Max-Planck-Institut
für Meteorologie

MAX-PLANCK-GESELLSCHAFT

International Max Planck Research School
on Earth System Modelling

Quantifying the Present and Future Climate Impact of Wildfire Emission Heights in an Earth System Model

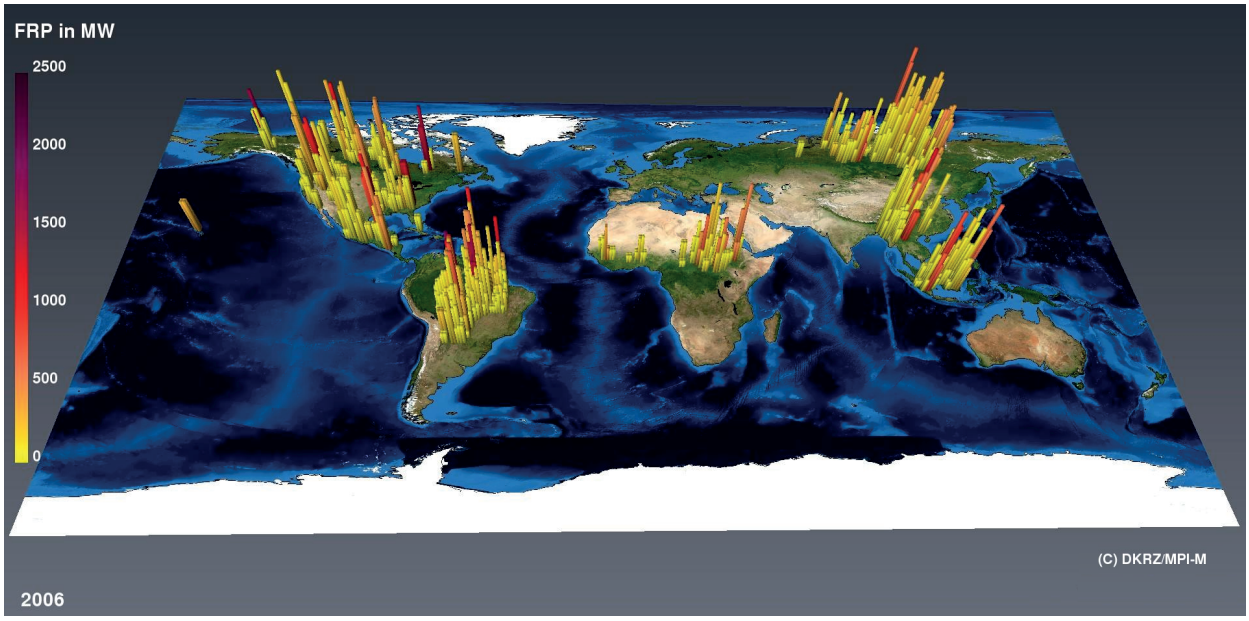

Andreas Veira

Hamburg 2015

Berichte zur Erdsystemforschung
Reports on Earth System Science

174
2015

Hinweis

Die Berichte zur Erdsystemforschung werden vom Max-Planck-Institut für Meteorologie in Hamburg in unregelmäßiger Abfolge herausgegeben.

Sie enthalten wissenschaftliche und technische Beiträge, inklusive Dissertationen.

Die Beiträge geben nicht notwendigerweise die Auffassung des Instituts wieder.

Die "Berichte zur Erdsystemforschung" führen die vorherigen Reihen "Reports" und "Examensarbeiten" weiter.

Notice

The Reports on Earth System Science are published by the Max Planck Institute for Meteorology in Hamburg. They appear in irregular intervals.

They contain scientific and technical contributions, including Ph. D. theses.

The Reports do not necessarily reflect the opinion of the Institute.

The "Reports on Earth System Science" continue the former "Reports" and "Examensarbeiten" of the Max Planck Institute.

Anschrift / Address

Max-Planck-Institut für Meteorologie
Bundesstrasse 53
20146 Hamburg
Deutschland

Tel./Phone: +49 (0)40 4 11 73 - 0
Fax: +49 (0)40 4 11 73 - 298

name.surname@mpimet.mpg.de
www.mpimet.mpg.de

Layout

Bettina Diallo and Norbert P. Noreiks
Communication

Copyright

Quantifying the Present and Future Climate Impact of Wildfire Emission Heights in an Earth System Model

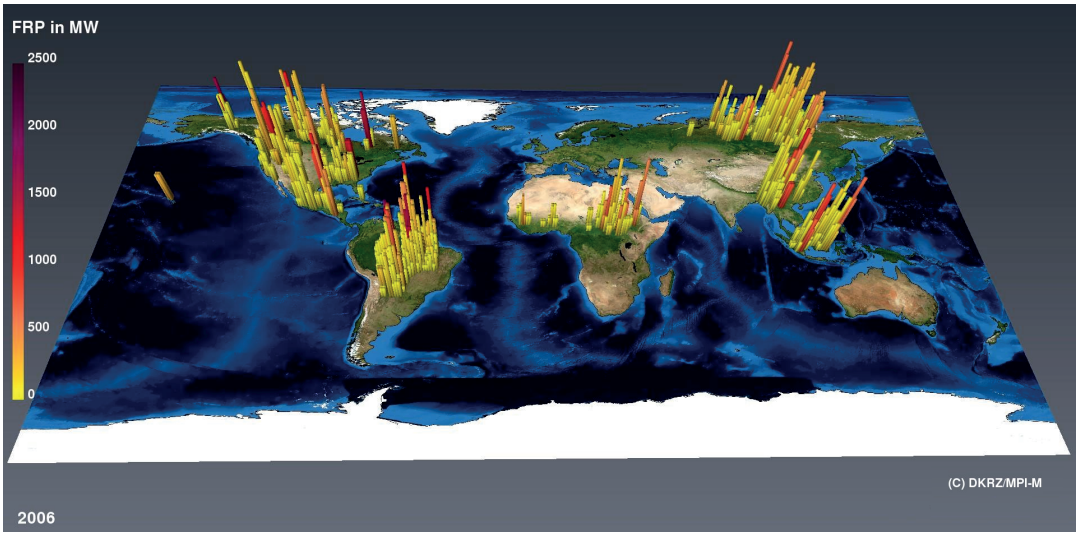

Andreas Veira

Hamburg 2015

Andreas Veira

Max-Planck-Institut für Meteorologie
Bundesstrasse 53
20146 Hamburg

Als Dissertation angenommen
vom Fachbereich Geowissenschaften der Universität Hamburg

auf Grund der Gutachten von
Prof. Dr. Martin Claußen
und
Dr. Silvia Kloster

Hamburg, den 4. 11. 2015
Professor Dr. Christian Betzler
Leiter des Departments Geowissenschaften

Berichte zur Erdsystemforschung / Max-Planck-Institut für Meteorologie 174
Reports on Earth System Science / Max Planck Institute for Meteorology 2015

ISSN 1614-1199

Abstract

Wildfires represent a major source for aerosol particles impacting atmospheric radiative transfer, atmospheric chemistry and cloud micro-physical properties. Compared to other emission sources, wildfires are unique in the sense that they are the only widespread source which can release emissions at high altitudes. Previous studies indicate that the height of the aerosol-radiation interaction crucially affects its climate impact. But the sensitivity to emission heights, i.e., the altitude at which emissions are injected into the atmosphere, has been examined only by a few case studies. In Earth system models (ESMs), the release of wildfire emissions is usually prescribed at the surface or at fixed heights.

In this study, a semi-empirical plume height parametrization is implemented and advanced in the aerosol-climate model ECHAM6-HAM2 to investigate the impact of wildfire emission heights on the atmospheric long-range transport of black carbon (BC) particles and radiation. The modified plume height parametrization simulates a reasonable global plume height distribution representing a major improvement over a prescribed emission release. However, the comparison to observational aerosol optical thickness (AOT) data shows that the improved plume height implementation only slightly enhances the model performance in AOT regionally, while large biases remain globally. Free-tropospheric BC concentrations are mainly determined by tropical convection and differences in emission inventories rather than by differences between parametrized and prescribed emission heights. Using the plume height parametrization, wildfire aerosol emissions cause a top of atmosphere radiative forcing (TOA RF) of -0.20±0.07 $\mathrm{Wm^{-2}}$. A prescribed emission release at the surface entails a comparable TOA RF of -0.16±0.06 $\mathrm{Wm^{-2}}$. Overall, substantial improvements in wildfire aerosol modeling likely rely on better emission inventories and aerosol process modeling rather than on improved emission heights.

In addition to the plume height sensitivity experiments, future wildfire emission fluxes and emission heights are simulated for Representative Concentration Pathway (RCP) scenarios. For this purpose, the process-based fire model SPITFIRE within the global vegetation model JSBACH is modified and run. The simulated fire emission fluxes and fire intensities serve as input for an ensemble of ECHAM6-HAM2 experiments. Compared to present day, fire emission fluxes are simulated to significantly increase in the extra-tropics by 2090-2099 due to enhanced fuel availability. The strongest changes in emission fluxes are found for the strongest warming scenario RCP8.5. In the tropics, fire emissions generally decrease due to land-use changes. While the increased atmospheric stability tends to decrease plume heights for RCP2.6 and RCP4.5, the enhanced fire intensity overcompensates the stability effects in RCP8.5. Nevertheless, mean global emission heights differ only by a few hundred meters. Changes in atmospheric BC concentrations and AOT are primarily driven by changes in fire emission fluxes and large-scale circulation patterns.

In summary, this PhD thesis for the first time assesses the importance of the wildfire emission height representation in an ESM for present and future climate conditions. Although emission heights are of limited importance globally, they may be key parameters for aspects such as regional aerosol-cloud interaction. The new implementations, which link global vegetation-fire and atmospheric aerosol modeling, provide a novel framework to investigate these regional aerosol-climate interactions in future high-resolution ESMs.

Zusammenfassung

Wald- und Buschbrände sind eine wichtige Quelle für Aerosolpartikel, welche den atmosphärischen Strahlungstransfer, die atmosphärische Chemie und die mikro-physikalischen Eigenschaften von Wolken beeinflussen. Von anderen Emissionsquellen unterscheiden sich Wald- und Buschbrände dadurch, dass sie als einzige flächendeckende Quelle Emissionen in große Höhen emittieren. Die Ergebnisse früherer Untersuchungen deuten darauf hin, dass die Höhe, in welcher die Aerosol-Strahlungswechselwirkung stattfindet, den Klimaeinfluss der Aerosolteilchen entscheidend beeinflussen kann. Die globale Bedeutung von Feuer-Emissionshöhen, d.h. der Höhe, in der Feueremissionen in die Atmosphäre eingetragen werden, wurde jedoch nur im Rahmen weniger Fallstudien untersucht. In Erdsystemmodellen wird die Freisetzung von Feueremissionen im Allgemeinen an der Landoberfläche oder in festgesetzten Modellschichten vorgeschrieben.

In der vorliegenden Arbeit wird eine semi-empirische Emissionshöhen-Parametrisierung im Aerosol-Klimamodell ECHAM6-HAM2 implementiert und verbessert, um den Einfluss von Feueremissionshöhen auf den atmosphärischen Aerosol-Ferntransport von Rußpartikeln und den Strahlungstransfer zu untersuchen. Die Analysen lassen erkennen, dass die implementierte Emissionshöhen-Parametrisierung eine angemessene globale Emissionshöhenverteilung simuliert und dadurch eine deutliche Verbesserung gegenüber vorgeschriebenen Emissionshöhen darstellt. Der Vergleich der simulierten Aerosol-optischen Dicke (AOD) mit Beobachtungsdatensätzen zeigt jedoch, dass die verbesserte Emissionshöhen-Parametrisierung nur zu einer geringfügigen regionalen Verbesserung der Modelleigenschaften im Bezug auf die AOD führt. Die erheblichen systematischen Abweichungen des Modells auf globaler Skala hingegen bleiben bestehen. Die Rußkonzentrationen in der freien Troposphäre werden in erster Linie durch tropische Konvektion und Unterschiede in den Emissionsinventaren bestimmt, während die Unterschiede zwischen verschiedenen Emissionshöhen-Implementierungen von geringerer Bedeutung sind. Unter Anwendung der semi-empirischen Emissionshöhen-Parametrisierung ergibt sich ein durch Feueremissionen ausgelöster Strahlungsantrieb am Oberrand der Atmosphäre von -0.20±0.07 Wm^{-2}. Eine vorgeschriebene Emissionsfreisetzung nahe der Landoberfläche führt zu einem vergleichbaren Strahlungsantrieb von -0.16±0.06 Wm^{-2}. Zusammenfassend kann man schlussfolgern, dass wesentliche Fortschritte in der Feuer-Aerosolmodellierung vermutlich nur durch eine Reduzierung der Unsicherheiten in den Feueremissionsinventaren sowie durch eine verbesserte Implementierung jener atmosphärischer Prozesse, welche die Aerosoleigenschaften beeinflussen, erreicht werden können. Emissionshöhen hingegen spielen nur eine untergeordnete Rolle.

Ergänzend zur Sensitivitätsstudie der Emissionshöhen-Implementierung wird auch der Feueremissionsausstoß für verschiedene zukünftige Emissionsszenarien (RCPs) simuliert. Dazu wird das prozessorientierte Feuermodell SPITFIRE innerhalb des globalen Vegetationsmodells JSBACH modifiziert und zur Simulation der globalen Feueraktivität genutzt. Die modellierten Feueremissionsflüsse und Feuerintensitäten dienen als Eingabeparameter für ein Ensemble von ECHAM6-HAM2 Experimenten. Im Vergleich zu den gegenwärtigen Klimabedingungen zeigt sich für den Zeitraum 2090–2099 ein erheblicher Anstieg der Feueremissionen in den Extratropen, welcher im Wesentlichen auf eine

Erhöhung der für die Verbrennung verfügbaren Biomasse zurückzuführen ist. Die stärksten Veränderungen in den Emissionsflüssen werden für das Szenario RCP8.5 simuliert, welches die stärkste Erwärmung repräsentiert. In den Tropen ist ein genereller Rückgang der Feueremissionen aufgrund von Landnutzungsänderungen erkennbar. Während für die Szenarien RCP2.6 und RCP4.5 ein Rückgang der Emissionshöhen aufgrund eines Anstiegs der atmosphärischen Stabilität erkennbar ist, wird diese Zunahme im Szenario RCP8.5 durch einen Anstieg in den Feuerintensitäten überkompensiert. Allerdings betragen die Unterschiede der globalen mittleren Emissionshöhen zwischen den verschiedenen RCP Szenarien nur maximal einige hundert Meter. Regionale Veränderungen in atmosphärischen Rußkonzentrationen und in der AOD werden in erster Linie durch Veränderungen in den Feueremissionsflüssen sowie durch Veränderungen in den großräumigen Zirkulationsmustern hervorgerufen.

Zusammenfassend wird in dieser Dissertation erstmals die Wichtigkeit der Darstellung von Emissionshöhen in einem Erdsystemmodell für heutige und zukünftige Klimabedingungen untersucht. Obwohl Emissionshöhen global nur von geringer Bedeutung sind, könnten sie dennoch einen Schlüsselparameter für spezifische Aspekte wie die regionale Wechselwirkung von Aerosolen und Wolken darstellen. Die in dieser Studie vorgestellten Modellimplementierungen, welche die Vegetations-Feuer-Modellierung mit der atmosphärischen Aerosolmodellierung verbinden, stellen ein neuartiges Modellsystem dar, um die regionalen Wechselwirkungen von Aerosolen und Klima in zukünftigen hochauflösenden Erdsystemmodellen zu erforschen.

Contents

Chapter 1

Introduction

1.1 Wildfire emissions in the Earth system

Wildfires, either set by humans or ignited naturally by lightning, impact the Earth system in many different ways. Below the ground, wildfires modify the physical and mineralogical soil properties and soil carbon pools (Neary et al., 1999; Certini, 2005). Above ground, fires represent a natural vegetation disturbance which can considerably impact vegetation dynamics (Bond and Keeley, 2005). In the atmosphere, trace gases and aerosols released by fires affect atmospheric chemistry, cloud-microphysical properties and radiation (Haywood and Boucher, 2000; Andreae and Merlet, 2001). However, wildfires are not only shaping the Earth system, but at same time their frequency and intensity is also driven by the climate itself (Marlon et al., 2008; Bowman et al., 2009). Therefore wildfires, also referred to as vegetation fires, form a complex and integral part of our Earth system.

Within the last two decades, the availability of satellite-based fire activity and emission data sets fundamentally helped to enhance our scientific understanding of vegetation-fire-climate interactions. Based on data from the polarorbiting Moderate Resolution Imaging Spectroradiometer (MODIS) first global estimates of burned area (Giglio et al., 2006) and total carbon emissions (van der Werf et al., 2006) have been derived. Meanwhile, about a dozen global wildfire emission inventories are available, including the Global Fire Emission Data Base (GFED) (van der Werf et al., 2010), the Fire INventory from NCAR (FINN) (Wiedinmyer et al., 2011) and the Global Fire Assimilation System (GFAS) (Kaiser et al., 2012). Although the uncertainties of the burned area and emission inventories remain large (e.g. Zhang et al., 2014), they provide observational constraints, which considerably helped to include reasonable parametrizations of wildfires in dynamic global vegetation models (DGVMs). Simple (e.g. Arora and Boer, 2005) as well as more sophisticated, process-based fire models like SPITFIRE (Thonicke et al., 2010) have been implemented into several DGVMs (e.g. JSBACH, LPJ, ORCHIDEE).

In DGVMs as well as in satellite-based emission data sets, the biomass burned by a fire is usually converted into emission estimates of trace gases (e.g. CO, CO_2, CH_4) and particulate matter by application of species-specific emission factors (Andreae and Merlet, 2001; Akagi et al., 2011). These emission estimates in turn serve as input for global circulation models to investigate the atmospheric impacts of wildfire emissions. In

contrast to the short-lived trace gas CH_4, for which wildfire emissions only contribute about 0.5–3 % to the total natural and anthropogenic emissions (Ciais et al., 2013), the relative contribution of the major wildfire aerosol species is significantly larger. Black carbon (BC) aerosols emitted from wildfires contribute approximately 30–40 % to the overall atmospheric BC emissions (Bond et al., 2013); for organic carbon (OC), wildfires even form the largest global emission source.

Together with dust, sea-salt and sulfate particles from natural and anthropogenic emission sources, BC and OC aerosol particles emitted from wildfires represent major drivers of the overall atmospheric aerosol effects (Haywood and Boucher, 2000; Andreae and Gelencsér, 2006). Aerosols can serve as cloud and ice condensation nuclei and impact atmospheric radiative transfer via direct, indirect and semi-direct effects (Boucher et al., 2013). The so called *direct aerosol effect* describes the scattering and absorption of solar radiation by aerosol particles (Ångström, 1962). While solely scattering sulphate and sea-salt aerosols are generally cooling the atmosphere, BC particles, which act strongly absorbing, are warming the atmosphere (Bond et al., 2013; Myhre et al., 2013). *Indirect aerosol effects* primarily characterize the increase in cloud albedo and cloud lifetime for increased aerosol concentrations (Twomey, 1977; Albrecht, 1989; Lohmann and Feichter, 2005). *Semi-direct aerosol effects* describe the effect that absorption of solar radiation by aerosols in clouds may cause evaporation of the clouds (Johnson et al., 2004). Aerosols do not only influence cloud properties, but they are dominantly removed by in-cloud precipitation formation and scavenging below clouds; thus aerosols and clouds represent interactive players in the atmosphere (Andreae and Rosenfeld, 2008).

Simultaneously to the development of DGVMs, aerosol-modules have been coupled to global climate models in order to assess the emission, transport and removal of aerosols from wildfires and other sources (Langmann et al., 2009; Carslaw et al., 2010). In the framework of the Aerosol Comparisons between Observations and Models (AEROCOM) initiative (Kinne et al., 2006), the radiative forcing (RF) of biomass burning emissions emissions in 15 state-of-the-art aerosol climate models has been analyzed (Myhre et al., 2013). Although a slightly positive RF of $+0.15\,\mathrm{W\,m^{-2}}$ was found for the multi-model mean, no consensus about a positive or negative RF could be identified. In addition, Samset et al. (2013) analyzed the influence of the vertical BC distribution on the overall BC RF in 12 different AEROCOM models. Globally, the authors found good agreement between models that, on average, more than 40 % of the BC RF is attributed to BC found above 5 km. Moreover, Ban-Weiss et al. (2011) used the Community Atmosphere Model to explore the altitude-dependence of the equilibrium climate response caused by BC particles. While BC particles close to the surface were simulated to cause a surface warming, BC particles in the upper troposphere and the stratosphere introduced a cooling effect on surface temperatures. With the limited vertical transport of aerosol particles from the planetary boundary layer (PBL) into the free troposphere (FT), the direct injection of BC into layers above the PBL represents a key parameter for the overall RF. As wildfires are the only emission source besides volcanic eruptions and aircraft emissions, which can directly inject emissions into the FT, the contribution of wildfires to the overall BC RF is assumed to be particularly important.

By a number of regional cases studies wildfire emission heights, i.e. the altitude above surface at which emissions are injected into the atmosphere, have been shown to impact the long-range transport of emissions and the atmospheric radiative transfer (Damoah et al., 2006; Dirksen et al., 2009; Peterson et al., 2015). There is evidence that events of particularly strong fires combined with favorable atmospheric conditions in rare cases even inject emissions directly into the lower stratosphere (Fromm et al., 2006; Siddaway and Petelina, 2011). Such emission injections may be comparable to small volcanic eruptions. Moreover, short-term case studies also investigated the local impact of biomass burning aerosols on precipitation and atmospheric convection. It has been shown that wildfire smoke generally increases droplet number concentrations, decreases droplet size and alters vertical temperature profiles (e.g. Andreae et al., 2004; Grell et al., 2011). However, depending on the specific atmospheric conditions, the delayed onset of rain-out may either reduce precipitation or trigger an increase in heavy rainfall with an enhanced probability of large hail production.

Beyond the atmospheric aerosol impacts, BC particles deposited on ice- and snow-covered land and sea surfaces are known to reduce the surface albedo by 1.5–3 % (Hansen and Nazarenko, 2004). This reduction in albedo entails a global RF in the order of $+0.05\,\mathrm{W\,m^{-2}}$ corresponding to a 2-m air temperature change of +0.10 K to +0.15 K (Flanner et al., 2007). Although a fraction of 80 % of the RF is attributed to anthropogenic emissions, the increase in snow melting rates of 19-28 % is to a large extent caused by boreal wildfires, which are primarily active in the summer season.

Due to the large range of processes by which wildfire emissions impact the climate, an integral representation of fires in an Earth system model (ESM) is required to simulate the interactions across spatial and temporal scales which range from minutes to decades and from some meters to thousands of kilometers (Stavros et al., 2014; Loehman et al., 2014). The schematic drawing presented in Fig. 1.1 illustrates and summarizes our current scientific knowledge about the fire emission climate impact including emission heights, long-range transport and direct as well as indirect aerosol effects. Overall, the representation of wildfires as an interactive vegetation disturbance and emission source in ESMs is still poor (Bowman et al., 2009; Langmann et al., 2009; Keywood et al., 2013), even though case studies quantified the climate impact of individual processes like the long-term changes of post-fire surface albedo (Randerson et al., 2006) or the influence of wildfire smoke on tropical convection (Andreae et al., 2004). If we want to proceed towards an improved understanding of the role of fires in past, present and future climates, we are in need of both, a significant reduction in the current emission inventory uncertainties as well as improved process-representations of atmospheric transport and removal processes in global models. Against the background of the large model biases in long-range transport with important implications for other parts of the climate system (e.g. radiation, soot deposition on snow), an assessment, how emission heights influence other aerosol-climate modeling parameters is essential to reduce the model uncertainties. The detailed quantification of this “emission height climate impact“ represents the main goal of this PhD thesis.

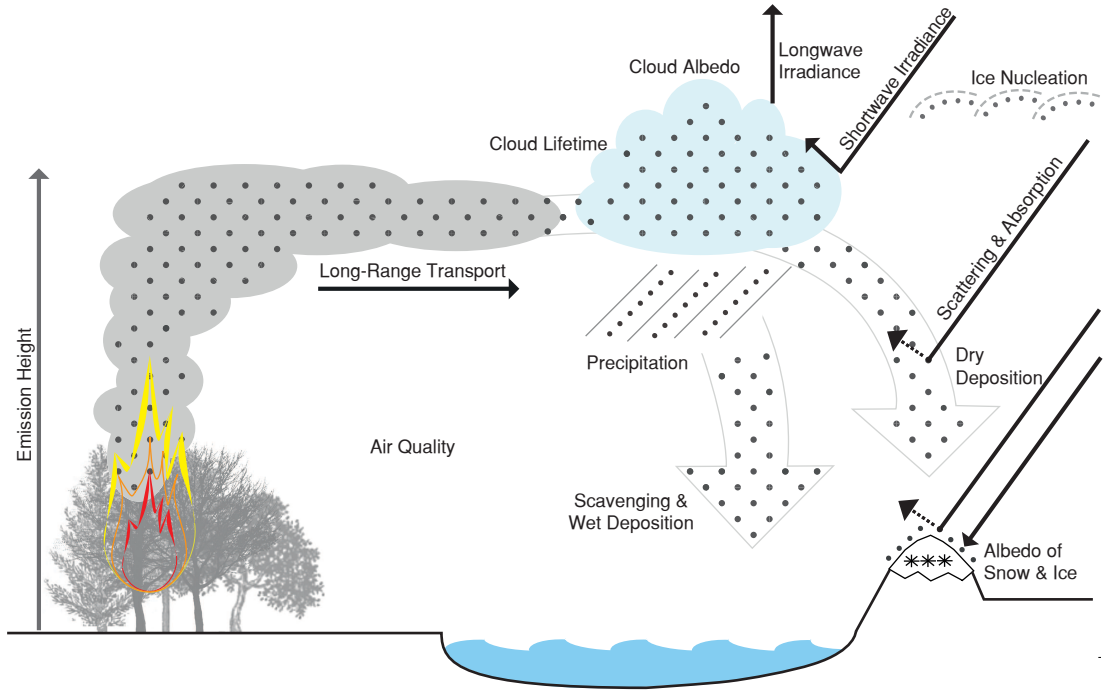

Figure 1.1: Schematic drawing of fire-aerosol-climate interactions in the Earth system. The simplified illustrations of aerosol transport and aerosol-radiation interactions represent a modified synthesis of schematic figures provided by Boucher et al. (2013) and Ward et al. (2012).

1.2 Satellite-based wildfire emission inventories

Due to the fact that the strength of the fire emission release is linked to the heat release, which impacts atmospheric convection, fire emission inventories and emission heights are closely connected. Basically, satellite-based wildfire emission estimates can be derived by two different methods. The "top-down approaches" use observations of the atmospheric aerosol-radiation interaction combined with fire radiative power (FRP) measurements to calculate global fire emission coefficients and emission estimates (e.g. Ichoku and Ellison, 2014). The "bottom-up approaches" use measurements of burned area or FRP and apply land-cover-specific conversion and species-specific emission factors to calculate wildfire aerosol emissions (Zhang et al., 2014, and references therein). Bottom-up as well as top-down emission inventories provide daily, monthly or annually averaged emission fluxes of particulate matter or BC, OC and sulfur dioxide (SO_2) as well as other trace gas species (e.g. van der Werf et al., 2010; Wiedinmyer et al., 2011; Kaiser et al., 2012; Ichoku and Ellison, 2014).

In order to illustrate the basic global fire emission patterns, Fig. 1.2 provides a global map of annually averaged BC emission fluxes for 2003-2013 in the GFASv1.2 emission inventory. Globally, tropical Africa represents the largest wildfire emission source with observed fire return intervals of only a few years (Thonicke et al., 2001). However, although fires occur much less frequently in dense forests of the Amazon and in boreal North America and Siberia (fire return intervals of 50-1000 years), they considerably contribute to the

overall global emissions, because large amounts of biomass can be accumulated in the period between two fire events.

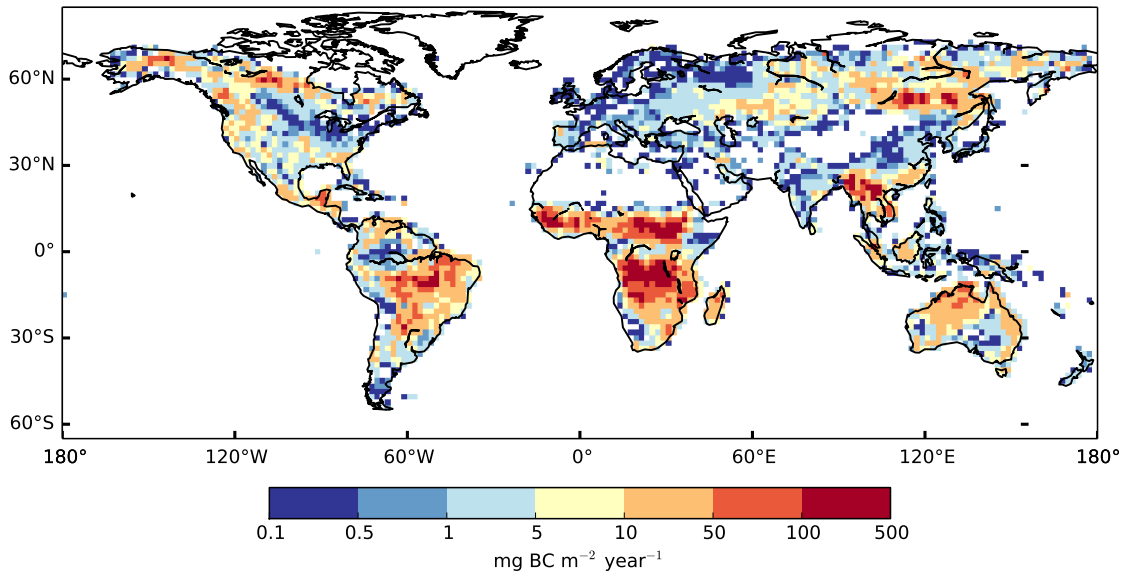

Figure 1.2: Global map of annual mean wildfire BC emission fluxes in GFASv1.2 for 2003-2013. For more detailed information on the derivation of emission flux estimates and the data assimilation techniques applied in GFAS, see Kaiser et al. (2012).

Due to the large uncertainties in satellite-based fire quantities (e.g. burned area or FRP) as well as in the emission calculations via vegetation-specific emission factors (Andreae and Merlet, 2001; Akagi et al., 2011), all global emission data sets include large biases. Petrenko et al. (2012) and Zhang et al. (2014) consistently demonstrated that the regional emission flux estimates of different emission inventories vary by up to a factor 5-10. Moreover, all bottom-up emission inventories have been shown to cause significant underestimations of the aerosol optical thickness (AOT) in global aerosol-climate models (e.g. Petrenko et al., 2012; Kaiser et al., 2012; von Hardenberg et al., 2012). The AOT describes the fraction of light of a certain wavelength which is extinct while traveling through the atmosphere. Besides the single scattering albedo and the phase function, the AOT determines the direct radiative impact of aerosols (Yu et al., 2006). A similar order of local over- as well as underestimation was also found for all AEROCOM models regarding atmospheric BC concentrations evaluated by in-situ aircraft measurements in remote regions (Schwarz et al., 2013). However, these biases were not only attributed to biases in wildfire, but also to biases in anthropogenic emission inventories.

1.3 Wildfire emission estimates in DGVMs

In addition to the satellite-based burned area and emission inventories for present day (PD) climate conditions, simple fire indices as well as more sophisticated fire models in DGVMs have been applied to reproduce past and PD burned area and emission estimates and to predict future wildfire activity (e.g. Flannigan et al., 2009; Thonicke et al., 2010; Kloster

et al., 2012). By comparison to reconstructions, Pfeiffer et al. (2013), Yue et al. (2014) and Kloster et al. (2010) found reasonable agreement of the simulated fire activity in LPJ-LM, ORCHIDEE and CLM to observational estimates for the 20th century. These studies provide evidence for the basic ability of state-of-the-art DGVMs to simulate global fire activity patterns in a reasonable way. Nevertheless, regional biases remain large.

Regarding potential changes in future fire activity, various modeling studies found vast agreement about a future increase in fire probability for boreal and temperate regions at the end of the 21st century due to climate warming (e.g. Flannigan et al., 2009; Moritz et al., 2012, and references therein). The magnitude of these extra-tropical future increase in wildfire activity and the direction of future changes in tropical wildfire activity, however, are still very uncertain. Furthermore, most of the previous studies were limited to the prediction of changes in fire weather indices or burned area not providing estimates for future changes in emission fluxes.

1.4 Emission heights

In contrast to the globally available satellite-based emission flux estimates, up to now there is no automatic algorithm available, which can detect wildfire emission heights of individual fires. Nelson et al. (2008, 2013) published a tool called MISR Interactive Explorer (MINX) which is used to analyze Multi-angle Imaging Spectroradiometer (MISR) aerosol data. MISR data are available since 2000 and provide largely global coverage (Diner et al., 1998; Kahn et al., 2007). The MINX tool enables a partly-automatic emission height calculation with an uncertainty range of only ± 200 m, but smoke plumes in satellite images have to be manually digitized and referred to individual MODIS fires to calculate emission heights. Based on MINX, a couple of studies have analyzed regional emission height distributions in North America (Val Martin et al., 2010), South-East Asia (Tosca et al., 2011) and Australia (Mims et al., 2010). Various regional MINX plume height inventories have been composed in the MISR Plume Height Project (MPHP). Figure 1.3 qualitatively visualizes mean plume heights of the MPHP for the year 2006. The observations indicate that there is a weak to moderate correlation between FRP and plume heights, but atmospheric stability represents the major determining factor for the plume rise (Sofiev et al., 2012). Globally only 5-15 % of all plumes are assumed to reach the FT, whereas the remaining fraction of plumes inject the entire emissions into the PBL. Even though very few plumes reach altitudes of more than 5 km, the large majority of plumes is only injecting emissions into the lowest 0.5–1.5 km above surface (Val Martin et al., 2010; Sofiev et al., 2013).

However, the MPHP data set provides exclusively top emission heights, not the full vertical aerosol concentration profiles. The investigation of vertical emission profiles requires either airborne in-situ aerosol measurements in fresh emission plumes or the application of ground-based remote sensing techniques close to the fires. Due to the logistical challenges of these measurements, wildfire emission profiles have only been explored by a small number of measurement campaigns, primarily for prescribed burns (e.g. Melnikov et al., 2008; Liu et al., 2013; Archer-Nicholls et al., 2015). Up to now, no global data set of vertical emission profiles in the immediate vicinity of fires exists. Therefore vertical emission distributions are usually prescribed in aerosol-climate models.

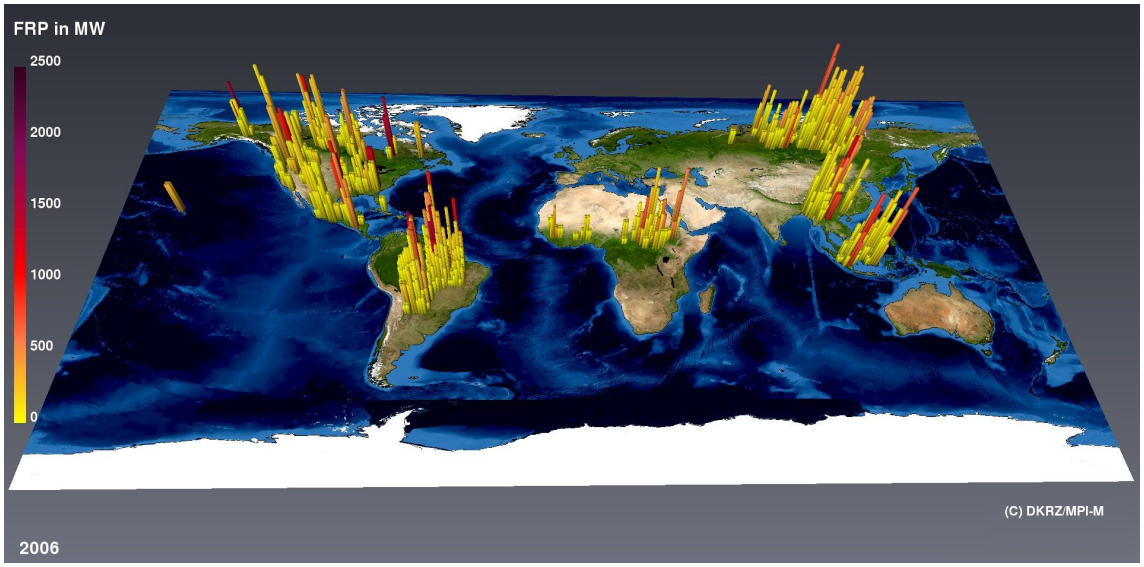

Figure 1.3: Visualization of gridded mean plume heights of the MPHP data set for the year 2006. The height of each column shows the injection height above surface. The highest columns represent top injection heights of approximately 6 km; a linear scaling of the plume heights is applied. Colors indicate the related total FRP detected by MODIS.

In addition to the observational emission height data sets, a broad range of plume rise models has been developed in the framework of local and regional case studies (Goodrick et al., 2012, and references therein). These include semi-empirical (e.g. Briggs, 1975; Lavoué et al., 2000; Achtemeier et al., 2011; Sofiev et al., 2012) as well as analytical-numerical (e.g. Heikes and Angeles, 1990; Trentmann et al., 2006; Freitas et al., 2007) models. In general circulation models (GCMs), the performance of plume height parametrizations has been evaluated by use of the MPHP. On the global scale, the model performances have been shown to be moderate to poor with little difference between the different plume height parametrizations (Val Martin et al., 2012). Therefore, in aerosol-climate models, wildfire emissions are usually released at the surface (e.g. Tosca et al., 2013) or at prescribed levels in the PBL and the lower free troposphere (Dentener et al., 2006). So far, no predictions of potential future changes in emission heights have been published.

1.5 Thesis outline

The overall scientific goal of this study is to investigate, if wildfire emission heights represent a key parameter for our scientific understanding of wildfire-climate interactions. In addition, this PhD thesis provides new methods to adequately represent emission heights in global aerosol-climate models. The focus of this study lies on the investigation of present day as well as future fire-climate interactions and explores the following research questions:

I) Which degree of plume height parametrization complexity is required to adequately represent wildfire emission heights in state-of-the-art global climate models?

II) How do wildfire emission heights impact global BC concentrations, BC deposition rates and atmospheric radiative transfer?

III) How might future changes in fire emissions and fire emission heights in a warmer climate impact atmospheric BC concentrations and atmospheric radiative transfer?

For the investigation of question (I) presented in chapter 2, prescribed emission heights in the aerosol-climate modelling system ECHAM6-HAM2 are replaced by a semi-empirical plume height parametrization. Simulated global plume height distributions are evaluated against the observational MPHP data set. For prescribed as well as parameterized emission heights, global plume height patterns and the impact of a prescribed diurnal cycle in FRP and emissions are discussed. In addition, the global emission height spectra of the simple plume height parametrization are compared to results from a more sophisticated, fully analytical plume model. However, in consideration of the low horizontal, vertical and temporal resolution of today's global climate models, this study is not designed to develop a perfect parametrization of fire-induced convection, which would be more suitable for local, high resolution modelling. The results of chapter 2 have been published in Atmospheric Chemistry and Physics [1].

In the third chapter of this PhD thesis, the impact of the emission heights on atmospheric BC concentrations and radiation is discussed. Besides the simulations with the plume height parametrization introduced in chapter 2, extreme cases of globally prescribed emission injections either completely into the FT or at the surface serve as constraints of a maximum respectively minimum fire emission height climate impact. The focus lies on the discussion of radiative effects and changes in BC concentrations and deposition rates. The modelling results are compared to observations from Aerosol Robotic Network (AERONET) ground-based observations as well as MODIS and Cloud-Aerosol Lidar with Orthogonal Polarization (CALIOP) satellite observations to quantify the improvements in model performance which are achieved by the improved plume height representation. The results of the third chapter have also been published in Atmospheric Chemistry and Physics [2].

In the fourth chapter of this study, wildfire activity and emissions for future Representative Concentration Pathway (RCP) scenarios are simulated with the interactive, process-based fire model SPIRTFIRE within the global vegetation model JSBACH. Simulated emission fluxes and FRP are applied for an ensemble of ECHAM6-HAM2 simulations for the time period 2090-2099. These experiments enable the investigation of climate-change induced changes in emission heights. In the analysis, the impact of changes in climate and changes in wildfire activity on emission heights and aerosol long-range transport are discussed. Thus, this study provides a novel approach to investigate future vegetation-wildfire-climate interactions. The results of chapter 4 have been prepared for submission to the Journal of Geophysical Research.

[1] Veira, A., Kloster, K., Wilkenskjeld, S., Remy, S. (2015). Fire emission heights in the climate system Part 1: Global plume height patterns simulated by ECHAM6-HAM2. Atmospheric Chemistry and Physics, 15, 7155–7171.

[2] Veira A., Kloster K., Schutgens, N. A. J. , Kaiser, J. W. (2015). Fire emission heights in the climate system - Part 2: Impact on transport, black carbon concentrations and radiation. Atmospheric Chemistry and Physics, 15, 7173–7193.

The combined analysis of the plume height parametrization evaluation, the simulated global plume height patterns and the assessment of the overall emission height climate impact offers a unique framework to investigate the three research questions raised above. In chapter 5, a conclusive summary of chapters 2, 3 and 4 is provided and the relevance of this study for our current understanding of fire-climate interactions is discussed. Furthermore, suggestions for future directions of ESM development are given in the outlook.

Chapter 2

Global plume height patterns simulated by ECHAM6-HAM2

2.1 Introduction

Aerosol particles emitted from fires are known to impact a wide range of atmospheric processes including radiative transfer, atmospheric chemistry and cloud micro-physical processes (Twomey, 1977; Crutzen and Andreae, 1990; Heald et al., 2014). A crucial parameter that has been identified to influence the lifetime of aerosols and thus potentially also their climate impact is the fire emission height, i.e., the altitude above the surface at which fire smoke plumes release emissions into the atmosphere. The terms "fire emission height", "injection height" and "plume height" have been used as equivalent terms in the literature, although they do not always have the same meaning. In this study, we use the term "plume height" to describe the top level above the surface at which emissions are injected, i.e., the "plume-top height". The term "emission heights" describes the full range of heights at which wildfire emissions are released. "Emission profiles" specify the entire vertical emission profiles from the surface to the top of the smoke plume.

Theories and models, which describe the process of plume rise, have been developed since the 1970s. Today various semi-empirical (e.g., Briggs, 1975; Achtemeier et al., 2011; Sofiev et al., 2012) and analytical-numerical plume height models (e.g., Heikes and Angeles, 1990; Trentmann et al., 2006; Freitas et al., 2007) are available. In addition to these plume height models which take into account fire properties and atmospheric conditions to calculate plume heights, other parametrizations are solely based on fire brightness temperature (Hodzic et al., 2007) or fire intensity (Lavoué et al., 2000). The review papers of Goodrick et al. (2012) and Heilman et al. (2013) provide extensive summaries of various plume height models. Although a reasonable performance of the plume models has been demonstrated for selected case studies on local or regional scales, the knowledge about smoke plume heights on a global scale is very limited due to a lack of observational data sets. Besides a small number of airborne in situ and ground-based remote-sensing studies, e.g., Melnikov et al. (2008) or Liu et al. (2013), satellite data sets provide observations of potentially global coverage. Although smoke plume measurement uncertainties are only $\pm 200\,\mathrm{m}$ for well-constrained plumes (Kahn et al., 2008; Nelson et al., 2013), only a lim-

ited number of plumes are available on the global scale, because a partly manual analysis is required for each individual plume. The most comprehensive data set of individual smoke plume heights is provided by the MPHP that has been analyzed in the framework of several regional studies (Mazzoni et al., 2007; Val Martin et al., 2010; Sessions et al., 2011). These studies indicate a large variability of smoke plume heights all over the globe. Various case studies demonstrated that particularly intense fires can, under favorable meteorological conditions, result in emission injections into the upper troposphere or even the lower stratosphere (Damoah et al., 2006; Luderer et al., 2006; Dirksen et al., 2009). Very rare cases of pyro-cumulonimbus events caused by particularly strong fires may even be comparable to small volcanic eruptions (Fromm et al., 2006, 2008; Siddaway and Petelina, 2011). However, the majority of emission injections are limited to the PBL (Gonzi and Palmer, 2010; Val Martin et al., 2010; Ichoku et al., 2012).

The studies of Hyer et al. (2007), Leung et al. (2007) and Jian and Fu (2014) showed that the transport of wildfire emissions crucially depends on an appropriate implementation of smoke plume heights that consider the free tropospheric injection of a certain emission fraction. Nevertheless, due to computational costs and the lack of complexity regarding the representation of fire processes in global models, standard versions of state-of-the-art global climate and Earth system models respectively currently make use of simple latitude- and region-dependent vertical emission distributions (Dentener et al., 2006) or prescribe injections at the surface (e.g., Tosca et al., 2013).

In order to step forward towards a better representation of smoke plume heights in climate models, we implement the simple, semi-empirical plume height parametrization by Sofiev et al. (2012) into the general circulation model ECHAM6 extended by the aerosol module HAM2. In a first step, we evaluate the performance of the plume height parametrization for selected plumes reported in the MPHP data set. We use FRP reported in the MPHP based on MODIS data to test different versions of the parametrization on the global scale and constrain uncertainties introduced by uncertainties in fire-related and meteorological variables. Furthermore, the Sofiev plume height parametrization is adjusted to the ECHAM6-HAM2 aerosol–climate modeling system by the application of a statistical–empirical tuning. In a second step we simulate plume heights in ECHAM6-HAM2 globally for the years 2005–2011. For these experiments GFAS FRP (Kaiser et al., 2012) is used as input. We carry out a number of simulations that cover the standard Sofiev parametrization as well as a modified version of the Sofiev parametrization optimized for application in ECHAM6-HAM2. Moreover, effects of the implementation of a prescribed diurnal cycle are investigated. A sensitivity simulation with a global doubling of FRP assesses the implications of a potential climate-induced increase in fire intensity.

Section 2.2 introduces the ECHAM6 global circulation model extended by the HAM2 aerosol model, configurations of the Sofiev plume height parametrization and the GFAS data set. Section 2.3 provides a statistical analysis of the global plume height parametrization performance and the application of a statistical–empirical FRP correction. In Sect. 2.4, we present global plume height patterns simulated by ECHAM6-HAM2 enhanced by the Sofiev parametrization and compare these to plume height distributions in the standard version of the ECHAM6-HAM2 model. Furthermore, we discuss the influence of the diurnal cycle in fire intensity. In Sect. 2.5, we compare plume heights simulated

by the Sofiev parametrization to results from a more complex 1-D plume model. The conclusions of this chapter are summarized in Sect. 2.6, where we discuss our results in the context of ESM development.

2.2 Methodology

In the following, the general setup of the global circulation model ECHAM6, the aerosol model extension HAM2 and the semi-empirical plume height parametrization are described. We introduce the MPHP data set which we use for the evaluation of the plume height parametrization. Moreover, the implementation of the GFAS fire intensity data set in ECHAM6-HAM2 is explained. The last two sections present details on the specific model setup used for the plume height evaluation and the simulation of global plume height patterns.

2.2.1 ECHAM6-HAM2 model description

ECHAM6 is a general circulation model and serves as the atmospheric and land component of the Max Planck Institute Earth System Model (MPI-ESM). A detailed model description is provided by Giorgetta et al. (2013) and Stevens et al. (2013). For all our simulations we apply a T63 grid (spectral space) which corresponds to a Gaussian grid of approximately $1.875° \times 1.875°$. In the vertical, we use 47 vertical layers ranging from the surface to 0.01 hPa. A computing time step of 10 min is chosen for all simulations. The plume height parametrization evaluation experiments only apply prescribed sea surface temperature, which originates from the Atmosphere Model Intercomparison Project (AMIP). No nudging against observations is applied for these simulations, because we aim to investigate the basic skills of the ECHAM6-HAM2 model (extended by the plume height parametrization) to capture the spectrum of plume heights, not to reproduce individual plume observations.

For all other simulations, the atmospheric model is additionally nudged against observational data every 6 h. Thus, the model dynamics is forced to stay close to the ERA-Interim reanalysis fields (Dee et al., 2011) and changes in global plume height patterns between different plume height parametrizations stay comparable. For these simulations, the ECHAM6 model is extended by the aerosol module HAM2, modeling the dynamics, micro-physics, transport and radiative impact of aerosol species (Stier et al., 2005). The aerosol module represents the aerosol spectrum by superposition of seven lognormal distributions including nucleation, Aitken, accumulation and coarse mode. Vegetation fire emissions, here referred to as "wildfire emissions", are represented by three species: BC, OC and SO_2. A description of the changes in the HAM model configuration from the original model version HAM1 (Stier et al., 2005) to HAM2, used in this study, has been published by Zhang et al. (2012a). The term "ECHAM6-HAM2" in this study refers to model version ECHAM6.1.0-HAM2.2.

Top plume heights H_p in the standard version of ECHAM6-HAM2.2 are generally prescribed as the PBL height plus two model layers:

$$H_\mathrm{p} = \text{PBL Height} + 2\,\text{model layers}. \tag{2.1}$$

For the large majority of plume heights lower than 4 km, 75 % of the released wildfire emissions are vertically distributed with a constant mass mixing ratio from the surface to the level below the PBL, 17 % are injected into the next model layer above the PBL and 8 % are injected in the layer of height H_{p}. If the PBL height exceeds 4 km, the plume heights are set to PBL height and the emissions are equally distributed with constant mass mixing ratio from the surface to the first model layer below the PBL height. The upper limit of 4 km is an arbitrary value, but it represents the standard plume height implementation of ECHAM6-HAM2 described by Zhang et al. (2012a). In order to ensure comparability of our results to previous studies, we apply this standard implementation for one reference simulation, whereas improved plume height parametrizations are used for all other simulations.

2.2.2 Implementation of an improved plume height parametrization

To improve the representation of plume heights in ECHAM6-HAM2, we implement the simple, semi-empirical plume height parametrization by Sofiev et al. (2012), henceforth named Sofiev Parametrization (SP). Although the SP has been empirically tuned by observations, it is based on an analytical derivation which describes the plume rise as an atmospheric buoyancy process. For the complete derivation of the SP see Sofiev et al. (2012). The original SP predicts plume heights as a function of PBL height, H_{PBL}, Brunt–Väisälä frequency of the FT, N_{FT}, at 2× PBL height, and the total FRP of a fire, P_{f}:

$$H_{\mathrm{p}} = \alpha H_{\mathrm{PBL}} + \beta \left(\frac{P_{\mathrm{f}}}{P_{\mathrm{f0}}} \right)^{\gamma} \exp\left(-\delta N_{\mathrm{FT}}^2 / N_0^2 \right). \tag{2.2}$$

Here, α is that part of the PBL passed freely, β is a scaling factor for the fire intensity, γ describes the power-law dependence on P_{f}, δ scales the dependence on the stability of the FT, N_0 is the reference Brunt–Väisälä frequency and P_{f0} is the reference FRP. N_0 and P_{f0} are a priori chosen as $N_0 = \sqrt{2.5 \,\mathrm{x}\, 10^{-4}}\,\mathrm{s}^{-1}$ and $P_{\mathrm{f0}} = 10^6\,\mathrm{W}$, respectively. The constants α, β, γ and δ have been determined by Sofiev et al. (2012) using a computational learning data set:

$$\alpha = 0.24,\ \beta = 170\,\mathrm{m},\ \gamma = 0.35,\ \delta = 0.6. \tag{2.3}$$

As the use of N_{FT} at 2× PBL height is, from a physical point of view, not most appropriate for plumes which do not reach the FT, Sofiev et al. (2012) proposed a two-step iteration scheme, with separate tuning constants for PBL and FT plumes.

For PBL plumes

$$\alpha = 0.15,\ \beta = 102\,\mathrm{m},\ \gamma = 0.49,\ \delta = 0.0, \tag{2.4}$$

and for FT plumes

$$\alpha = 0.93,\ \beta = 298\,\mathrm{m},\ \gamma = 0.13,\ \delta = 0.7. \tag{2.5}$$

In this study, the performance of the one-step as well as the two-step SP are tested. Konovalov et al. (2014) successfully applied the one-step SP for CO modeling in the CHIMERE model. For stable PBL layers, Kukkonen et al. (2014) achieved improved plume height

predictions with the SP when replacing the Brunt–Väisälä frequency of the FT by the inversion layer Brunt–Väisälä frequency. Thus, for all nighttime plumes (18:00–08:00 LT) we replace N_{FT} in Eq. (2.2) by N_{PBL} which describes the Brunt–Väisälä frequency of the stable nocturnal boundary layer at the second lowest model layer approximately 150 m above the surface.

The implementation of this simple plume height parametrization is a significant improvement compared to prescribed plume heights, because it takes into account fire activity as well as ambient meteorological conditions at the time of the fire. However, various parameters, such as fire size and wind drag (Freitas et al., 2007, 2010) or entrainment and multiple core fire structure (Rio et al., 2010), are known to impact plume heights and are not explicitly represented in the SP. On the other hand, studies by Goodrick et al. (2012), Val Martin et al. (2012), Rosário et al. (2013) and Strada et al. (2013) indicate that neither of the more complex plume models shows an outstanding model performance. Moreover, the input parameters required for plume models on the global scale, such as fire size and fire intensity, are still very uncertain. Although FRP is strongly correlated with the heat flux of a fire and thus with fire-induced atmospheric convection, the reliance of plume heights on FRP measured by remote-sensing techniques is much more uncertain than the theoretical relationship between FRP and heat fluxes might suppose. Therefore, the use of a more advanced, more analytical plume model driven by original MODIS or derived FRP data cannot be expected to increase the accuracy of plume height predictions for global climate models with coarse resolution.

2.2.3 MPHP satellite data set

The MPHP represents a synthesis of MISR smoke aerosol data and MODIS MOD14 thermal anomaly data (Nelson et al., 2008, 2013). This unique plume height data set has been accomplished by application of the MINX software tool which retrieves wind-corrected plume heights from MISR data. In contrast to the plume heights provided in the MPHP, no further processing is applied to the manually selected MODIS MOD14 thermal anomalies which are attributed to individual MISR plumes. The latest release of the MPHP (April 2012) includes data of wildfire smoke plumes in North and South America, Eurasia, Africa and Southeast Asia, observed between 2001 and 2009. The MPHP data set used in this study is based on red band retrievals only as no blue band data were available. For future studies, an explicit validation of red and blue band retrievals is highly desirable, because for thin plumes blue band retrievals are expected to provide more accurate plume height estimations than red band retrievals.

Various studies made use of specific parts of this data set: the assignment of plume height distributions to vegetation types in North America (Diner et al., 2008; Val Martin et al., 2010), peat fire plumes in Borneo and Sumatra (Tosca et al., 2011) and the analysis of Australian bush fire plumes (Mims et al., 2010). Each individual plume data set provides extensive information about FRP, optical smoke properties, plume height statistics and wind profiles. For more detailed information, see the official product description at `http://www-misr.jpl.nasa.gov/getData/accessData/MisrMinxPlumes/`. As stated in the MPHP data quality statement and the error analysis therein, important biases are in-

Table 2.1: FRP bin scheme used for ECHAM6-HAM2 simulations. Individual GFAS fires of $0.1° \times 0.1°$ resolution are assigned to FRP bins 1–41 according to their FRP value. See text for more detailed information.

FRP bin No.	**1–10**	**11–15**	**16-21**	**22–26**	**27–41**
FRP range [MW]	0–100	100–200	200–500	500–1000	>1000
Bin width [MW]	10	20	50	100	–

troduced by pyro-cumulus clouds which hide below-cloud fire activity, by shortcomings in the manual digitization of the plumes and by large uncertainties in the MODIS fire pixels. By excluding plumes of *poor* or *fair* retrieval quality (Nelson et al., 2008) and incomplete individual data files, the MPHP provides 6942 plumes which we use for the evaluation of the SP. A visualization of mean annual MPHP plume height values for the year 2006 is presented in Fig. 1.3 (see chapter 1.4). This visualization illustrates the heterogeneous plume height distribution in the MPHP data set and gives a qualitative sense of plume height distributions and FRP diversity. On average, fires of small fire intensity feature lower plume heights, but for presumably favorable meteorological conditions, even low-intensity fires reach plume heights of several kilometers. According to the official MPHP product description and Kahn et al. (2008), an observational plume height accuracy of ± 200 m can be assumed. Due to the fact that MISR detects aerosol plumes that have been aged for a certain period of time, the measured plume heights do not in some cases adequately represent the convection generated by the thermal anomalies at the time of a specific satellite overpass. Thus, MODIS FRP values that correspond to MPHP plume heights can only be seen as a rough approximation.

2.2.4 GFAS fire intensity data

The investigation of global plume height patterns and the subsequent climate impact requires fire intensity data of full global coverage which the MPHP does not provide. In the current standard setup of ECHAM6-HAM2, wildfire emissions from the AEROCOM project are prescribed (Dentener et al., 2006), but no data on FRP are provided. Therefore, we extended the model to use FRP information from an external data set as a boundary condition. The GFASv1.1 data set (Kaiser et al., 2012) offers not only global FRP data but also corresponding wildfire emissions of BC, OC and SO_2. Thus, a consistent framework for this study and subsequent investigations of the emission height climate impact is provided. GFASv1.1 applied in this study has a spatial resolution of $0.1° \times 0.1°$ and a daily temporal resolution. We assume that each $0.1° \times 0.1°$ grid cell includes only one individual fire if a non-zero FRP value is reported in GFAS. The $0.1° \times 0.1°$ grid information of GFAS for the years 2005–2011 is transferred to the ECHAM6-HAM2 T63 grid by combining GFAS FRP values for each individual fire to fixed FRP bins.

Table 2.1 illustrates the used FRP bin scheme. The plume height parametrization is run only once within a grid cell for each FRP bin. With a maximum of 41 FRP bins considered instead of running the plume height parametrization for each individual fire of the GFAS data set at every grid cell, the application of the FRP bin scheme reduces

the computational costs for the plume height parametrization calculations by more than 95 %. The FRP bin scheme represents a conceptual approach to implement a simplified fire intensity distribution into a global model. The limitation of 41 FRP bins was chosen for technical reasons related to the specific input data format of the ECHAM6 model. The FRP value of bin 1 (0–10 MW) represents the individual daily mean for the FRP in a particular grid cell, because the variations of the FRP bin 1 values cover several orders of magnitude (10^{-6} to 9.9 MW). For the FRP bins 2–26, a mean FRP value is applied which represents the mean FRP of all fires in this data set for the entire period 2005–2011. Due to the importance of intense fires with FRP values larger than 1000 MW, each of these fires is treated individually and the specific GFAS FRP value is used to calculate the plume height (FRP bins 27–41). For 2 days in the 2005–2011 period, more than 15 fires with FRP values larger than 1000 MW could be found in one specific grid cell and thus the FRP bins 27–41 are not sufficient. In this case the redundant fires were shifted to neighboring grid cells.

Due to the damping factor γ in Eq. (2.2), the small changes in FRP on the order of 0–5 % introduced by application of the FRP bin scheme do not alter plume heights simulated by the SP by more than a few meters. Thus, although the FRP bin scheme represents a simplification of the FRP distribution, the loss of accuracy in global plume height distributions is negligible.

In contrast to the GFASv1.1 data set we apply in this study, Sofiev et al. (2013) used MODIS MOD14 level 2 FRP data for the preparation of a plume height climatology. The relative frequency of total FRP per fire for GFAS and MODIS MOD14 level 2 thermal anomalies is presented in Fig. 2.1 together with the frequency distribution of the MPHP. We group individual MODIS FRP pixels, which have a distance smaller than 3 km to the next fire pixel, to one fire, because in many cases individual MODIS MOD14 level 2 thermal anomalies are not connected although they belong to the same fire. The method of grouping individual MODIS pixels has successfully been applied by Henderson et al. (2010). The advantage of GFAS over MODIS FRP is the assimilation technique applied in GFAS that produces a considerable fraction of fires which are below the MODIS FRP detection limit and thus not included in the MODIS MOD14 data set. Figure 2.1 clearly demonstrates the large number of low-intensity fires which is included in GFAS, but not represented in MODIS. MPHP plumes are based on MODIS fire counts, but have been selected manually. Therefore, the FRP frequency distribution of small fires in the MPHP data set is shifted towards more intense fires which are easier to identify by eye. As such the evaluation of the SP using the MPHP data set is of limited significance, because small fires are underrepresented.

2.2.5 Model setup for evaluation of the plume height parametrization

Sofiev et al. (2012) have already shown that their plume height parametrization offers a generally reasonable individual performance, if the parametrization is forced with meteorological input data from ECMWF reanalysis data. Here, we evaluate the SP implemented into the ECHAM6 general circulation model. For long-term climate simulations, the individual plume height performance is less important than the statistical performance

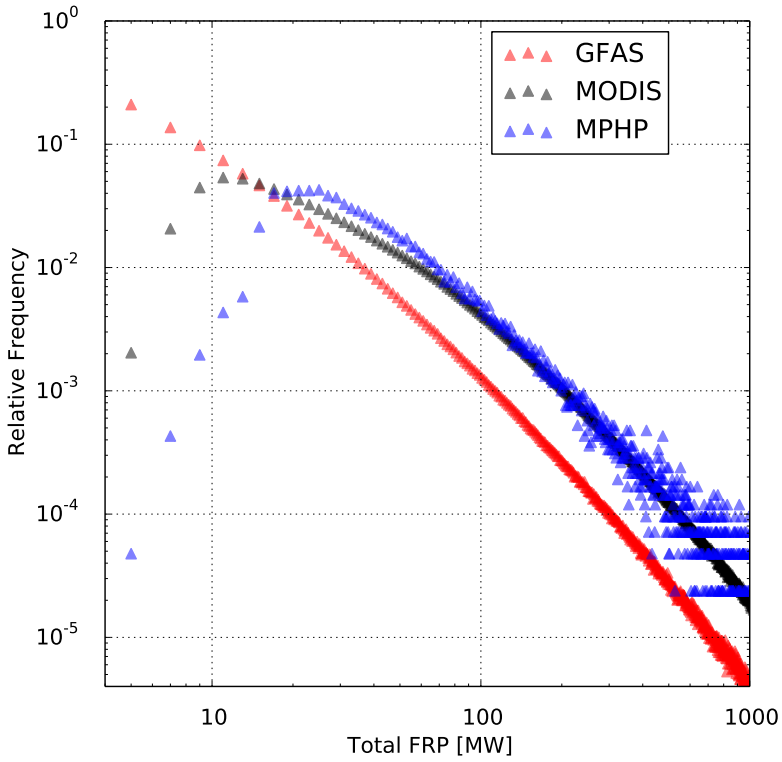

Figure 2.1: Relative frequency of total FRP per fire for MODIS, MPHP and GFAS data. MODIS refers to total FRP of grouped MOD14 level 2 thermal anomalies which feature distances of 3 km or less to neighboring fire pixels. GFAS data (version 1.1) is provided as daily mean total FRP of $0.1° \times 0.1°$ individual grid cells. MPHP data refer to the total FRP of manually selected MODIS daytime fires.

of the global plume height distribution. Therefore, we do not force the ECHAM6 model with reanalysis data, but apply free model runs with prescribed sea surface temperature. Moreover, we quantify FRP uncertainties in more detail than previously done by Sofiev et al. (2012). The SP is run offline based on the meteorological parameters from the ECHAM6 output and FRP from the MPHP data set as described in Sect. 2.2.3. We run ECHAM6 simulations with prescribed AMIP-II sea surface temperature for 2000–2010 to generate a climatology of meteorological input parameters required in the SP. As we expect only a minor impact of aerosol emissions on the meteorological parameters which determine the plume height and as GFASv1.1 data are only available for 2005–2011, we do not use the HAM2 aerosol module for the SP evaluation experiments. In total, the SP is run for a selection of 6942 MPHP plumes. To take into account the FRP uncertainties of 30 % in the MPHP data set, we run the SP additionally for fire intensity values of $0.7 \times$ FRP and $1.3 \times$ FRP. For each plume we test the standard SP (EVAL-SOFIEV-1) as well as the two-step iteration scheme (EVAL-SOFIEV-2) described in Sect. 2.2.2. The SP is run at the particular day when the plume was reported in the MPHP. To estimate plume heights in favorable meteorological conditions, we additionally simulate the plume heights at each day of the month and analyze the upper 25 % of all plumes within a month.

This simulation is called EVAL-SOFIEV-1-METEO. A summary of all simulations for the evaluation of the SP is provided in Table 2.2.

Table 2.2: Setup of simulations for evaluation of various implementations of the Sofiev plume height parametrization. Each version of the parametrization is additionally run with FRP values of ±30 % to estimate the impact of FRP uncertainties on the plume heights. See text for a detailed description of the individual simulation set-ups.

Simulation Name	**Plume Height Parametrization**	**Meteorology**	**FRP from MPHP**
EVAL-SOFIEV-1	Sofiev 1-step	day of obs	original
EVAL-SOFIEV-2	Sofiev 2-step	day of obs	original
EVAL-SOFIEV-1-METEO	Sofiev 1-step	25 % most favorable cond.	original
EVAL-SOFIEV-MODIFIED	Sofiev 1-step + FRP corr.	day of obs	tuning for plumes $> H_{deep}$

Sofiev et al. (2012) found a tendency of the SP to underestimate particularly high plumes, although the plume height spectrum was not subject to a more detailed analysis. There might be various factors which contribute to an underestimation of high plumes including low fire emissivity at 4 µm and an underestimation of FRP due to the smoke opacity effect. Investigations by Schroeder et al. (2014) who compared MODIS FRP data to the Autonomous Modular Sensor (AMS) airborne multi-spectral imaging system indicate that MODIS underestimates the FRP of high-intensity fires. For a particular fire of approximately 500 MW, the underestimation of surface FRP was found to be nearly 50 %. For a smaller fire of 72 MW (detected by AMS), the surface FRP bias was roughly 20 %. There is a general tendency of MODIS to underestimate FRP for high plumes due to the smoke which decreases the detectability of the thermal anomalies below the smoke. This opacity effect of smoke plumes has been described by Kahn et al. (2008). As we use direct MODIS FRP for our plume height simulations, we expect similar underestimations of FRP in our plume height calculations.

Peterson and Wang (2013) and Peterson et al. (2014) investigated MODIS FRP data and found sub-pixel information to be useful for the prediction of high-altitude injections. However, so far there is no global data set available that provides this sub-pixel data for a wide range of fire sizes and intensities. Even though the magnitude of the underestimation cannot be quantified on the global scale, satellite pictures of the MPHP data set clearly indicate that the underestimation of MODIS FRP tends to increase with plume height. This holds especially for calm conditions and pyro-cumulus events as one can see for a number of plumes in the MPHP data set (personal communication with David Nelson). To take into account this significant FRP underestimation of particularly strong fires, we apply an empirical FRP correction of the SP which tunes deep plumes higher than a threshold H_{deep} towards the observations by replacing the FRP P_{f} in Eq. (2.2)

Table 2.3: Setup of global plume height pattern simulations. All simulations are nudged towards observations every six hours; simulation period is 2005–2011.

Simulation Name	**Plume Height Parametrization**	**Diurnal Cycle of FRP**	**Emission Distribution**
HAM2.2-STANDARD	PBL + 2 model layers	NO	25 % into FT, 75 % into PBL
SOFIEV-ORIGINAL	SOFIEV (Original)	NO	const. mass mixing ratio
SOFIEV-DCYCLE	SOFIEV (Original)	YES	const. mass mixing ratio
SOFIEV-2X-FRP	SOFIEV (Original, 2xFRP)	NO	const. mass mixing ratio
SOFIEV-MODIFIED	SOFIEV (Modified)	YES	const. mass mixing ratio

with P_{f}^{*}, where

$$P_{\mathrm{f}}^{*} = P_{\mathrm{f}} \times \left(\frac{H_{\mathrm{p}}}{H_{\mathrm{deep}}} \right)^{\varepsilon} . \tag{2.6}$$

We empirically vary ε and define H_{deep} based on the statistical performance of EVAL-SOFIEV-1 evaluated with the MPHP data set. The empirically determined best performance values of ε are subsequently used for the simulation EVAL-SOFIEV-MODIFIED (see Table 2.2).

2.2.6 Model setup for simulation of global plume height patterns

We run the ECHAM6-HAM2 general circulation model as described in Sect. 2.2.1 in nudged mode (ERA-INTERIM data) for the years 2004–2011 to simulate global plume height patterns. Due to the limited availability of GFASv1.1 (years 2005–2011) plume heights for 2004 are driven by 2008 GFAS fire intensity data. The year 2004 serves thereby solely as model spin-up and is excluded from our analysis. In total we run five ECHAM6-HAM2 simulations: one reference simulation "HAM2.2-STANDARD", for which we use the standard plume height distribution scheme and four simulations which represent different configurations of the SP (Table 2.3).

Simulation SOFIEV-ORIGINAL is based on the original SP as described in Sofiev et al. (2012) and evaluated in simulation EVAL-SOFIEV-1. In SOFIEV-DCYCLE, we apply a simplified diurnal cycle according to Zhang et al. (2012b), which distributes 80 % of the FRP constantly during daytime (08:00–18:00 LT) and the remaining 20 % during nighttime (18:00–08:00 LT). In simulation SOFIEV-MODIFIED, we use the results from the plume height parametrization evaluation to tune the SP. Vertical emission distributions in experiment HAM2.2-STANDARD are implemented as described in Sect. 2.2.1, while

all SOFIEV simulations apply a constant mass mixing ratio from the surface to the top of the plume.

Simulation SOFIEV-2X-FRP is a sensitivity scenario of more intense fires in a warmer climate and serves as a sensitivity test. A climate-change-induced increase in fire activity has been found based on climate projections for the end of the 21st century particularly for boreal regions, (e.g., Stocks et al., 1998; Kloster et al., 2012; de Groot et al., 2013). Since no global estimates of a future intensification in FRP are available, we only consider a hypothetical global doubling in fire intensity in simulation SOFIEV-2X-FRP.

2.3 Plume height parametrization performance

This section presents the evaluation of the various versions of the SP described in Sect. 2.2.5. Table 2.4 provides statistical values of the global plume height distribution for all versions of the SP and the observational MPHP data set. Parametrization EVAL-SOFIEV-1 shows basic agreement with the observed spectrum for a wide range of plume heights. The global mean plume height of EVAL-SOFIEV-1 (1389 ± 572 m) is very close to the observed global mean of 1382 ± 702 m.

However, there is a general tendency of the SP to overestimate low plumes and to underestimate high plumes. Similar problems to reproduce particularly high as well as low plumes have been reported for other plume rise parametrizations by Val Martin et al. (2012).

The uncertainties in plume heights introduced by the $\pm 30\,\%$ uncertainty in the FRP impact the mean plume heights by less than 100 m. The two-step SP (EVAL-SOFIEV-2) provides a slightly better representation of the plume height variations, but the one-step SP holds a smaller positive model bias for low plumes and a better representation of extraordinarily high plumes. For favorable meteorological conditions (parametrization EVAL-SOFIEV-1-METEO), the increase in plume heights compared to EVAL-SOFIEV-1 ranges between 200 and 400 m except for the highest plumes which significantly exceed this range (1250 m for the maximum plume height). Compared to the FRP uncertainty, the meteorological parameters turn out to be more important for plume heights on the global scale. Due to the simplified representation of plume buoyancy in the Sofiev formula, the interpretation of these findings has to be taken with care, but the setup of our simulations does not allow for a more detailed analysis. A Kolmogorov-Smirnov (KS) test indicates that the best statistical performance is provided by EVAL-SOFIEV-1, for both, the complete distribution, as well as the uppermost 40 percentiles. The uppermost 40 percentiles serve best for the KS test, because for these percentiles the cumulative probability distribution of EVAL-SOFIEV-1 continuously exceeds the MPHP distribution.

Table 2.4: Statistical analysis of different versions of the Sofiev plume height parametrization implemented in ECHAM6. The KS tests describe results for a Kolmogorov-Smirnov test, the square root error is shown as cumulative sum over the cumulative probability function. Uncertainties of mean heights indicate one SD.

Plume Height Dataset	**MPHP OBS**	**EVAL-SOFIEV-1**	**EVAL-SOFIEV-2**	**EVAL-SOFIEV-1-METEO**	**EVAL-SOFIEV-MODIFIED**
mean height [m]	1382±702	1389±572	1517±637	1651±599	1411±646
mean height FRP +30 % [m]	–	1478±616	1603±668	1750±649	1511±717
mean height FRP -30 % [m]	–	1279±519	1403±596	1554±616	1292±567
10th percentile [m]	651	789	834	1011	789
25th percentile [m]	892	988	1048	1231	988
50th percentile [m]	1248	1280	1402	1544	1280
75th percentile [m]	1713	1666	1834	1937	1688
90th percentile [m]	2271	2123	2282	2421	2218
95th percentile [m]	2671	2465	2675	2782	2621
99th percentile [m]	3709	3193	3629	3576	3556
max height [m]	11986	6153	5620	7404	7786
top 10 plumes [m]	6122±2008	5153±596	5129±308	5521±908	6235±881
KS test d value	–	0.081	0.117	–	0.081
KS test d value upper 40 %	–	0.075	0.249	–	0.034
cumulative square root error	–	0.161	0.300	–	0.034

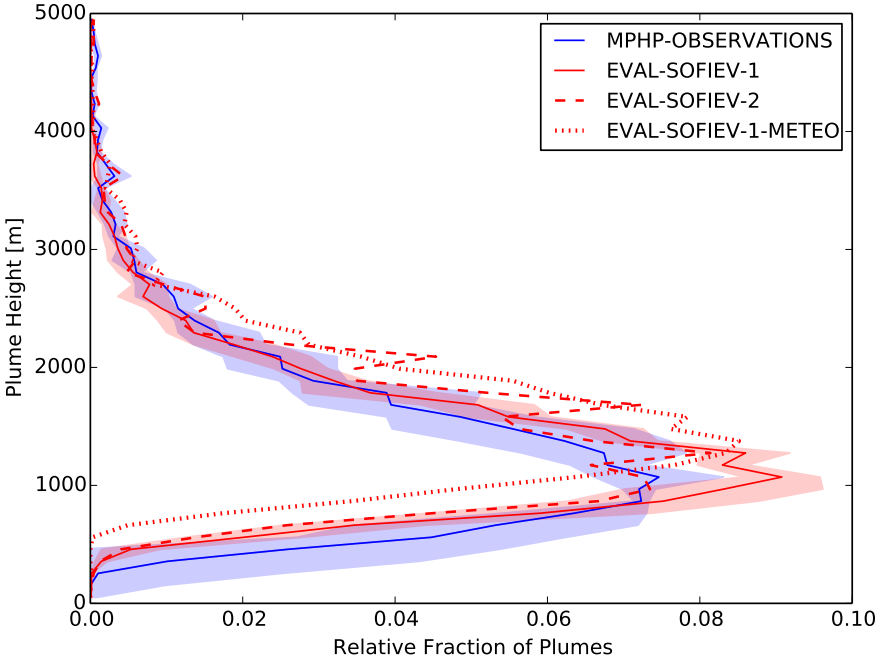

Figure 2.2: Global mean plume height distribution for different plume height parametrizations and MPHP observations. Blue shading represents uncertainties of ±200 m in the plume height observations, red shading represents a ±30 % FRP uncertainty applied for the plume height parametrizations.

Figure 2.2 visualizes the vertical plume height distribution for the different versions of the SP. While the EVAL-SOFIEV-1-METEO parametrization lies significantly above the observations for the entire plume height range below 4 km, EVAL-SOFIEV-1 matches the uncertainty range of the observations for a large part of the plume height spectrum. The spikes in the EVAL-SOFIEV-2 distribution originate from the two-step algorithm which tends to shift plumes away from levels of the PBL height. As particularly high plumes are in many cases linked to large emission injections, these plumes require special attention in the context of global climate modeling. Based on empirical variations of the tuning parameters in parametrization EVAL-SOFIEV-MODIFIED (see Eq. 2.6), we found the best statistical performance for $\varepsilon = 0.5$ and $H_{\text{deep}} = 1500\,\text{m}$. The correction of FRP for deep plumes significantly improves the overall plume height parametrization performance on the global scale (see Table 2.4). The cumulative square error of the entire distribution is decreased from 0.16 for parametrization EVAL-SOFIEV-1 to 0.03 for parametrization EVAL-SOFIEV-MODIFIED. While the mean plume height of EVAL-SOFIEV-MODIFIED ($1411 \pm 646\,\text{m}$) does not change substantially compared to EVAL-SOFIEV-1 ($1389 \pm 572\,\text{m}$), the maximum plume heights are increased from 6.1 to 7.8 km and the KS test d value for the uppermost 40 percentiles is reduced by $\approx 50\,\%$.

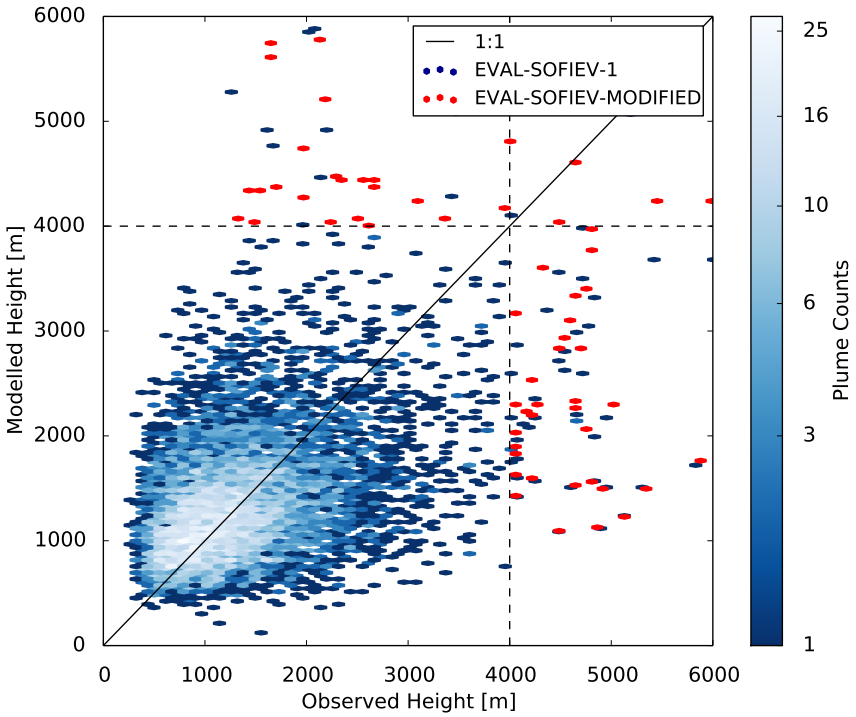

Figure 2.3: Performance of the 1-step Sofiev plume height parametrization (EVAL-SOFIEV-1) for plumes below 6 km. Honeycomb colors indicate the number of plumes in a specific 100 m height bin for EVAL-SOFIEV-1. Red honeycombs represent plumes for EVAL-SOFIEV-MODIFIED. For reasons of clarity, only EVAL-SOFIEV-MODIFIED plumes above 4 km are shown.

Figure 2.3 shows the frequency of plume heights in specific 100 m bins for parametrization EVAL-SOFIEV-1 (0–6 km) and EVAL-SOFIEV-MODIFIED (4–6 km only). The large majority of low plumes are adequately represented by EVAL-SOFIEV-1, but for high plumes > 4 km, the FRP correction applied in EVAL-SOFIEV-MODIFIED is particularly important. While the number of plume heights > 4 km is 38 in the observational MPHP data set (out of 6942 plumes in total), the number of plumes > 4 km is increased from 12 in simulation EVAL-SOFIEV-1 to 33 in simulation EVAL-SOFIEV-MODIFIED.

Figure 2.4 presents a global map of the mean plume height bias simulated by EVAL-SOFIEV-1 compared to MPHP observations for all analyzed plumes. Very similar patterns apply for parametrization EVAL-SOFIEV-MODIFIED as the FRP correction introduced in EVAL-SOFIEV-MODIFIED only marginally effects the mean plume heights. Although significant individual over- and underestimations on the grid box scale are observable, there is no clear region-specific bias pattern observable in the extra-tropics. In tropical South America, plumes generally tend to be slightly overestimated, but in other parts of the tropics (e.g., Southeast Asia) tropical plumes are captured very well by the SP. A more detailed analysis shows that the positive model bias in tropical South America is primarily related to plumes with heights smaller than 3 km. Due to the vast majority of these tropical low plumes injecting emissions into the well-mixed PBL, this bias is generally of limited importance for the emission height climate impact.

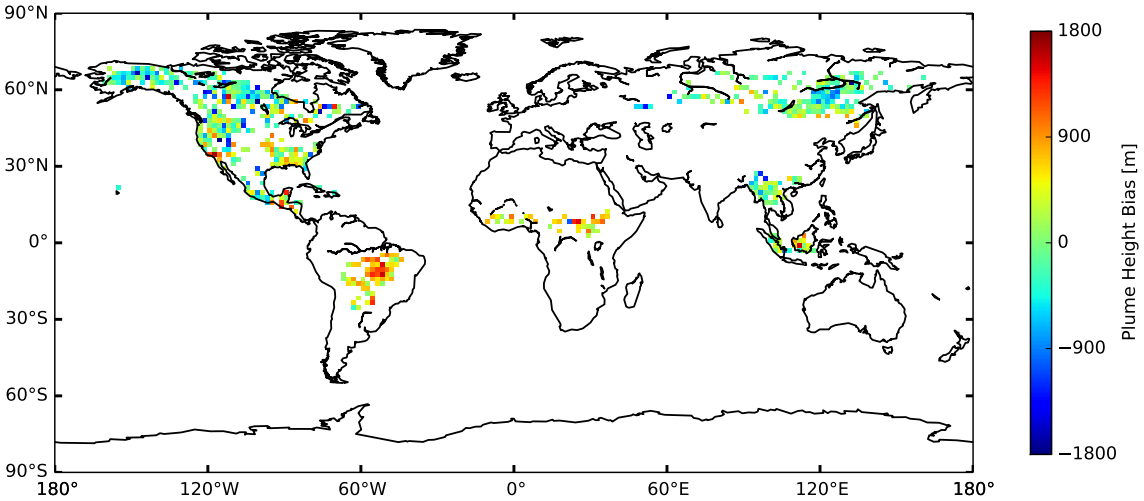

Figure 2.4: Mean plume height bias of simulation EVAL-SOFIEV-1 for 2001–2009 compared to the observational MPHP data set (EVAL-SOFIEV-1 minus MPHP). Blue colors indicate underestimation of plume heights by the model, red colors indicate overestimation of plume heights by the model. The large majority of grid boxes contains more than one individual plume; in these cases averaged biases are shown. The large areas of white colors, e.g. in Europe and Australia, represent the limited global coverage of the MPHP data set as no plumes are available in these regions.

2.4 Global plume height patterns

In the next sections, global plume height patterns simulated by the various plume height implementations in ECHAM6-HAM2 are presented. All simulations are based on FRP data as reported by the GFASv1.1 data set. We analyze global and regional differences in plume heights, impacts of a diurnal and seasonal cycle and the fraction of free tropospheric injections.

2.4.1 Global patterns of mean and maximum plume heights

Table 2.5 shows a comparison of global plume height statistics for all five simulations introduced in Sect. 2.2.6. We apply a linear weighting of plume heights with FRP. The weighting becomes particularly important for global mean plume height values as the large number of small fires in GFASv1.1 dominates the plume height spectrum. Thus, intense fires injecting large amounts of emissions are more adequately represented in global plume height statistics.

The ECHAM6-HAM2 standard plume height implementation (PBL height +2 model layers) results in a mean global plume height of 2798 ± 813 m. This plume height value is considerably higher than all mean plume heights in the various versions of the SP, which range from 1327 ± 457 m (SOFIEV-ORIGINAL) to 1559 ± 577 m (SOFIEV-MODIFIED). The introduction of a diurnal cycle in FRP (SOFIEV-DCYCLE), as well as the additional ECHAM6-HAM2.2-specific FRP correction for high plumes, does not impact mean plume heights by more than 450 m except for the 99th percentile. For a doubling in FRP (simulation SOFIEV-2X-FRP), mean plume heights range between the SOFIEV-ORIGINAL

simulation and the SOFIEV-DCYCLE simulation. Daytime plumes in SOFIEV-DCYCLE and SOFIEV-MODIFIED are weighted approximately 6 times greater than nighttime plumes due to their higher FRP values. However, although the differences between the various versions of the SP are very limited for 99 % of all plumes, the disproportionately important 1 % of the highest plumes show larger differences.

Table 2.5: Plume height characteristics for various plume height implementations. All values represent global means for the time period 2005–2011. Uncertainty estimates for mean TOP 100 plumes represent one standard deviation (SD). A description of the simulation set-ups is provided in Table 2.3.

Simulation Name	**HAM2.2-STANDARD**	**SOFIEV-ORIGINAL**	**SOFIEV-DCYCLE**	**SOFIEV-MODIFIED**	**SOFIEV-2X-FRP**
mean height [m]	2798±813	1327±457	1526±517	1559±577	1500±549
10^{th} percent. [m]	1784	833	956	956	924
25^{th} percent. [m]	2173	1012	1164	1164	1128
50^{th} percent. [m]	2733	1256	1449	1459	1406
75^{th} percent. [m]	3364	1552	1790	1827	1754
90^{th} percent. [m]	3883	1892	2167	2255	2169
95^{th} percent. [m]	4199	2161	2461	2607	2511
99^{th} percent. [m]	4798	2831	3195	3543	3356
max height [m]	14408	6386	7121	8701	7788
Mean TOP 100 [m]	9510±1027	4786±389	5676±477	6782±632	5755±485

Figure 2.5 presents maximum values of hourly plume heights for all simulations from 2005 to 2011. On average, plume heights simulated by the SP show significantly smaller maximum plume heights than the plume heights simulated by HAM2.2-STANDARD. By taking into account not only the PBL height but also the fire intensity, the SP represents a more heterogeneous pattern of plume heights (see Fig. 2.5a–d). The HAM2.2-STANDARD plume heights follow a distinct gradient from the Equator to the poles due to their dependence on PBL height. In contrast to the HAM2.2-STANDARD scenario, SP maximum plume heights are generally lower than 4 km in many regions. Plume heights greater than 4 km are simulated in the subtropical and tropical savannah, in remote mid-latitudes and in boreal regions. The differences in plume heights between the various versions of the SP (Fig. 2.5b–d) are much smaller than the differences to HAM2.2-STANDARD (Fig. 2.5a). The implementation of a diurnal cycle (SOFIEV-DCYCLE, Fig. 2.5c) introduces a significant mean plume height increase in regions of high fire intensity. For SOFIEV-MODIFIED, the FRP correction for plumes > 1500 m leads to a further increase in plume heights. In contrast to the SOFIEV-ORIGINAL simulation, for SOFIEV-MODIFIED a very small fraction of individual plumes reaches plume heights of

more than 7 km. In parts of Australia, boreal Canada and Siberia, some high plumes simulated by SOFIEV-MODIFIED rise substantially above the HAM2.2-STANDARD plume heights.

Sofiev et al. (2013) presented zonal mean injection profiles and regional maximum plume heights of 5.5 km with the majority of plumes injecting into the lowest 1000 m. In contrast to our study, the results by Sofiev et al. (2013) were based on MODIS MOD14 FRP data and were therefore lacking a significant fraction of small fires which is included in GFASv1.1. However, the dominance of emission injections into the lowest 1–2 km is observable in both studies. The tuning of high plumes applied in SOFIEV-MODIFIED leads to a small fraction of plume heights above 6–7 km which is not included in Sofiev et al. (2013), although such high plumes are reported in the MPHP data set. In the MPHP data set, one single, particularly high plume even exceeds a plume height of 10 km and lies thus beyond the spectrum of our SP simulations.

Gonzi et al. (2015) applied a modified version of the 1-D plume rise model by Freitas et al. (2007) for global modeling of plume heights for the year 2006 and analyzed regional plume height distributions in Indonesia, North America, Africa and Siberia. The authors found a very limited number of plumes (approximately 10–100 plumes for 2006) which exceeded injection heights by more than 5 km above the PBL height. Due to differences in model resolution, FRP inventories and temporal resolution, the study by Gonzi et al. (2015) is not directly comparable to our simulations. Nevertheless, the magnitude of the highest plumes shows basic agreement with simulation SOFIEV-MODIFIED.

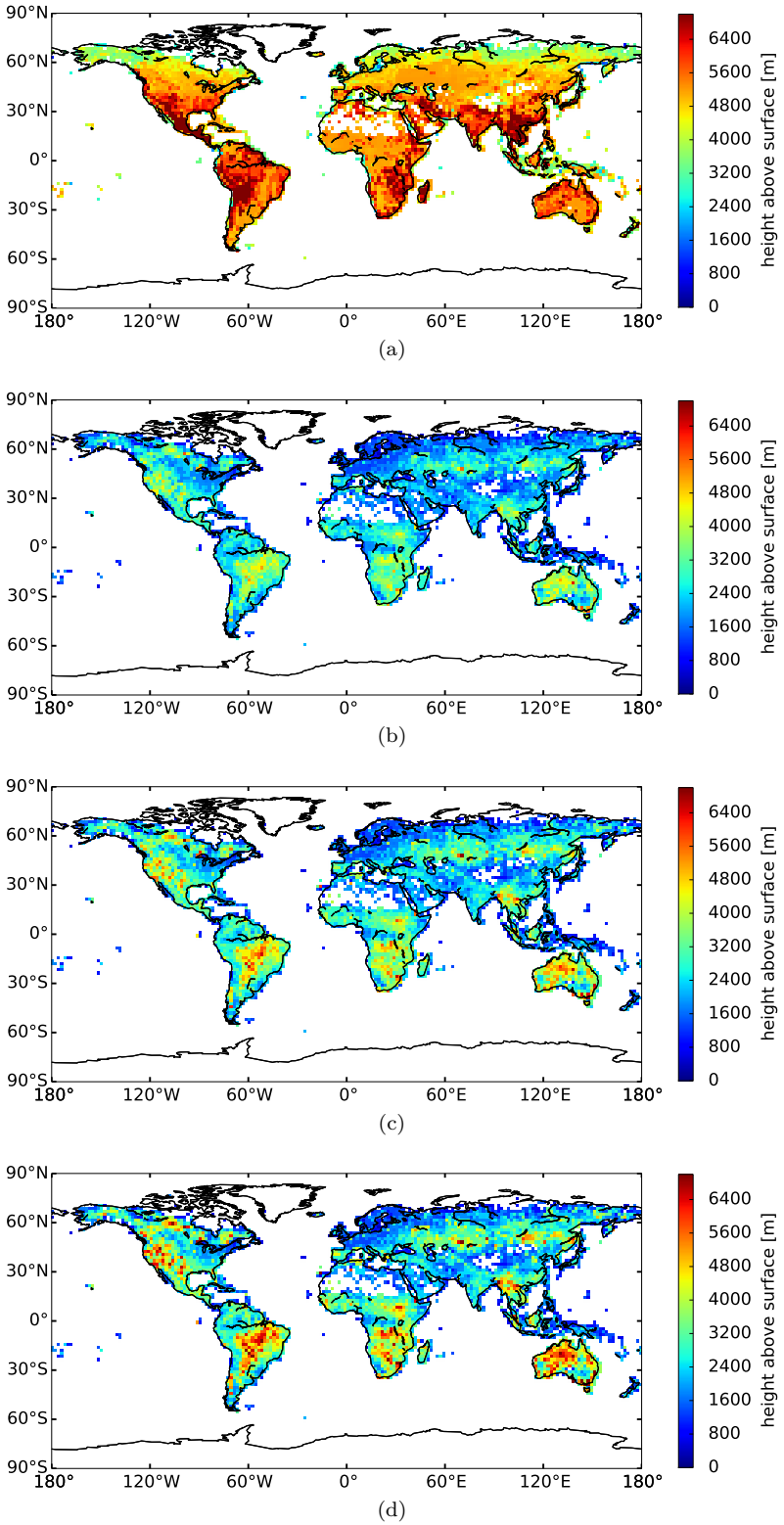

Figure 2.5: Maximum plume heights for simulations HAM2.2-STANDARD **(a)**, SOFIEV-ORIGINAL **(b)**, SOFIEV-DCYCLE **(c)**, SOFIEV-MODIFIED **(d)**. Plume heights for **(a)** represent standard plume heights in ECHAM6-HAM2.2, plume heights in **(b)** to **(d)** are based on various versions of the Sofiev plume height parametrization. For a detailed description, see Sect. 2.2.6.

2.4.2 Vertical emission distributions

For all SP simulations we assume a vertical emission distribution of constant mass mixing ratio in all levels below the top plume height. In the HAM2.2-STANDARD simulation a fixed fraction of the emissions (25 %) is injected in the next two layers above the PBL (see Sects. 2.2.1 and 2.2.6). Figure 2.6 illustrates the vertical emission distributions of all simulations as 7 year global means. All versions of the SP are emitting the major fraction of the emissions below 800 hPa with small differences between these simulations. For simulation HAM2.2-STANDARD, a considerably larger emission fraction is injected into layers 3–5 km above the surface.

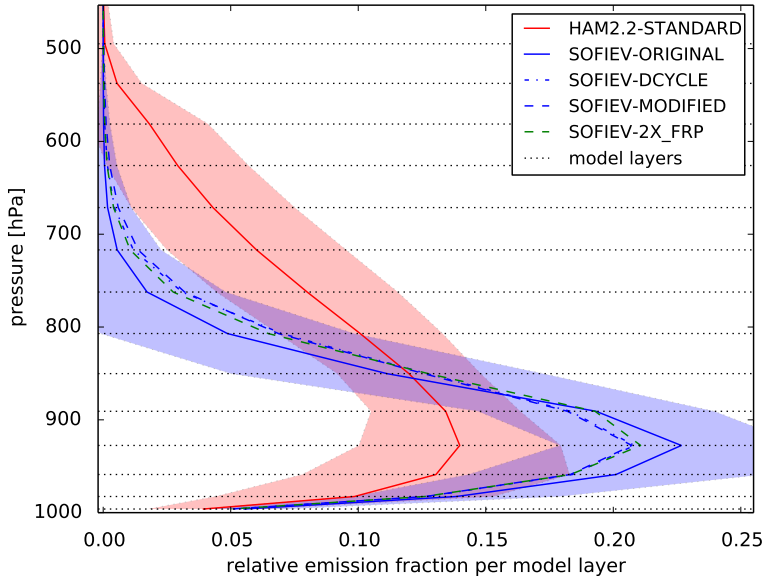

Figure 2.6: Globally averaged vertical emission distribution of wildfire emissions for different emission height parametrizations 2005–2011. All emission distributions are weighted with FRP, i.e. strong fires contribute disproportionately high to the distribution, see text Sect. 2.4.1. Red and blue shadings indicate one SD of simulation HAM2.2-STANDARD respectively SOFIEV-ORIGINAL. Note that the SOFIEV-DCYCLE and SOFIEV-MODIFIED lines largely overlie for pressure levels >700 hPa. For a detailed description of the simulation set-ups, see Table 2.3.

The SP simulations are basically in line with the observational study of Jian and Fu (2014) who found on average only 45 % of smoke MISR pixels above 1 km. Kipling et al. (2013) showed that, for prescribed standard emission profiles, ECHAM6-HAM2 generally overestimates BC in the upper troposphere over the Pacific. This model bias might to some extent be related to too high plumes in ECHAM6-HAM2 standard. A doubling of FRP is not found to considerably change the vertical emission distributions compared to simulation SOFIEV-ORIGINAL.

2.4.3 Diurnal and seasonal cycles

The purely PBL-related plume height variations in HAM2.2-STANDARD result in a distinct diurnal cycle of plume heights (see Fig. 2.7). The SP, which also takes into account

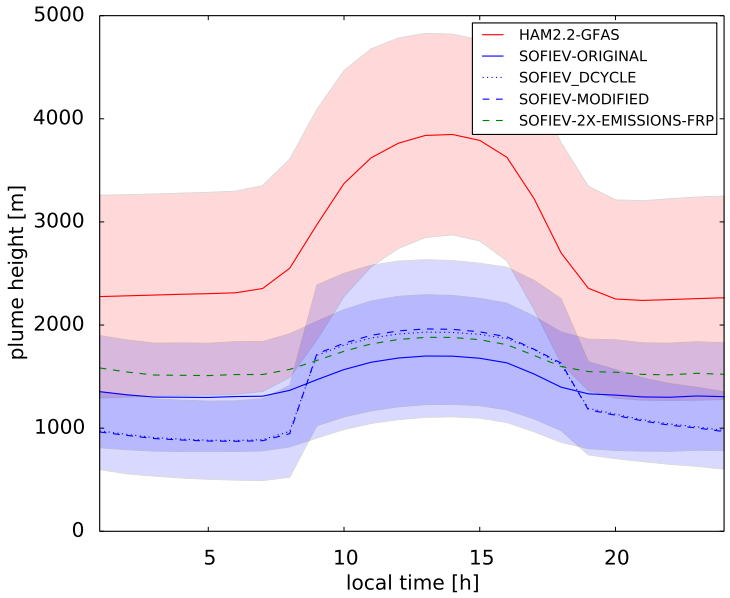

Figure 2.7: Global mean diurnal cycle of plume heights for different plume height implementations. Shadings indicate one SD.

the FRP and Brunt–Väisälä frequency, shows a less pronounced diurnal cycle. Overall, simplified diurnal variations in FRP (simulation SOFIEV-DCYCLE) turn out to impact the overall diurnal cycle by 200–500 m and are therefore of similar importance as diurnal variations in PBL and Brunt–Väisälä frequency. The limited impact of a diurnal cycle in FRP in all SOFIEV simulations coincides with the results from Gonzi et al. (2015) who showed that the differences in CO profiles are only marginally influenced except for the lowest 1–2 km when diurnal FRP variations are accounted for. For analysis of the simulated seasonal cycle in plume heights, we choose North America (30–60° N, 90–120° W) as a region with a distinct fire activity peak during the northern hemispheric summer and tropical Africa (0–15° N, 15° W–45° E) as a region of maximum fire activity in southern hemispheric summer conditions.

Figure 2.8 shows seasonal variations of the HAM2.2-STANDARD, SOFIEV-ORIGINAL and SOFIEV-DCYCLE simulations. In both regions, seasonal variations of area averaged plume heights are not very pronounced, since a large number of small fires dominates the mean plume heights. There is a distinct seasonal cycle in the maximum individual daily plume heights observable in the SOFIEV simulations for North America and – though less pronounced – also for Africa. This seasonal cycle in plume heights is mainly related to the seasonal cycle in individual FRP values peaking in the summer season. For HAM2.2-STANDARD, the seasonal cycle is not represented because PBL heights do not show distinct seasonal patterns in those regions.

2.4.4 Fraction of free tropospheric injections

In HAM2.2-STANDARD, all plumes are prescribed to reach or exceed PBL height. In all versions of the SP, the fraction of plumes that reach the FT is significantly smaller than

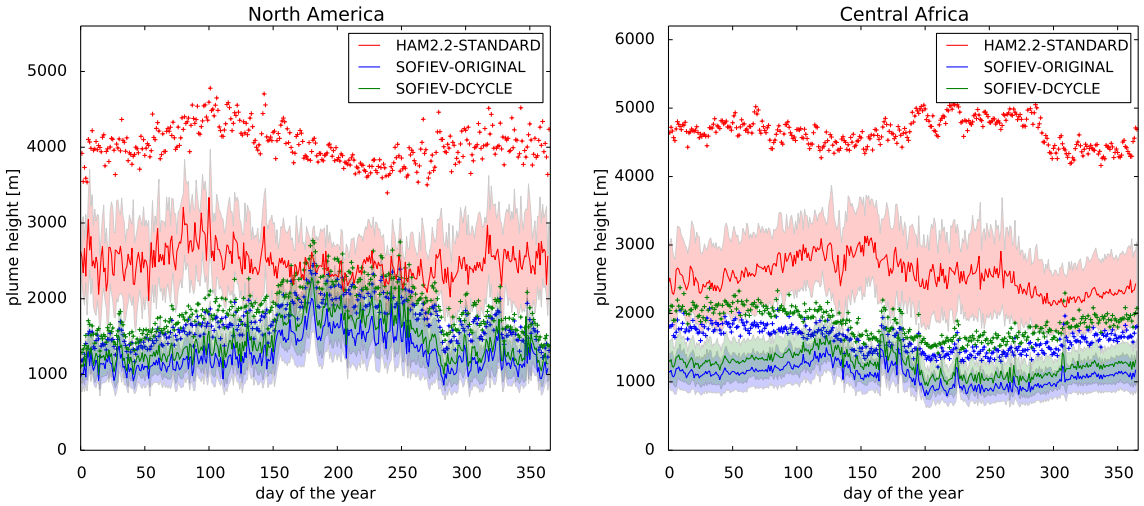

(a) (b)

Figure 2.8: Seasonal cycle of daily mean plume heights for North America (left plot **a**) and Central Africa (right plot **b**). Shading represents one SD, crosses indicate maximum individual mean daily values in these regions. See text and Table 2.3 for a more detailed description of model simulations HAM2.2-STANDARD, SOFIEV-ORIGINAL and SOFIEV-DCYCLE.

100 % (see Table 2.6). The simulated global fraction of FT plumes ranges between 9.7 ± 1.4 and 15.0 ± 2.0 %. For daytime plumes, which emit 80 % of the total wildfire emissions, the fraction of FT plumes is substantially smaller (3.7–5.5 %).

A similar fraction of 4 % daytime plumes reaching the FT was presented by Tosca et al. (2011) for Indonesia. For North America Val Martin et al. (2010) found a fraction of 4–12 %. In contrast, Diner et al. (2008) and Mims et al. (2010) found values of 26 % for North America, and 30 % for Australia, respectively. A slightly smaller fraction of North American FT injections (14–22 %) has also been identified by Gonzi et al. (2015).

Table 2.6: Global fraction of FT plumes for all-day (0–24 LT), daytime (8–18 LT) and nighttime (18–8 LT) plume heights. Uncertainties indicate SDs of day to day variations.

Simulation Name	**FT Fraction 0–24 LT,**[%]	**FT Fraction 8–18 LT** [%]	**FT Fraction 18–8 LT** [%]
SOFIEV-ORIGINAL	11.9 ± 1.7	3.7 ± 0.7	17.8 ± 2.3
SOFIEV-DCYCLE	9.7 ± 1.4	5.2 ± 0.9	12.8 ± 1.7
SOFIEV-2X-FRP	15.0 ± 2.0	5.5 ± 1.0	21.6 ± 2.7
SOFIEV-MODIFIED	9.7 ± 1.4	5.2 ± 1.0	12.8 ± 1.7

2.5 Comparison to other plume height parametrizations

The SP represents a simple, semi-empirical plume height parametrization that takes into account fire intensity as well as meteorological parameters for calculation of plume heights. This parametrization does not explicitly account for fire size, wind drag, entrainment and the number of updraft cores which have been shown to influence plume heights (Freitas et al., 2007, 2010; Liu et al., 2010a; Rio et al., 2010). But for long-term climate modeling, the computational costs for the implementation of more complex analytical models are disproportionate to the benefits. Nevertheless we compare the plume heights calculated by the SP to the widely used 1-D plume height model by Freitas et al. (2007) for a limited period of time. We use fire and meteorological data from the Monitoring Atmospheric Composition and Climate (MACC) project for the period 1 January 2014 to 13 July 2014. The MACC-II data were most suitable for this comparison, because a modified version of the Freitas plume rise model (PRM-MODEL) (Freitas et al., 2007; Gonzi et al., 2015) had already been implemented in MACC-II. Therefore, the required additional effort for the implementation of the SP was very limited. As the PRM-MODEL requires the fire size of each fire which is not provided in GFASv1.1, it was unfortunately not possible to run the PRM-MODEL simulations for our ECHAM6-HAM2.2 experiment set-ups.

The PRM-MODEL provides entire detrainment profiles, but for comparability to the SP we only analyze the mean height of maximum injections. In the PRM-MODEL, maximum injection heights are defined as the average of the levels for which the detrainment is $> 50\,\%$ of the maximum detrainment. Moreover, the PRM-MODEL output is assimilated to fill observational gaps as described by Kaiser et al. (2012).

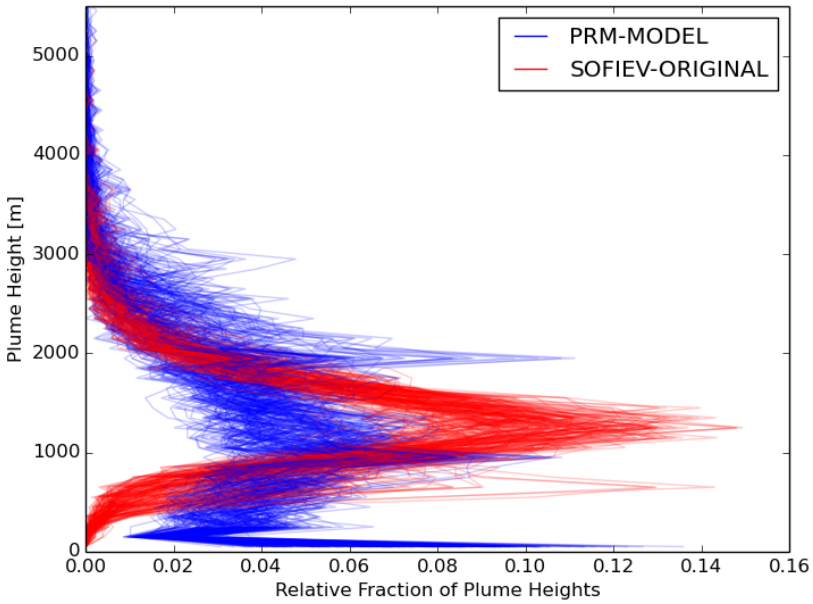

Figure 2.9: Plume height distributions calculated by the PRM-MODEL and the original version of the SP (SOFIEV-ORIGINAL) implemented in MACC-II for 1 January 2014 to 13 July 2014. Each line represents the global mean plume height distribution of a particular day.

The implementation of the PRM model for all individual fires entailed roughly a doubling in computation time for the MACC-II system, whereas the additional computational costs of the SP implementation are negligible. A comparison of global mean daily plume height distributions of the PRM model vs. SP implemented in the MACC-II system is shown in Fig. 2.9. For this period, the PRM model provides a mean plume height of 1287 ± 807 m, for SP the mean is 1392 ± 506 m; the 10th percentile in PRM is only 273 m, whereas it is 809 m in SP; the 95th percentile is 2663 m in PRM and 2322 m in SP; the mean plume height of the highest 100 plumes in the PRM is 7251 ± 466 m, for the SP it is 4406 ± 329 m. Overall the differences between the models are largely restricted to the lowest 500–1000 m within the well-mixed PBL and furthermore to the upper 97–99 percentile. However, a modified SP in MACC to improve occasionally high plumes (which would require additional tuning similar to our FRP correction in simulation SOFIEV-MODIFIED) would shift the plume height distribution to a better agreement with the PRM (see Table 2.5).

2.6 Summary and conclusions

In this study prescribed plume heights in ECHAM6-HAM2.2 have been replaced by the implementation of different versions of a simple, semi-empirical plume height parametrization after Sofiev et al. (2012). In a first step we evaluated the modeled plume height distribution against 6942 plumes of the MPHP data set. Overall the semi-empirical parametrization shows a reasonable performance within the uncertainty range, although low plumes tend to be slightly overestimated and high plumes tend to be underestimated. A statistical–empirical correction for the FRP of high plumes turned out to significantly improve the uppermost 10 % of the plume height spectrum, because this correction compensates the smoke opacity effects which reduce the detectability of FRP for intense fires. For the plume height parametrization used in this study, meteorological conditions impact the plume heights more effectively than uncertainties in FRP. The reliance of plume heights on FRP in the Sofiev parametrization represents a very simplified approach which provides reasonable statistics on the global scale, but it might fail for the prediction of individual plumes.

In a second step we simulated plume heights for fire activity of global coverage for 2005–2011 using FRP reported in the global fire inventory GFASv1.1 (Kaiser et al., 2012) as input for the plume height parametrization. The application of the fire-intensity-dependent plume height parametrization introduced considerable changes to global plume height patterns compared to the ECHAM6-HAM2 standard plume height implementation which solely depends on PBL height. The global mean plume height simulated by the modified Sofiev plume height parametrization is 1559 ± 577 m with a fraction of 3.7 ± 0.7 % of daytime plumes emitting into the FT. The highest 100 plumes reach altitudes of 6.1–8.7 km above the surface. On the global scale, plume heights simulated by the Sofiev plume height parametrization are significantly lower than for ECHAM6-HAM2 prescribed plume heights and show a much more heterogeneous spatial distribution. As a results of the strong damping in the FRP impact on plume heights described by the Sofiev plume height parametrization, a hypothetical doubling in future fire intensity, as well as the im-

plementation of a diurnal cycle in FRP, only marginally increases the vast majority of emission heights. Basic global plume height patterns are rarely affected by these changes in FRP, but for the uppermost 10 percent of all plumes, an average increase in plume heights by 300–500 m is simulated.

The lack of high-resolution plume height data sets of full global coverage remains a limiting factor for the evaluation of plume height parametrizations in climate and Earth system models. Nevertheless, the implementation of an advanced plume height representation into a climate model is an essential step forward to advance the progress in our understanding of the overall fire emission climate impact. The simulations presented in this study form the basis for the investigation of the fire emission height impact on black carbon long-range transport and radiation which we show in the third chapter of this thesis. For subsequent studies without observational FRP data, we will couple the implemented plume height parametrization to a mechanistic interactive fire model (Lasslop et al., 2014) within a global vegetation model (see chapter 4). This will enable the investigation of climate-change-induced future changes in fire intensity and related changes in plume heights.

Chapter 3

Impact of emission heights on atmospheric transport, BC concentrations and radiation

3.1 Introduction

Within the last two decades, comprehensive observational and modeling studies have investigated and quantified the importance of wildfire aerosol emissions for direct, semi-direct and indirect radiative effects and aerosol–cloud precipitation interaction (Haywood and Boucher, 2000; Lohmann and Feichter, 2005; Bowman et al., 2009). The global BC emissions from vegetation fires are estimated to range between 1.7 and 3.0 $\mathrm{Tg\,BC\,yr^{-1}}$, which is equivalent to roughly 30 % of the global total BC emissions including fossil fuels (e.g., Andreae and Merlet, 2001; Reid et al., 2005; Bond et al., 2013). Regardless of the considerable progress that has been made concerning our understanding of the direct, semi-direct and indirect aerosol effects, the ability of recent global climate models to reproduce observations and climate-related changes in carbonaceous aerosol concentrations is very limited (Dentener et al., 2006; Kinne et al., 2006; Koch et al., 2009). Important sources of bias could be identified to arise from large uncertainties in the fire emission inventories, improper transport mechanisms and removal processes (Bond et al., 2013; Schwarz et al., 2013). Long-range transport and removal processes of wildfire aerosol emissions in turn depend to some extent on the emission heights. Samset et al. (2013) published a comprehensive comparison of 12 global aerosol models in the framework of the AEROCOM project. The authors found that most of the AEROCOM models attribute more than 40 % of the BC radiative forcing (RF) to altitudes higher than 5 km, although only 24 % of the BC mass is found above 5 km. Thus, the vertical emission distribution at the time of the wildfire emission release can be identified as a key parameter for the overall radiative impact of wildfire emissions.

In the following, we use the term “plume height” to describe the maximum altitude above the surface at which emissions are released (e.g. prescribed, or calculated by a plume height parametrization). The term “emission heights“ describes the full range of heights at which wildfire emissions are released. “Emission profiles” specify the entire vertical

emission profiles from the surface to the top of the smoke plume.

Although advanced emission height models are available for implementation in global circulation models (e.g., Luderer et al., 2006; Freitas et al., 2007; Rio et al., 2010), there is an ongoing discussion about which degree of complexity in emission height parametrization is required for global Climate Modeling. Due to a lack of observational plume height data sets of global coverage, our knowledge regarding appropriate emission height parametrizations for specific global modeling applications is largely based on short-term or regional studies. By application of inverse Lagrangian modeling techniques, the early studies of Liousse et al. (1996), Wotawa and Trainer (2000) and Spichtinger et al. (2001) found the best matches of modeled aerosol transport to observations for emission distributions between 0 and 2, 0.5 and 3, and 3 and 5 km for BC, CO and NO_x concentrations, respectively. Chen et al. (2009) showed that emission heights are substantially more important for BC than for trace gases, which questions the general transferability of the results from trace gas studies to BC. Other studies provided good agreement of model simulations with observations for an emission release between the surface and the PBL height as well as a fixed height of 1.2 km (Wang et al., 2006; Matichuk et al., 2007). While Jian and Fu (2014) found a large sensitivity of BC concentrations on the emission heights, Colarco (2004) demonstrated that the differences between a near-surface emission release and a release between 2 and 6 km are small for convective atmospheric conditions. Chen et al. (2009) used the GEOS-CHEM model with GFED2 emissions to simulate the smoke transport from North American forest fires. The authors found the best overall model performance for a scenario of 40 % emissions injected into PBL and 60 % emissions injected into the FT. For a study by Stein et al. (2009), in one case PBL injections performed best, whereas in another case plume heights up to 3 km were necessary to reproduce observations. Gonzi et al. (2015) applied a modified version of the 1-D plume model by Freitas et al. (2007), MODIS FRP and fire size to simulate global CO concentrations in GEOS-Chem for the year 2006. The authors compared modeling results to Measurement of Pollution in the Troposphere (MOPITT) satellite data, but it turned out that the particular emission height impact on the overall bias was not quantifiable. Overall, modeling as well as observational studies (e.g., Diner et al., 2008; Val Martin et al., 2010; Ichoku et al., 2012) indicate that wildfire plume heights are highly variable on the global scale. While Freitas et al. (2007), Rio et al. (2010) and others demonstrated a reasonable performance for their specific plume height parametrizations in particular case studies, other authors including Val Martin et al. (2012) and Goodrick et al. (2012) presented results that showed a poor to moderate performance of all these models on the global scale.

In summary, our knowledge about both, an appropriate implementation of emission heights in global climate models as well as the impact of the emission heights on aerosol long-range transport, atmospheric radiative transfer and other climate variables is very limited. In the second chapter of this thesis, we presented globally simulated plume height patterns. Through a comparison of simulated plume heights to observations from the MPHP data set, we evaluated the performance of different plume height implementations. The best agreement of model results to observations was found for a modified version of the Sofiev et al. (2012) plume height parametrization (modeled global mean plume heights 1411 ± 646 m, observed mean global plume heights 1382 ± 702 m). Only 5.2 ± 1.0 % of all

daytime plumes were injecting emissions into the FT. On average, plume heights simulated by the semi-empirical parametrization are 1.1–2.0 km lower than prescribed standard plume heights in ECHAM6-HAM2. Based on the simulations introduced in chapter 2 and the additional extreme scenarios (pure surface and free-tropospheric injections) presented in this chapter, we analyze atmospheric BC concentrations, BC deposition rates and atmospheric radiative transfer for all simulations to address the following research questions:

- To what extent do wildfire emission heights impact atmospheric aerosol concentrations and aerosol–radiation interaction?
- How important is the vertical distribution of the released emissions?
- Does the diurnal cycle of fire intensity and emission release enhance, dampen or change the sign of the averaged climate response?
- How might a future increase in fire intensity and emissions influence plume heights and radiation?
- What degree of complexity in plume height parametrization is required to capture the emission height impact on aerosol long-range transport and atmospheric radiative transfer in global climate models?

A comprehensive comparison of modeled AOT (also referred to as Aerosol Optical Depth, AOD) to observational data sets from Marine Aerosol Network (MAN), AERONET, MODIS and CALIOP gives us an independent constraint on an adequate choice of plume height parametrizations for climate modeling applications.

The next section introduces our model setup, the different plume height implementations and the observational data sets used for model evaluation. In the "Comparison of model results to observations" section, the impact of the wildfire emission heights on BC concentrations, deposition rates and radiation is analyzed. Furthermore, we present regional time series and statistical analysis on the model performance. The conclusions section summarizes our results and provides suggestions for future implementations of plume height parametrizations in climate and Earth system models based on our findings.

3.2 Methodology

3.2.1 ECHAM6-HAM2 model description

The aerosol–climate modeling system ECHAM6-HAM2 is an extension of ECHAM6, the atmospheric component of the MPI-ESM (Stevens et al., 2013). ECHAM6-HAM2 predicts the evolution of micro-physically interacting aerosol populations, their size distribution and composition (Stier et al., 2005; Zhang et al., 2012a). For all our simulations, we use model version ECHAM6.1.0-HAM2.2. We apply a spatial grid of approximately $1.875° \times 1.875°$ (T63) and a temporal resolution of 600 s. The 47 vertical layers range from the surface to 0.01 hPa. To allow for appropriate comparisons of the wildfire RF, the model is nudged against observational data every 6 h by relaxation of the prognostic variables to ERA-Interim reanalysis fields (Dee et al., 2011). The aerosol module HAM2

employs a superposition of seven lognormal distributions which describe the nucleation, Aitken, accumulation and coarse modes. Besides dust, sea salt and sulfur emissions from natural and anthropogenic sources, the model also simulates the emission and transport of carbonaceous matter from anthropogenic sources and wildfires.

Wildfire emissions are represented by three species in the ECHAM6-HAM2 model: BC, OC and SO_2. For details on the implementation of sedimentation, wet and dry deposition, thermodynamics and aerosol micro-physics parametrization, see Stier et al. (2005). A detailed assessment of the processes which drive the evolution of aerosol mass and number concentrations is described in Schutgens and Stier (2014). Calculations of aerosol optical properties are based on Mie theory for 24 solar spectral bands and provide single scattering albedo, extinction cross section and asymmetry factors. These parameters in turn serve as input for radiation calculations by the ECHAM6 radiation scheme (Giorgetta et al., 2013; Stevens et al., 2013). Aerosol–cloud interactions are represented by a two-moment cloud micro-physics scheme that is coupled to the aerosol micro-physics (Lohmann et al., 2007). Overall, we carry out nine ECHAM6-HAM2 simulations with different emission height implementations for 8 years (2004–2011) which will be described in the next two sections. The year 2004 is used for the spin-up of the model and therefore excluded from our analysis.

3.2.2 Emission data sets

In the standard release of ECHAM6-HAM2, AEROCOM phase 2 wildfire emissions (Dentener et al., 2006) are implemented. These emissions are based on GFEDv2 data (van der Werf et al., 2006) multi-year monthly means of the years 1997–2008. GFEDv2 emissions are derived from burnt area observations and do not provide any information on wildfire intensity. As fire intensity is a key input parameter required for plume height parametrizations, the AEROCOM emission data set within the standard ECHAM6-HAM2 model does not represent an appropriate framework to study wildfire emission heights. In contrast to GFED, GFASv1.1 (Kaiser et al., 2012) uses FRP retrieved from MODIS satellite observations to estimate fire emissions from the year 2000 to present. GFAS applies land-cover-specific emission factors to calculate combustion rates and fills observational gaps by use of a Kalman filter. With consistent aerosol emission and fire intensity information, GFASv1.1 provides an appropriate input data set for our simulations.

Kaiser et al. (2012) found that GFAS emissions implemented in the global circulation model ECMWF are only able to reproduce AOT observations in a reasonable way, if global GFAS wildfire emissions are multiplied by a global factor of 3.4. This zero-order approximation also provided reasonable global modeling results in studies by Huijnen et al. (2012) and von Hardenberg et al. (2012) using the global MACC atmospheric composition forecasting system as well as ECHAM5-HAM1. Basically, the underestimation of AOT in GFAS and other bottom-up inventories could have various reasons including an underestimation of emission fluxes (e.g., due to underestimation of wildfire emission factors or burned area and FRP) as well as shortcomings in the representation of aerosol microphysics in the model (impacting aging and removal rates). It would be highly desirable to investigate the reasons for the required factor of 3.4 in more detail in a future study.

We apply the GFASv1.1 emission data set for eight out of nine simulations, but we also run one simulation with the standard AEROCOM wildfire emissions to provide a reference which is comparable to other ECHAM6-HAM2 studies. As the global annual emission fluxes of GFAS and AEROCOM show mean differences of less than 9.2 % for BC and 4.4 % for OC, we decided to apply the 3.4 factor not only to GFAS but also to AEROCOM wildfire emissions. For both, AEROCOM as well as GFAS simulations, wildfire emissions are represented by the emission species BC, OC and SO_2.

In addition, we run one "NO-WILDFIRES" scenario for which wildfire emissions are completely switched off to calculate the overall wildfire emission impact on radiation.

3.2.3 Emission height parametrizations

Table 3.1 provides a summary of all plume height parametrizations used in this study. Based on the large range of emission height implementations in the literature, we apply first the most extreme and unrealistic scenarios for our sensitivity study: on the one hand the experiment "SURFACE" simulates a wildfire emission release into the lowest and second lowest model layer (approximately 30–150 m above the surface). Thus, this simulation provides the lower limit of the emission height radiative impact due to fast removal of the aerosols close to the surface. Wildfire emissions in simulation SURFACE were chosen to be distributed into the two lowest model layers instead of the surface layer only, because in preliminary test runs prior to this study, very intense wildfire emission releases concentrated at one specific model layer resulted in model instabilities, presumably due to radiative imbalance. On the other hand a simulation of purely free-tropospheric emission release (FT) serves as an unrealistic upper constraint of the emission height climate impact.

In the standard version of ECHAM6-HAM2.2, plume heights for all wildfires are prescribed as the PBL height plus two model layers, see also section 2.2.1, equation 2.1 If the PBL height exceeds 4 km, H_p is set to PBL height. We use this implementation as a reference simulation "HAM2.2-GFAS". For a more appropriate representation of wildfire emission heights in ECHAM6-HAM2, we implemented the semi-empirical plume height parametrization introduced by Sofiev et al. (2012) (named "SP"). In contrast to the standard emission heights in ECHAM6-HAM2, the SP takes into account the total FRP of a fire P_f as well as atmospheric stability (Brunt–Väisälä frequency of the atmosphere N) and PBL height H_PBL to predict fire emission heights:

$$H_\mathrm{p} = \alpha H_\mathrm{PBL} + \beta \left(\frac{P_\mathrm{f}}{P_\mathrm{f0}} \right)^{\gamma} \exp\left(-\delta N^2 / N_0^2 \right). \tag{3.1}$$

For more details on the SP, a description of the normalizing constants N_0 and P_f0 as well as the tuning parameters α, β, γ and δ and all modifications we applied (e.g., introduction of a diurnal cycle in FRP), see chapter 2 and Sofiev et al. (2012). Overall we carry out five simulations with different implementations of the SP: the original and most simple one-step model as described in Sofiev et al. (2012) called "SOFIEV-ORIGINAL", one simulation with additional application of a diurnal cycle in fire emissions and FRP called "SOFIEV-DCYCLE" and one simulation which applies a diurnal cycle as well as a tuning of high plumes "SOFIEV-MODIFIED". Simulation SOFIEV-MODIFIED represents the

Table 3.1: Set-up of ECHAM6-HAM2 simulations for 2005–2011 based on various plume height parametrizations. All simulations are nudged towards observations every six hours. In addition to the listed simulations, a *NO-WILDFIRES* scenario represents a simulation without any wildfire emissions. The diurnal cycle refers to FRP. See text for a more detailed description of the emission height implementations and emission inventories.

Simulation Name	**Plume Height Parametrization**	**Diurnal Cycle**	**Emission Inventory**	**Emission Distribution**
HAM2.2-GFAS	PBL Height+ 2 model layers	NO	GFAS	25 % into FT, 75 % into PBL
SOFIEV-ORIGINAL	SOFIEV (Original)	NO	GFAS	const. mass mixing ratio top – bottom
SOFIEV-DCYCLE	SOFIEV (Original)	YES	GFAS	const. mass mixing ratio top – bottom
SOFIEV-MODIFIED	SOFIEV (Modified)	YES	GFAS	const. mass mixing ratio top – bottom
SOFIEV-TOP-INJECTION	SOFIEV (Original)	YES	GFAS	50 % into top layer, 50 % top – bottom
SURFACE	2 lowest model layers (30–150 m)	NO	GFAS	100 % into lowest and 2nd lowest layer
FT	PBL Height to Tropopause	NO	GFAS	100 % into FT, const. mass mix. ratio
SOFIEV-2X-EMISSIONS-FRP	SOFIEV (Original, 2xFRP)	NO	GFAS	const. mass mixing ratio top – bottom
HAM2.2-AEROCOM	PBL Height+ 2 model layers	NO	AEROCOM	25 % into FT, 75 % into PBL

plume height parametrization which provides the best agreement to global plume height observations (see chapter 2). A hypothetical future scenario with a doubling in FRP and emissions, "SOFIEV-2X-EMISSIONS-FRP", enables a comparison of the impact of changes in emission fluxes and emission heights. We assume the BC/OC/SO_2 emission ratios for simulation SOFIEV-2X-EMISSIONS-FRP to be constant and apply BC/OC/SO_2 ratios provided by GFASv1.1. The last simulation "SOFIEV-TOP-INJECTION" is run to test the influence of the vertical emission distribution.

3.2.4 Vertical distribution of wildfire emissions

Besides the plume heights which describe the maximum level of emission injection above the surface, one has to make assumptions on the vertical distribution of the emissions from the surface to the plume height. For all SOFIEV simulations, we distribute emissions from the surface to the first level below the top of the plume with a constant mass mixing ratio. Simulation FT also applies a constant mass mixing ratio from the PBL height to the first level below the tropopause. In the simulation SURFACE, all wildfire emissions are

injected into the first two model layers approximately 30–150 m above surface. HAM2.2-AEROCOM and HAM2.2-GFAS use the vertical emission distribution prescribed in the standard HAM2.2 model with a fraction of 25 % of the emissions to be injected into the FT (in the two levels just above the PBL). The remaining 75 % of the emissions are distributed from the surface to the PBL height with constant mass mixing ratio.

Vertical emission distributions with constant mass mixing ratios have been used in most former global aerosol modeling studies even in case of more advanced plume models, e.g., Freitas et al. (2007). Our knowledge about the global variability of vertical emission distributions is even more limited than our knowledge about the plume heights. However, Luderer et al. (2006) and Fromm et al. (2010) showed in modeling, as well as observational case studies, that rare but extraordinarily high injections might emit a large fraction of the emissions into the upper part of the plumes. To account for this, we perform one sensitivity study, in which we emit 50 % of the total emissions into the uppermost layer of the plume and we distribute the remaining 50 % uniformly (constant mass mixing ratio) into the model layers below (SOFIEV-TOP-INJECTION).

3.2.5 Observational data sets for model evaluation

For evaluation of the ECHAM6-HAM2 model performance, vertically resolved and integrated AOT values are compared to observations from AERONET, MODIS, MAN and CALIOP. The AERONET program (Holben et al., 1998) is a ground network of sun photometers that provides long-term continuous AOT measurements based on the attenuation of direct solar radiation. These AOT measurements are estimated to have errors of ≈ 0.015 (Eck et al., 1999; Schmid et al., 1999) and are considered some of the most accurate aerosol observations we have. In this study, we use AERONET AOT which was averaged over 6 h, every 6 h.

The MAN is an integrated component of AERONET and includes data from ship cruises since the end of 2004 (Smirnov et al., 2011). It is based on hand held Microtops II sun photometers with five spectral channels ranging from 320 to 1020 nm providing data for spectral AOT. The MAN data set has limited spatial and temporal coverage due to the limited number of ship cruises which collected data (about 1700 individual days of measurements between November 2006 and March 2010).

In addition to AERONET data, spectral radiance measurements from the two MODIS sensors aboard the Aqua and Terra satellites are used to monitor AOT with a wide spatial coverage. MODIS AOT values are calculated by retrieval algorithms based on lookup tables for different particles which depend on scattering geometries (Tanre et al., 1997). Error estimations of MODIS AOT retrievals have been investigated by comparison with ground-based AERONET (e.g., Remer et al., 2005; Bréon et al., 2011) and MAN observations (e.g., Adames et al., 2011; Smirnov et al., 2011). Here we use the Naval Research Laboratory (NRL) L3 (Hyer et al., 2011; Shi et al., 2011) data that are derived from MODIS L2 observations through additional quality checks and empirical correction formulae. Both, the Aqua as well as the Terra NRL L3 data, are 1° by 1° aggregates, available every 6 h. MODIS observations do provide a far wider spatial coverage than AERONET, but uncertainties are significantly larger. For the quantitative analysis of the plume height

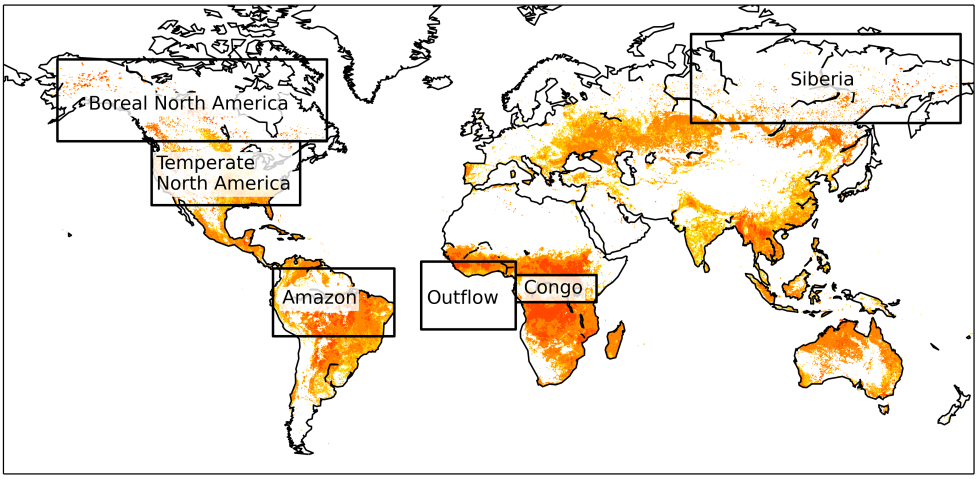

Figure 3.1: Region specification used for comparison of modeled AOT to observations. Color shading represents mean annual assimilated FRP values of GFASv1.1 for 2005–2011. Yellow colors indicate low FRP values, dark red colors indicate high FRP values.

parametrization, we restrict our considerations to the following six regions: boreal North America, temperate North America, Siberia, the Amazon area and neighboring regions, Congo and the African outflow to the tropical Atlantic (Fig. 3.1).

Vertically resolved information of AOT is provided by the CALIOP on board the CALIPSO satellite which was launched in June 2006 to acquire global aerosol profile data between 82° N and 82° S (Winker et al., 2010). CALIOP provides backscatter profiles at a vertical resolution of 30 m (below 8.2 km) as well as 60 m (between 8.2 and 20.2 km). Vertical aerosol extinction profiles are calculated at 1064 and 532 nm (Winker et al., 2013). CALIOP vertical AOT profiles have a good global coverage, but the uncertainties in individual AOT profiles are known to be large due to uncertainties in lidar ratios (e.g., Campbell et al., 2013; Winker et al., 2013). There is a tendency of CALIOP to underestimate low AOT values and the lowest 1.4 km are not reasonably captured. The gridded CALIOP level 3 data have been shown to provide more accurate AOT values than level 2 data because of an improved retrieval algorithm for the lowest 1.4 km (Kacenelenbogen et al., 2011; Redemann et al., 2012). Therefore, in this study, we apply multi-annual monthly means of level 3 data for 2006–2011 and restrict our analysis to relative vertical AOT profiles. For our analysis, we use only complete CALIOP vertical profiles without missing individual layers. Absolute AOT values are vertically averaged to 0.5 or 1.0 km layers for our comparison to ECHAM6-HAM2 model simulations.

In contrast to the spatially and temporally collocated MODIS, AERONET and MAN data of 6 hourly resolution, which we use for the comparison of total AOT to ECHAM6-HAM2 simulations, CALIOP level 3 data are only available in monthly temporal and $2° \times 5°$ (latitude $\times$ longitude) horizontal resolution. Therefore, the introduced errors in the CALIOP model–observations comparison are a priori larger for the CALIOP data then for MODIS, AERONET and MAN data. On the other hand CALIOP is the only data set which provides vertically resolved AOT profiles of global coverage.

3.3 Impact on BC burdens, concentrations and deposition rates

Differences in emission height parametrizations can be expected to cause differences in the vertical and horizontal transport of the wildfire emissions. To quantify these changes in global aerosol transport, we assess regional and global changes in BC burdens, vertical concentration profiles and deposition rates. We analyze seven years of model simulations (2005–2011) for the nine emission height scenarios provided in Table 3.1.

3.3.1 BC burdens

Global mean values of the atmospheric BC and OC aerosol burdens for all individual experiments are presented in Table 2.4. As the patterns of changes in OC concentrations and deposition rates are very similar to the changes in BC, we limit our detailed analysis to BC. Changes in SO_2 are not discussed in this chapter as SO_2 emissions from wildfires contribute only about 5 % to the overall SO_2 emissions. Table 2.4 also reports the range of plume heights simulated in the individual experiments. Global plume height patterns have been discussed in detail in chapter 2. All global mean values provided in Table 2.4 are complemented by more detailed and region-specific discussions within the next three sections. Note that all uncertainty estimates in Table 2.4 (except for the plume heights) represent 1 SD of monthly global means for 2005–2011.

Figure 3.2 illustrates the global relative changes in BC burden for the individual experiments compared to the standard ECHAM6-HAM2 setup (simulation HAM2.2-GFAS). For the various implementations of the Sofiev plume height parametrization (SOFIEV-ORIGINAL, SOFIEV-DCYCLE, SOFIEV-MODIFIED, SOFIEV-TOP-INJECTION; see Fig. 3.2a–d), the global patterns of changes in BC burden are very similar in the tropics and subtropics. While an increase in BC burden is observable close to the source regions, the implementation of the plume height parametrization introduces a reduction in BC burden far from the source regions. The simulated changes in BC burden can be attributed to a decreased aerosol long-range transport. The application of a diurnal cycle (SOFIEV-DCYCLE) which increases the height of daytime plumes, and a more realistic representation of deep emission injections (SOFIEV-MODIFIED), introduce only marginal changes in BC burden. In the TOP-INJECTION scenario, which injects 50 % of the emissions into the highest emission layer, the sign of the relative changes in BC burden compared to simulation HAM2.2-GFAS changes in boreal regions. The higher burdens can be attributed to the importance of strong boreal forest fire events which emit significant fractions of the emissions into the FT. Although the majority of emission injections in the SOFIEV simulations are injecting below the HAM2.2-GFAS emission heights, a small fraction of strong emission events simulated by the Sofiev parametrizations exceeds the HAM2.2-GFAS maximum emission heights of PBL height + two model layers (see chapter 2). The comparison of simulations SOFIEV-ORIGINAL, SOFIEV-DCYCLE and SOFIEV-MODIFIED shows that the changes in BC burden introduced by the application of a diurnal cycle and more realistic deep plumes are rather small on the global scale.

Table 3.2: Global mean values (2005–2011) describing aerosol atmospheric transport and radiation for various parametrizations of plume heights in ECHAM6-HAM2.2. The *NO-WILDFIRES* simulation serves as reference for calculation of total sky TOA RF in all simulations. Simulation *HAM2.2-AEROCOM* is based on AEROCOM emissions, for all other simulations we use GFASv1.1 emissions. The Asterisk (*) in the last column indicates that plume height values represent 10^{th} to 90^{th} percentiles. For a detailed plume height and emission inventory setup of all scenarios, see Table 3.1. Uncertainties represent one standard deviation of monthly means for 2005–2011.

Simulation Name	**BC Burden [Tg]**	**OC Burden [Tg]**	**BC Wet Deposition [Tg yr^{-1}]**	**BC Dry Deposition [Tg yr^{-1}]**	**BC Sedimentation [Tg yr^{-1}]**	**BC Lifetime [days]**	**Surface RF [Wm^{-2}]**	**TOA RF [Wm^{-2}]**	**Plume Heights* [km]**
HAM2.2-GFAS	0.34±0.02	3.03±0.20	13.60±0.69	1.06±0.04	0.032±0.002	8.50±0.23	-1.75±0.18	-0.24±0.05	1.8–3.9
HAM2.2-AEROCOM	0.36±0.01	3.17±0.08	14.44±0.02	1.07±0.02	0.035±0.001	8.50±0.02	-1.82±0.09	-0.25±0.06	1.8–3.9
FT	1.26±0.11	13.01±1.15	13.60±0.55	0.89±0.02	0.035±0.001	31.58±2.34	-7.37±1.16	+0.66±0.24	10.9–15.8
SURFACE	0.32±0.02	2.76±0.16	13.33±0.66	1.35±0.07	0.038±0.002	7.82±0.17	-1.51±0.15	-0.16±0.06	0.1–0.2
SOFIEV-ORIGINAL	0.33±0.02	2.87±0.18	13.55±0.68	1.13±0.05	0.033±0.002	8.08±0.19	-1.62±0.17	-0.20±0.05	0.8–1.9
SOFIEV-DCYCLE	0.33±0.02	2.89±0.18	13.56±0.69	1.11±0.04	0.033±0.002	8.15±0.19	-1.63±0.17	-0.20±0.06	1.0–2.2
SOFIEV-MODIFIED	0.33±0.02	2.90±0.18	13.56±0.69	1.11±0.04	0.033±0.002	8.17±0.20	-1.63±0.16	-0.20±0.07	1.0–2.3
SOFIEV-TOP_INJ	0.33±0.02	2.95±0.19	13.59±0.69	1.07±0.04	0.032±0.002	8.28±0.21	-1.67±0.16	-0.21±0.06	1.0–2.2
SOFIEV-2X-EMISSIONS-FRP	0.57±0.04	5.40±0.41	21.46±1.38	1.46±0.07	0.058±0.006	9.08±0.29	-3.28±0.34	-0.36±0.11	0.9–2.2

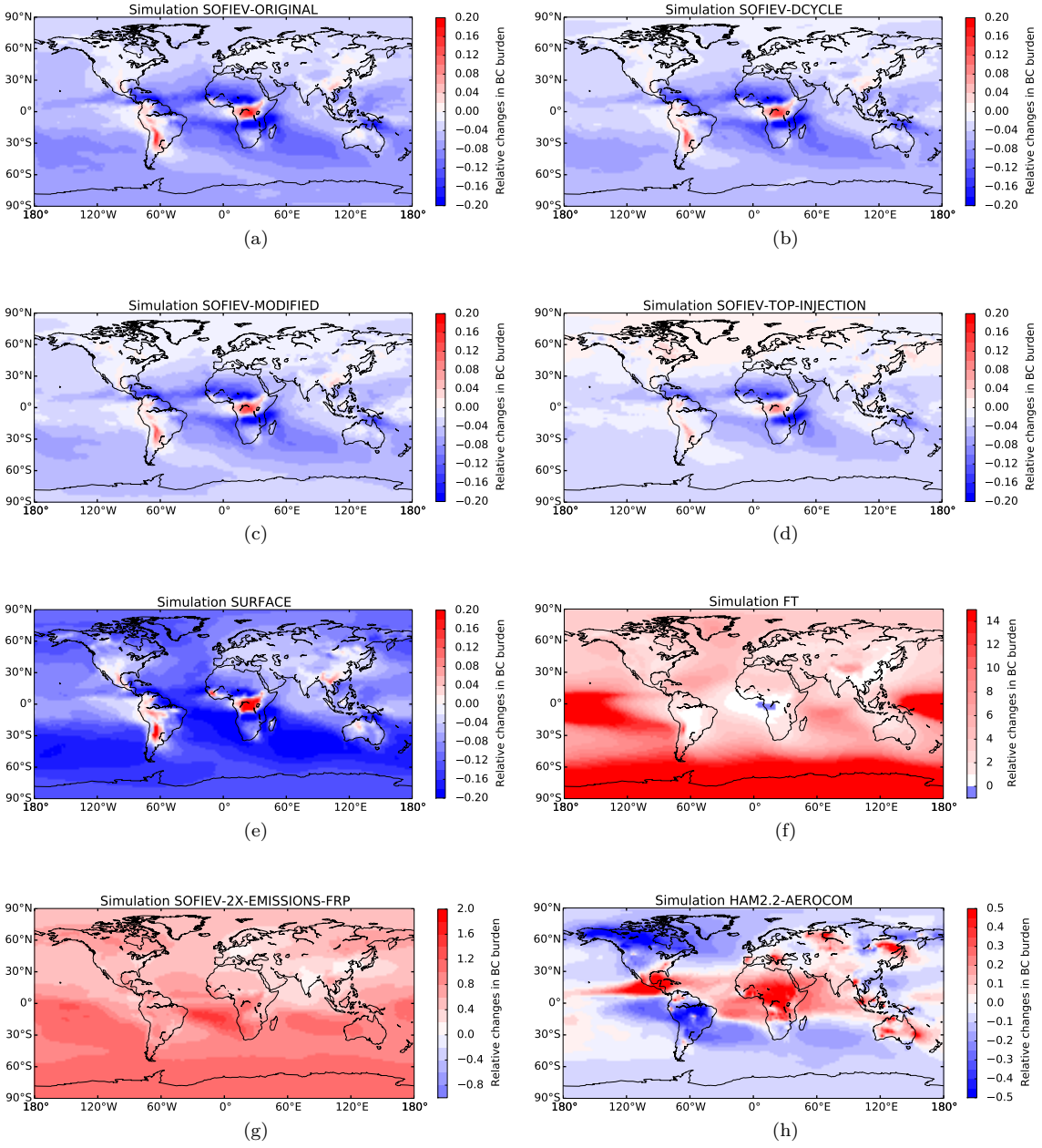

Figure 3.2: Mean relative changes in BC burden introduced by various implementations of fire emission heights. All relative changes refer to the standard implementation of prescribed emission heights combined with GFASv1.1 emissions (simulation HAM2.2-GFAS). Simulations SOFIEV-ORIGINAL **(a)**, SOFIEV-DCYCLE **(b)**, SOFIEV-MODIFIED **(c)** and SOFIEV-TOP-INJECTION **(d)** show different versions of the Sofiev plume height parametrization. Simulation SURFACE **(e)** represents near surface emissions, simulation FT **(f)** is based on purely free-tropospheric emissions. SOFIEV-2X-EMISSIONS-FRP **(g)** assumes a doubling in emissions and FRP. HAM2.2-AEROCOM **(h)** illustrates the influence of changes in the emission inventory. For a description of settings for simulations **(a)** to **(h)**, see Table 3.1.

Simulation SURFACE, the extreme scenario of pure near-surface emission injections, provides an estimate of the lower limit of the global BC burden (Fig. 3.2e). For the near-surface emission injections, residence times and therefore also BC burdens are increased in the vicinity of the sources, while long-range transport is generally reduced. The negative relative changes in BC burden are more pronounced in the Southern Hemisphere and range from 10 to 25 %.

Global mean relative changes in BC burden introduced by the replacement of prescribed emission heights in HAM2.2 by the implementation of various versions of the Sofiev plume height parametrization range between −2.6 and −4.8 % for BC and −2.7 and −5.5 % for OC. For the SURFACE scenario, global BC and OC burdens are reduced by −7.9 % and −8.9 %, respectively. These changes are remarkably small due to the fact that median global plume heights between these simulations range from about 0.15 km for the SURFACE simulation to 2.7 km for the HAM2.2-GFAS prescribed plume heights (see chapter 2). Consequently, these results indicate that the vertical mixing in ECHAM6-HAM2 acts very efficiently in the lower troposphere.

The extreme and unrealistic scenario of purely free-tropospheric injections shows an increase in BC burden over Antarctica by more than 20 times (see Fig. 3.2f). BC burdens in simulation FT are dominated by long-range transport rather than the emission sources. Because of the proportionately higher fraction of wildfire emission to the overall BC burden in the Southern Hemisphere, the relative changes in BC burden in these regions are more sensitive to plume height changes. The scenario of a doubling in FRP and fire emissions (Fig. 3.2g) entails an increase in atmospheric BC burden which largely exceeds the changes of the other simulations except the unrealistic FT scenario. In scenario SOFIEV-2X-EMISSIONS-FRP, which assumes a doubling in FRP and wildfire emissions corresponding to an overall increase in total BC emissions by 56.7 %, the global BC burden is non-linearly enhanced by 38.7 % compared to simulation SOFIEV-DCYCLE. This dampening of the increase in atmospheric BC concentrations for increased emissions can be attributed to the interaction of multiple aerosol micro-physical and atmospheric effects. These include but are not limited to non-linear particle formation, coagulation and deposition, micro-physical cloud processes and atmospheric feedback via changes in vertical temperature profiles due to changes in aerosol concentrations and radiation. However, in the framework of this study, it is impossible to disentangle the contribution of particular processes to the overall non-linear source–receptor relationship. A comparable magnitude in damping of the atmospheric response to an increased emission release has been found by Zhang et al. (2014) within a WRF-CHEM modeling study. Note that the differences in plume heights for a doubling in FRP and emissions do not exceed 100–500 m on average for 95 % of all plumes (see chapter 2).

Although the global mean differences in emission fluxes between AEROCOM and GFAS are only 9.2 %, the regional differences are considerably larger. For boreal regions (60–80° N), GFAS BC emission fluxes are roughly 2 times the AEROCOM emission fluxes. In the temperate regions (20–60° N and 20–60° S) GFAS is about 18.8 % higher than AEROCOM. In the tropical source regions (20° S to 20° N), which dominate the global burden, AEROCOM BC emission fluxes exceed the GFAS emission fluxes by 17.9 %. Figure 3.2h shows large regional differences in atmospheric burden between the HAM2.2-GFAS and the

HAM2.2-AEROCOM simulations applying the same plume height parametrization. These differences in BC burdens largely reflect the spatial differences in the emission inventories. Nevertheless, the mean total global BC burdens of HAM2.2-AEROCOM (0.36 ± 0.01 Tg) and HAM2.2-GFAS (0.34 ± 0.02 Tg) are very similar as a result of similar mean global emission fluxes.

The global mean BC lifetime of realistic plume height implementations ranges between 8.1 ± 0.1 days for the SOFIEV-ORIGINAL simulation and 8.5 ± 0.2 days for the prescribed standard emission heights in HAM2.2-GFAS (see Table 2.4). For similar daytime emission heights, a doubling in wildfire emissions (simulation SOFIEV-DCYCLE vs. SOFIEV-2X-EMISSIONS-FRP) enhances the mean BC lifetime by 22.3 h. An increase in plume heights by 1.7–3.7 km for simulation HAM2.2-GFAS compared to simulation SURFACE introduces an increase in BC lifetime by about 16.3 h. Due to the GFAS emission flux factor of 3.4 applied in this study, these lifetimes are substantially larger than mean BC lifetimes of 5.9 days in ECHAM6-HAM2 shown by Zhang et al. (2012a). The lifetimes in our study, however, are still within the range of the AEROCOM models for which mean lifetimes of 7.1 days with a 33 % SD were found (Textor et al., 2006).

3.3.2 Vertical BC concentration profiles

Figure 3.3 presents vertical cross sections of relative changes in BC concentrations as zonal means for 2005–2011. Compared to the HAM2.2-GFAS simulation with a prescribed emission injection of 25 % into the FT, the on average much lower Sofiev emission heights lead to increased BC concentrations near the surface and decreased BC concentrations in the FT. Differences in BC concentrations between the various versions of the Sofiev plume height parametrization are largely smaller than 5 % (Fig. 3.3a–d). However, for the SOFIEV-TOP-INJECTION scenario, the near-surface concentrations are substantially lower than for the other SOFIEV simulations (see Fig. 3.3d). In the tropics, a slight increase in BC concentrations is observable between 500 and 300 hPa for all SOFIEV simulations. This enhancement in tropical free-tropospheric BC concentrations cannot be directly attributed to differences in emission heights which are smaller in all SOFIEV simulations compared to the HAM2.2-GFAS standard emission heights. Moreover, Fig. 3.2a–d show a substantial increase in BC burden in equatorial Africa for the Sofiev simulations. As the regions of increased burden coincide with the strongest tropical convective zones, we assume that deep convection is the major process which determines the free-tropospheric BC concentrations, not the emission heights.

For simulation SURFACE, a decrease in mean BC concentrations up to 25 % in the Southern Hemispheric FT is found, but the sensitivity of stratospheric BC concentrations to emission heights is very limited (relative changes < 5 %). The other extreme scenario (simulation FT) shows an upper tropospheric and lower stratospheric increase in BC concentrations by a factor of 10–100 which substantially impacts the radiative transfer (see Sect. 3.5). For the SOFIEV-2X-EMISSIONS-FRP scenario, the largest relative increase in BC concentrations is observable in the Southern Hemispheric upper troposphere and lower stratosphere. Simulation HAM2.2-AEROCOM (see Fig. 3.3h) reflects the enhanced tropical wildfire emission fluxes in the AEROCOM emission data set compared to GFAS.

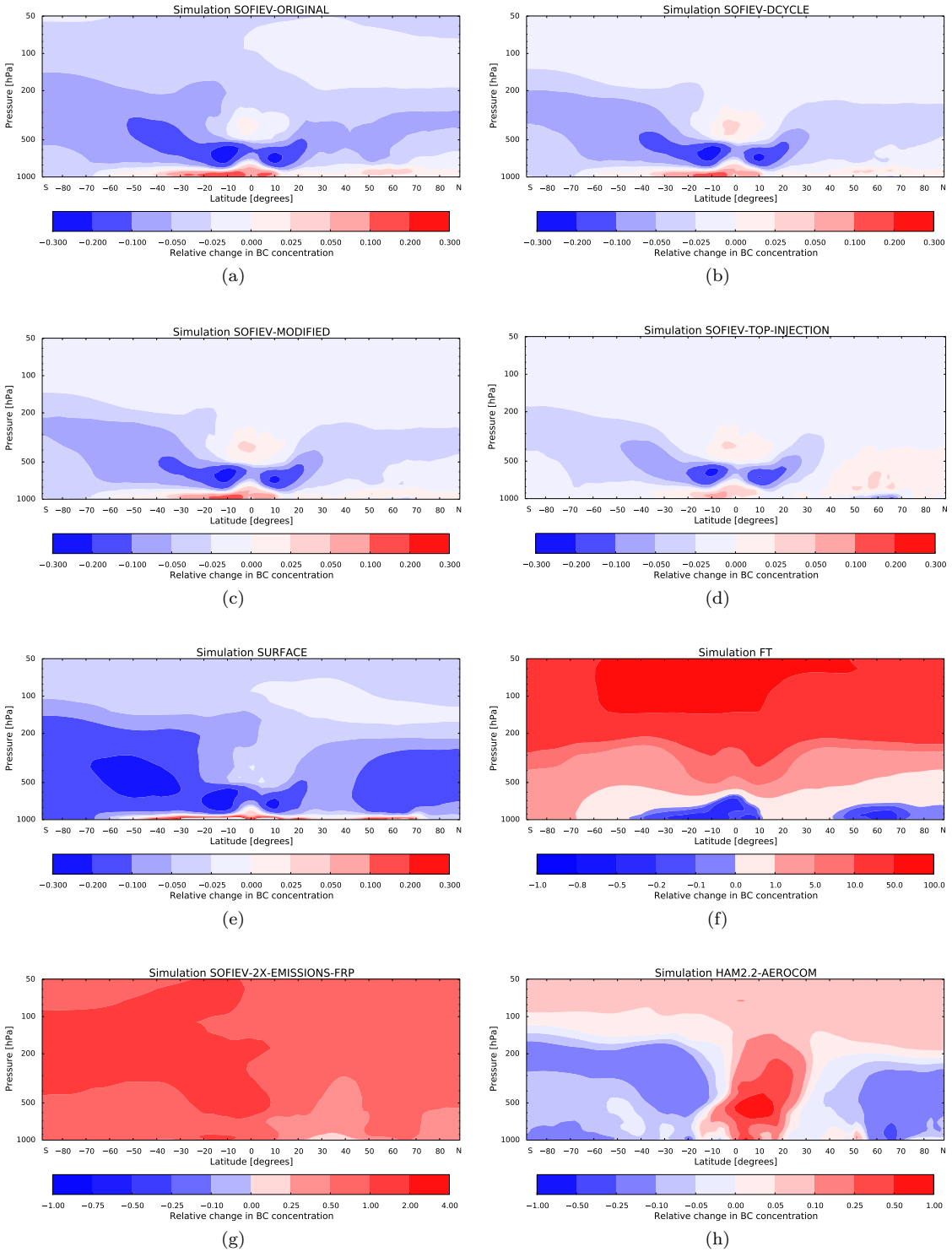

Figure 3.3: Mean relative changes in zonal mean BC concentrations for 2005–2011. All relative changes refer to the standard implementation of prescribed emission heights combined with GFASv1.1 emissions (simulation HAM2.2-GFAS). A more detailed description of the simulation set-ups is provided in Table 3.1.

As a result of the tropical convective transport, BC concentrations in the lower stratosphere are increased by 5–20 % all over the globe in the HAM2.2-AEROCOM simulation. On the other hand, the extra-tropical tropospheric BC concentrations are decreased by 5–25 %. Overall Fig. 3.3 demonstrates that upper tropospheric and lower stratospheric BC concentrations are not very sensitive to the emission heights if realistic emission height scenarios are applied.

3.3.3 Total deposition rates

Global mean values of wet deposition rates, dry deposition rates and sedimentation rates for BC are provided in Table 3.2. A potential climate impact of BC emissions is related to the deposition of BC on snow and ice which substantially reduces the surface albedo (e.g., Dumont et al., 2014). In this context, the question arises how strongly deposition rates in the Arctic and Antarctic depend on emission heights. Figure 3.4 presents the relative changes in total deposition rates for our various plume height implementations. Simulation SOFIEV-ORIGINAL reflects an increase in deposition rates in the vicinity of the major source regions due to lower emission heights. In contrast, the reduced remote deposition rates can be attributed to a decreased atmospheric long-range transport. Changes introduced by a consideration of the diurnal cycle in fire emissions (SOFIEV-DCYCLE) and a more accurate representation of high plumes (SOFIEV-MODIFIED) only marginally influence the deposition rates on the global scale. Over Antarctica, total deposition rates are decreased by 20–25 % for the SURFACE emission release compared to the HAM2.2 standard implementation. Over the glaciated areas of Greenland and the northern polar ice sheet, the reduction ranges between 10 and 20 %. However, although these changes are substantial, the known model biases in aerosol long-range transport, which have been found for ECHAM5-HAM1 by Bourgeois and Bey (2011) and von Hardenberg et al. (2012), may still persist. A global doubling of emissions and fire intensity results in a Southern Hemispheric increase in regional deposition rates of 60–140 % (Fig. 3.4g). In the Northern Hemisphere this increase is significantly smaller, because the BC release in mid-latitudes is largely dominated by anthropogenic emissions, not by wildfires.

3.4 Comparison of model results to observations

Our temporal analysis for the six regions specified in Fig. 3.1 for 2006–2008 is restricted to four simulations: a zero fire emissions scenario (NO-WILDFIRES), the HAM2.2-AEROCOM and the HAM2.2-GFAS simulations, both applying HAM2.2 emissions heights and the SOFIEV-MODIFIED simulation which is most appropriately representing the global spectrum of plume heights. For the sake of clarity, the other SOFIEV simulations, which have been shown to only marginally influence parameters such as BC burden and concentrations, are not included. Likewise, the scenarios SOFIEV-2X-EMISSIONS-FRP, SURFACE and FT are excluded from this analysis as these simulations do not represent realistic emission heights and emission inventories. Thus, these simulations cannot be expected to match observations. The NO-WILDFIRES scenario is used to identify regions and time periods in which wildfires significantly contribute to the overall model bias.

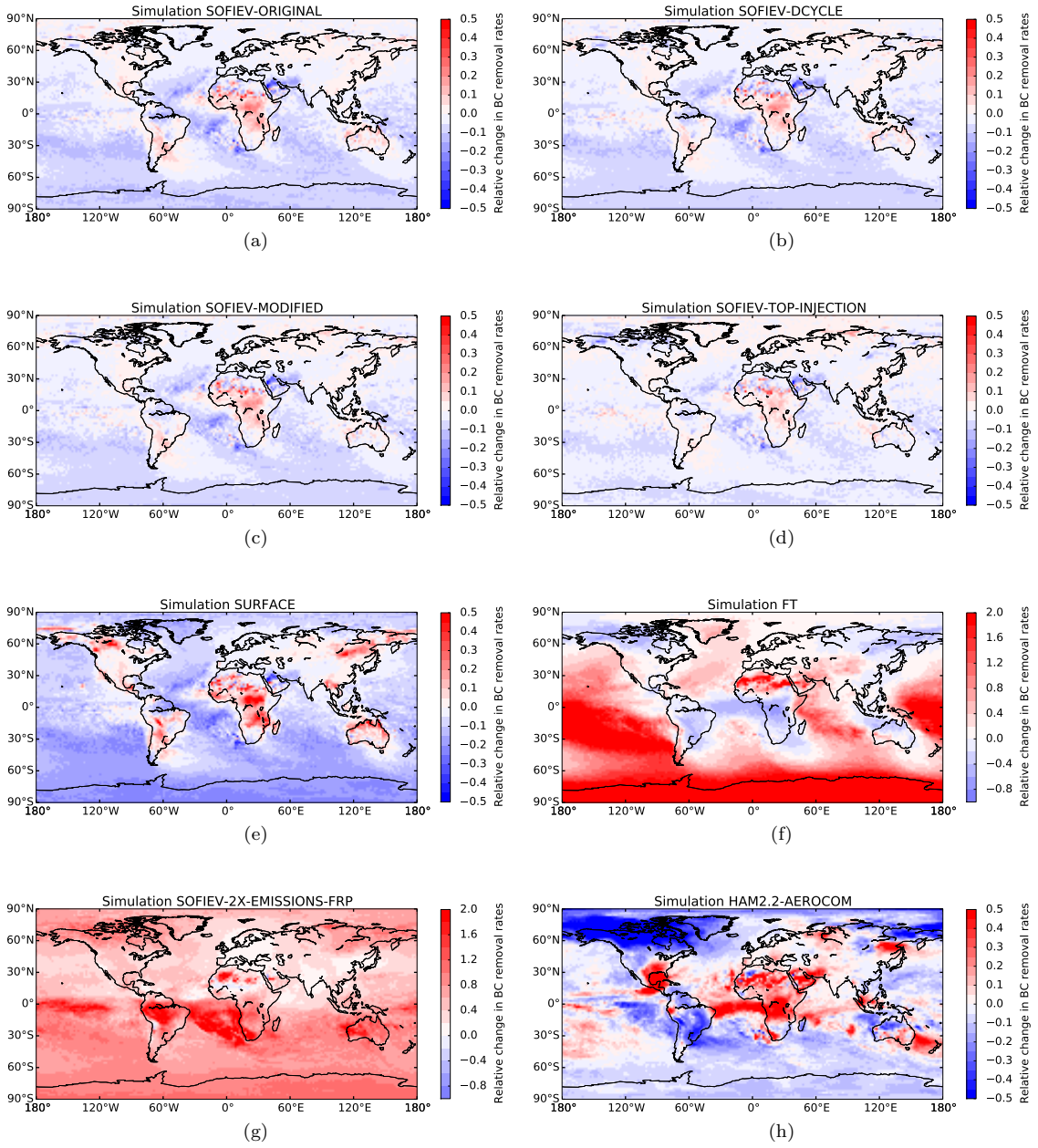

Figure 3.4: Simulated mean total deposition rates from 2005 to 2011. All relative changes refer to the standard implementation of prescribed emission heights combined with GFASv1.1 emissions (simulation HAM2.2-GFAS). A more detailed description of the simulation set-ups is provided in Table 3.1.

3.4.1 AERONET, MAN and MODIS

ECHAM6-HAM2 computes AOT at 550 nm for clear-sky conditions. The model calculates a separate relative humidity (RH) for the clear ($RH < 100\,\%$) and cloudy ($RH = 100\,\%$) parts of a grid box based on the grid box mean-specific humidity and the cloud fraction (see Stier et al., 2005, Sect. 2.6). The modeled AOT has global coverage and can be evaluated by comparison to observational AOT values which always refer to clear-sky conditions. Figures 3.5 and 3.6 provide a comparison of simulated and regionally averaged AOT to MODIS Aqua observations for the years 2006, 2007 and 2008. Time periods for which the NO-WILDFIRES values show little differences to all other simulations (e.g., Fig. 3.6, Boreal North America 2006, days 50–100 and Siberia 2008, days 250–300) indicate that the model bias in these periods has primarily to be attributed to non-wildfire sources. Generally those simulations based on GFAS emissions (HAM2.2-GFAS and SOFIEV-MODIFIED) perform better than the HAM2.2-AEROCOM simulation.

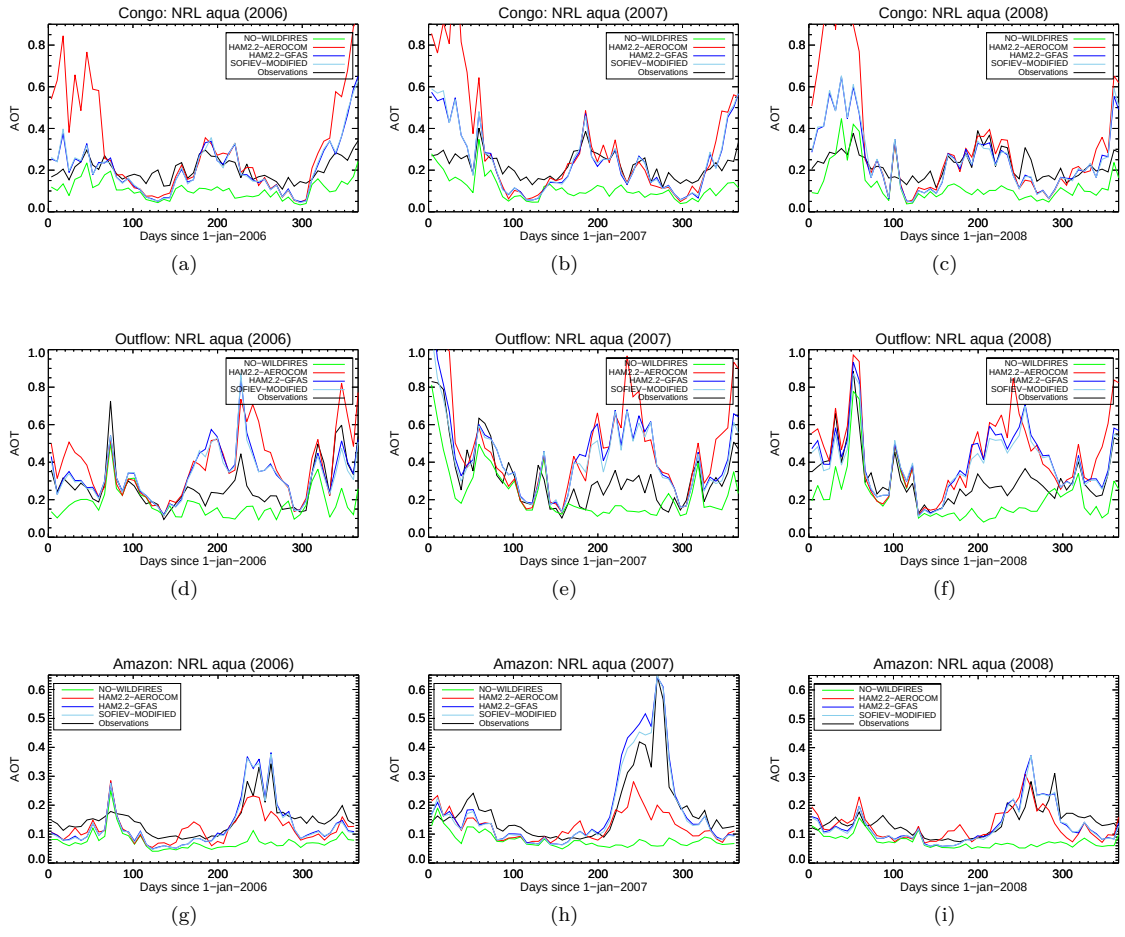

Figure 3.5: Temporal evolution of regional AOT for standard HAM2.2 emission heights based on GFAS emissions (HAM2.2-GFAS) respectively AEROCOM emissions (HAM2.2-AEROCOM) and a modified plume height parametrization of Sofiev et al. (2012) including a diurnal cycle of fire emissions and fire intensity (simulation SOFIEV-MODIFIED). The NO-WILDFIRES scenario is shown to distinguish wildfire-related biases from others. Observations are MODIS Aqua satellite measurements of AOT. All model data were collocated with the observations prior to averaging.

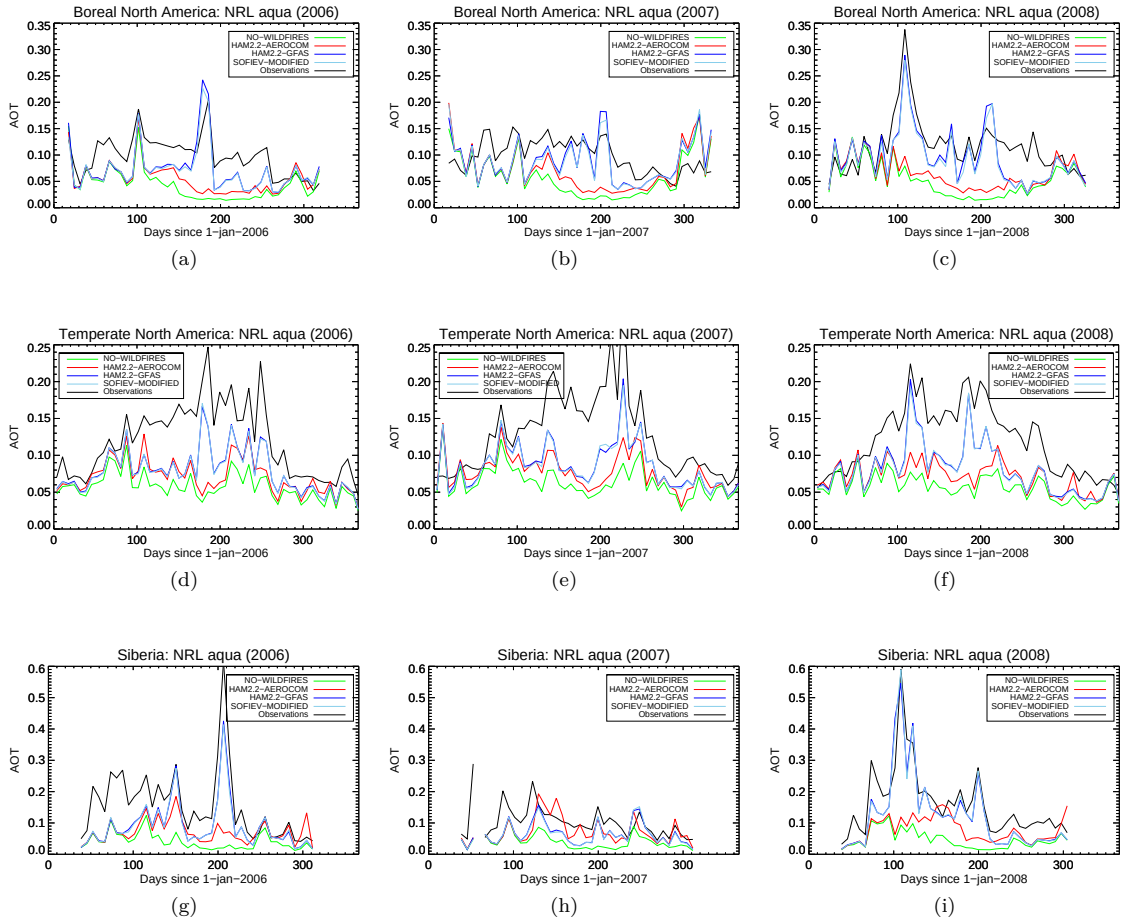

Figure 3.6: Temporal evolution of regional AOT for standard HAM2.2 emission heights based on GFAS emissions (HAM2.2-GFAS) respectively AEROCOM emissions (HAM2.2-AEROCOM) and a modified plume height parametrization of Sofiev et al. (2012) including a diurnal cycle of fire emissions and fire intensity (simulation SOFIEV-MODIFIED). The NO-WILDFIRES scenario is shown to distinguish wildfire-related biases from others. Observations are MODIS Aqua satellite measurements of AOT. All model data were collocated with the observations prior to averaging.

Note here that AEROCOM emissions represent a monthly climatology and are as such not expected to match the observations for specific time periods. Therefore, the HAM2.2-AEROCOM simulation should be seen as a crude approximation which only represents the basic seasonal and regional emission patterns. Due to the distinct differences in plume heights between HAM2.2-GFAS and SOFIEV-MODIFIED and subsequent changes in aerosol lifetime (see Table 3.2), larger AOT values can be observed for HAM2.2-GFAS, especially during the local burning season. In Siberia and boreal North America, the model performance is highly variable from year to year. While massive burning events in 2008 are captured very well by HAM2.2-GFAS and SOFIEV-MODIFIED simulations, large biases are observable for the weak burning periods in boreal North America 2006 and Siberia 2007 with negligible differences in performance between the two simulations. By implementation of the modified plume height parametrization (SOFIEV-MODIFIED), the overestimation in AOT observable for HAM2.2-GFAS over the Amazon region during 2007 can be slightly reduced for the major wildfire season. In the western Atlantic outflow

region of the central African smoke plumes, the model is generally less capable of capturing the magnitude and seasonality of AOT variations.

Figure 3.7 provides Taylor plots which illustrate the model performance with regard to correlations and standard deviations. The results show that the application of the fixed emission climatology AEROCOM is hardly able to improve the model performance compared to the NO-WILDFIRES scenario. Model runs with the GFAS emission inventory reach reasonable correlations of 0.4–0.85 depending on region and observational data set. The application of the Sofiev parametrization (SOFIEV-MODIFIED) instead of prescribed emission heights in HAM2.2-GFAS provides a moderate, but significant increase in correlation in boreal North America, Siberia and the Amazon. In the central African outflow region the biases of SD and correlation slightly increase, whereas there is no significant changes observable for temperate North America and the Congo region.

3.4.2 CALIOP

Figure 3.8 presents multi-year monthly AOT profiles (relative vertical AOT distribution) of ECHAM6-HAM2 simulations vs. CALIOP observations for the six regions specified in Fig. 3.1. For reasons of clarity, we limit our investigations to relative vertical AOT profiles and focus on the differences in AOT vertical profiles for prescribed (HAM2.2-GFAS and SURFACE) versus parametrized wildfire emission heights (SOFIEV-MODIFIED). In chapter 2 it has been shown that HAM2.2-GFAS overestimates plume heights by 1–2 km on average, while SOFIEV-MODIFIED offers the best plume height performance. Note that the lowest 1.5 km of all CALIOP profiles are known to include particularly high uncertainties which also impact the higher layers. Nevertheless, Fig. 3.8 shows that the vertical AOT patterns of CALIOP and the model simulations SOFIEV-MODIFIED, HAM2.2-GFAS and SURFACE show general agreement for boreal and temperate North America and Central Africa (Congo).

There is a tendency of the model to simulate higher AOT values in the extra-tropical FT than CALIOP (boreal North America, Siberia), but this feature is not necessarily related to shortcomings in the model, but could also be related to known underestimation of AOT for low AOT values in the CALIOP data set. Remarkably, the impact of the emission height implementation (HAM2.2-GFAS vs. SOFIEV-MODIFIED or SURFACE) is significantly smaller than the inter-annual variability and the differences between the model and CALIOP observations.

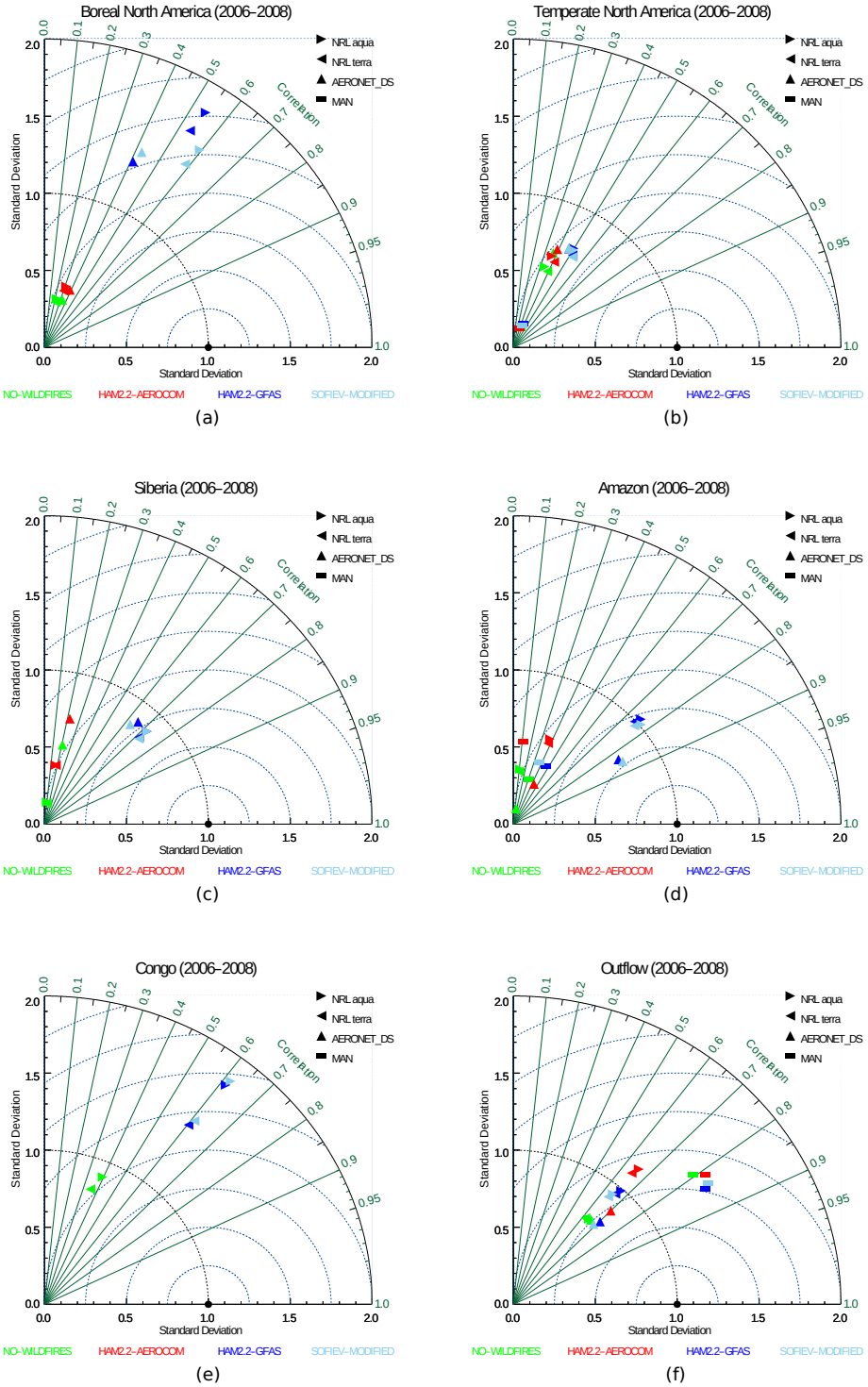

Figure 3.7: Taylor diagrams for comparison of simulations HAM2.2-AEROCOM, HAM2.2-GFAS and SOFIEV-MODIFIED to satellite observations (MODIS NRL Aqua, MODIS NRL Terra) and ground-based observations (AERONET_DS, MAN), see text for more detailed description of simulation set-ups and observational data sets. The NO-WILDFIRES scenario excludes all wildfire emissions. Note that for region Congo (e) simulation HAM2.2-AEROCOM is not shown, because the standard deviations exceed the scale range.

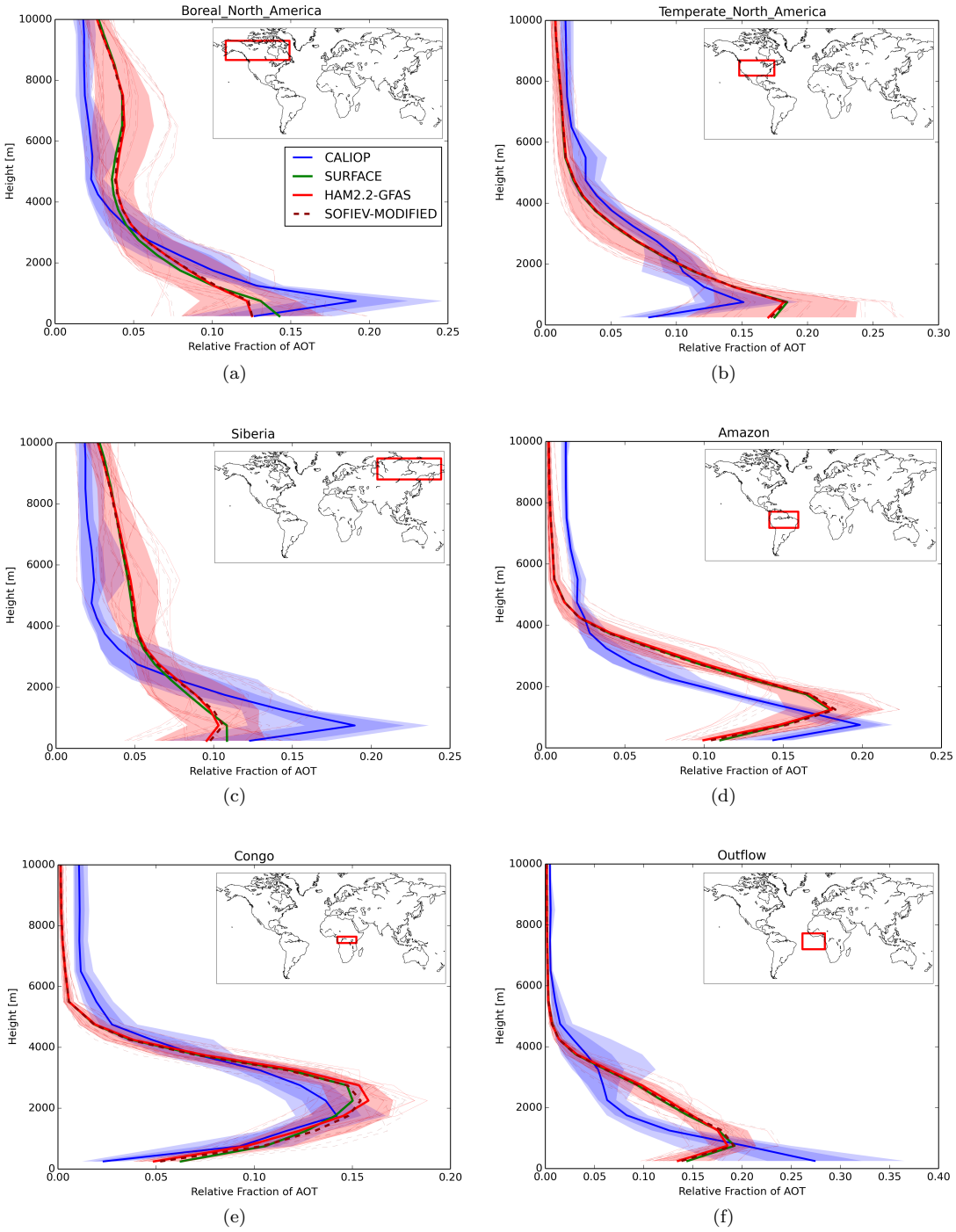

Figure 3.8: Regional AOT profiles averaged for 2006–2011 for CALIOP observations (solid blue line), simulation HAM2.2-GFAS (bold solid red line), simulation SOFIEV-MODIFIED (bold dashed dark red line) and simulation SURFACE (solid green line). Thin red lines indicate individual multi-year monthly means; red shading represents one SD of monthly variations for model simulation HAM2.2-MODIFIED. Dark blue shading indicates one SD of CALIOP monthly means; light blue shadings indicate minimum and maximum monthly means for CALIOP observations. All vertical lines represent relative AOT fractions at 532 nm (CALIOP) respectively at 550 nm (model simulations) of monthly averages for 2006–2011. Relative AOT fractions describe the integrated AOT of individual height layers (500 m intervals for 0–5 km, 1 km intervals for 5–10 km).

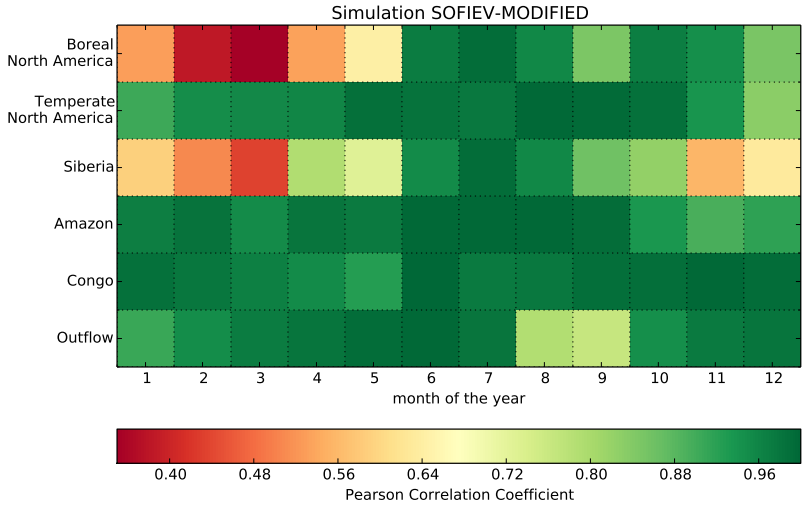

Figure 3.9: Pearson correlation coefficients of multi-year monthly means for CALIOP vs. SOFIEV-MODIFIED. Correlation coefficients greater than 0.48 are significant on a 95 % confidence interval, while correlations smaller than 0.48 are not significant.

As wildfire activity is seasonally varying, we further separate the analysis seasonally. Figure 3.9 provides correlation coefficients of spatially and temporally averaged relative AOT profiles for simulation SOFIEV-MODIFIED compared to CALIOP. For boreal North America and Siberia, a clear seasonal cycle in the model performance is observable with the highest correlations during the major wildfire season in these regions (June to August). Thus, the major shortcomings of the model in simulating vertical AOT profiles are not primarily related to wildfire emissions as such. Simulation HAM2.2-GFAS and simulation SURFACE show largely similar seasonal patterns in correlations (not shown). More realistic plume heights in simulation SOFIEV-MODIFIED compared to HAM2.2-GFAS increase the model performance in 65 % of all cases, but the differences in correlation range only between 0.001 and 0.038.

3.4.3 Comparison to former studies

Kipling et al. (2013) investigated the sensitivity of BC burdens and vertical profiles to emission heights in the ECHAM5-HAM2 and the Hadley Centre Global Environment Model version 3 – UK Chemistry and Aerosols (HadGEM3-UKCA) model. The authors found that differences in emission heights (PBL vs. prescribed 50–3000 m) did not significantly contribute to differences in the model performance. These findings are basically in line with our results which show that substantial differences in emission heights of 1–3 km entail differences of less than 10 % in global BC burdens at least for scenarios which inject emissions neither very close to the surface nor only into the FT. On the other hand, our evaluation of different plume height parametrizations also indicates that the application of a semi-empirical plume height parametrization which takes into account fire intensity as well as ambient meteorological conditions, marginally improves the overall model performance in AOT in the vicinity of regions with strong wildfire activity. Stein et al. (2009) also discovered a moderate improvement in model performance for the Hybrid Single Particle Lagrangian Integrated

Trajectory (HYSPLIT) model by application of a simple, empirical plume height parametrization (Briggs, 1969). Koffi et al. (2012) provided a comprehensive comparison of CALIOP AOT profiles to different model simulations including ECHAM5-HAM1. The spread of the model ensemble presented in that study is considerably larger than the impact of different emission height parametrizations in our study. The general CALIOP uncertainties in AOT profiles (e.g., Kacenelenbogen et al., 2011; Ma et al., 2013) exceed by far the uncertainties in emission heights. A minor general importance of emission heights compared to the large uncertainties in the emission inventories has also been found by Gonzi et al. (2015) for CO emissions.

3.5 Radiative forcing

The TOA RF of wildfire emissions is analyzed to quantify the climate impact caused by different emission height representations. Here, the RF represents exclusively the radiative perturbation that is introduced by wildfire emissions (BC, OC and SO_2), while anthropogenic emissions are kept constant. The radiative perturbation which is attributed to direct aerosol–radiation interference is referred to as *clear sky* RF; the RF which also includes indirect and semi-direct effects due to aerosol–cloud interaction is referred to as *total sky* RF. Aerosol-induced changes in atmospheric temperature profiles are implicitly included in both RF parameters, but due to our nudging towards reanalysis data every 6 h, they are partly suppressed. Figure 3.10a and b visualize the total sky and clear-sky TOA RF for different plume height implementations. Global mean values for the total sky RF are also provided in Table 2.4.

The differences in TOA RF introduced by the differences between the SOFIEV simulations are negligible (total sky TOA RF ranges between -0.196 ± 0.056 and $-0.211 \pm 0.060\,\mathrm{W\,m^{-2}}$). The most realistic implementation of emission heights (simulation SOFIEV-MODIFIED) leads to a TOA RF of $-0.20 \pm 0.07\,\mathrm{W\,m^{-2}}$ and is thus slightly less negative than the standard model HAM2.2-GFAS (total sky TOA RF of HAM2.2-GFAS: $-0.24 \pm 0.05\,\mathrm{W\,m^{-2}}$). The total sky TOA RF introduced by the extreme scenario of a SURFACE emission release is $-0.16 \pm 0.06\,\mathrm{W\,m^{-2}}$. Although the HAM2.2-GFAS simulation prescribes a certain emission injection into the FT for nearly all plumes, the difference in total sky TOA RF compared to the SURFACE simulation is only $0.08\,\mathrm{W\,m^{-2}}$.

The FT scenario entails a positive total sky TOA RF of $+0.66 \pm 0.24\,\mathrm{W\,m^{-2}}$ (not shown in Fig. 3.10). The change in the sign of the RF in the FT simulation can be attributed to the larger BC concentrations in the upper troposphere and lower stratosphere compared to the near-surface atmospheric levels. A doubling of FRP and emission fluxes in SOFIEV-2X-EMISSIONS-FRP entails a TOA RF of $-0.36 \pm 0.11\,\mathrm{W\,m^{-2}}$ which is nearly a doubling in the negative RF compared to SOFIEV-ORIGINAL. When the AEROCOM wildfire emissions are used (HAM2.2-AEROCOM), the total sky TOA RF is $-0.25 \pm 0.06\,\mathrm{W\,m^{-2}}$ which is comparable to the HAM2.2-GFAS simulation. Regionally, however, we find significant differences, that compensate on the global scale.

Figure 3.10c and d show the total respectively clear-sky surface RF for different plume height implementations. The surface RF of the simulation SOFIEV-ORIGINAL is $-1.62 \pm 0.17\,\mathrm{W\,m^{-2}}$ and ranges between the SURFACE and the HAM2.2-GFAS sim-

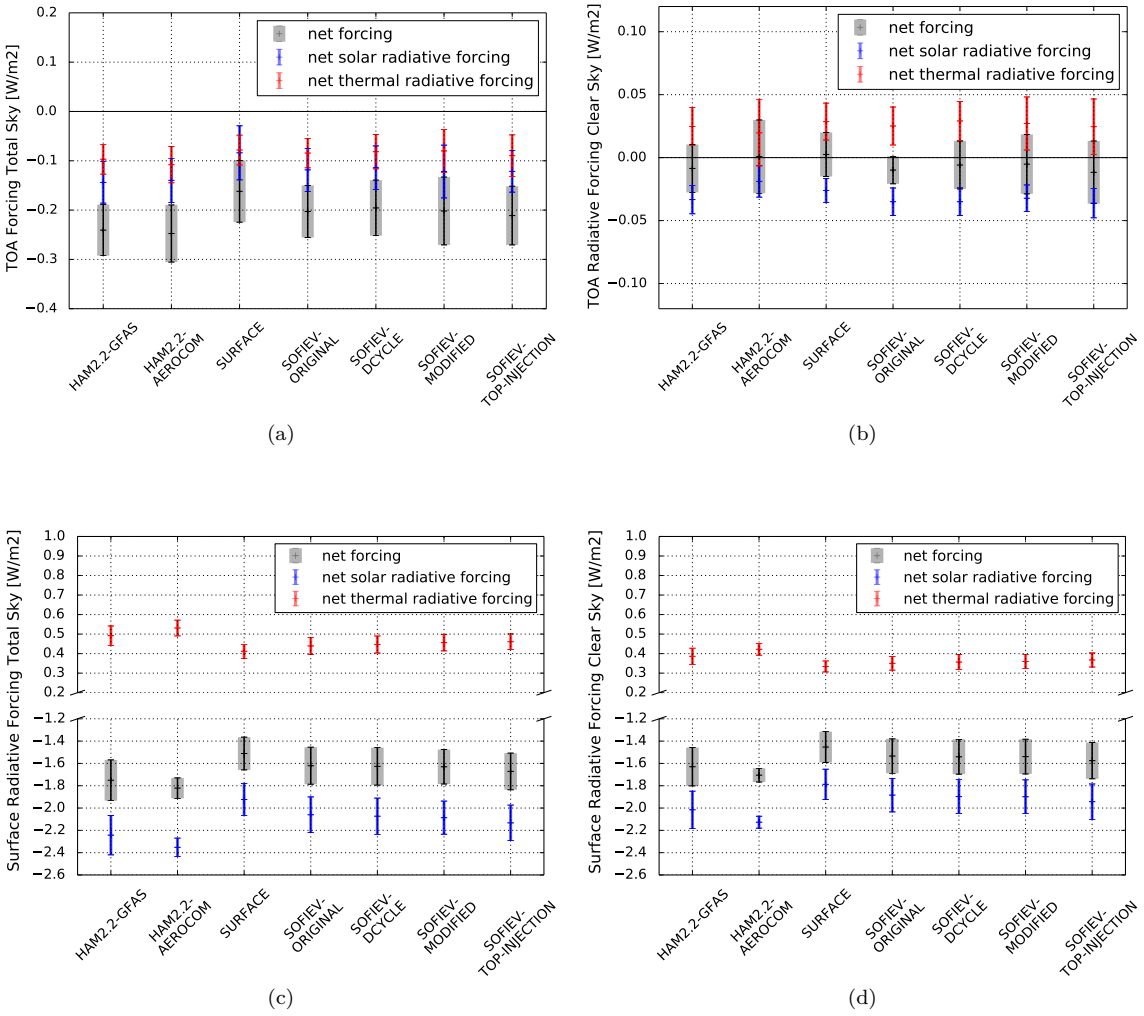

Figure 3.10: Simulated global mean net RF for TOA total sky **(a)**, TOA clear sky **(b)**, surface total sky **(c)** and surface clear sky **(d)**. The RF of all simulations refers to the NO-WILDFIRES scenario. Error bars indicate one SD of monthly mean RF values for 2005–2011. For a detailed description of the simulation set-ups, see Table 3.1.

ulation (see Fig. 3.10c). Neither the implementation of a diurnal cycle in fire emissions (SOFIEV-DCYCLE) nor a more realistic representation of deep plumes (SOFIEV-MODIFIED) alter the global surface RF by more then $\pm 0.05\,\mathrm{W\,m^{-2}}$. The same magnitude of changes in surface RF also applies for changes in the vertical distribution (SOFIEV-TOP-INJECTION). In contrast, the FT scenario causes a total sky surface RF of $-7.37 \pm 1.16\,\mathrm{W\,m^{-2}}$. A doubling in wildfire emissions and FRP would entail a total sky surface RF of $-3.28 \pm 0.34\,\mathrm{W\,m^{-2}}$ which represents roughly a doubling in surface RF compared to SOFIEV-DCYCLE ($-1.63 \pm 0.15\,\mathrm{W\,m^{-2}}$) applying the same emission height parametrization (not shown). Similarly to the TOA RF, the impact of the choice of the emission inventory on the global surface RF (HAM2.2-AEROCOM: $1.82 \pm 0.09\,\mathrm{W\,m^{-2}}$) is small. The ratio of TOA to surface RF ranges from 0.11 to 0.14 for all simulations except for the FT scenario. These similar TOA to surface RF ratios indicate that the aerosol–radiation interaction within the atmosphere shows a largely linear response to

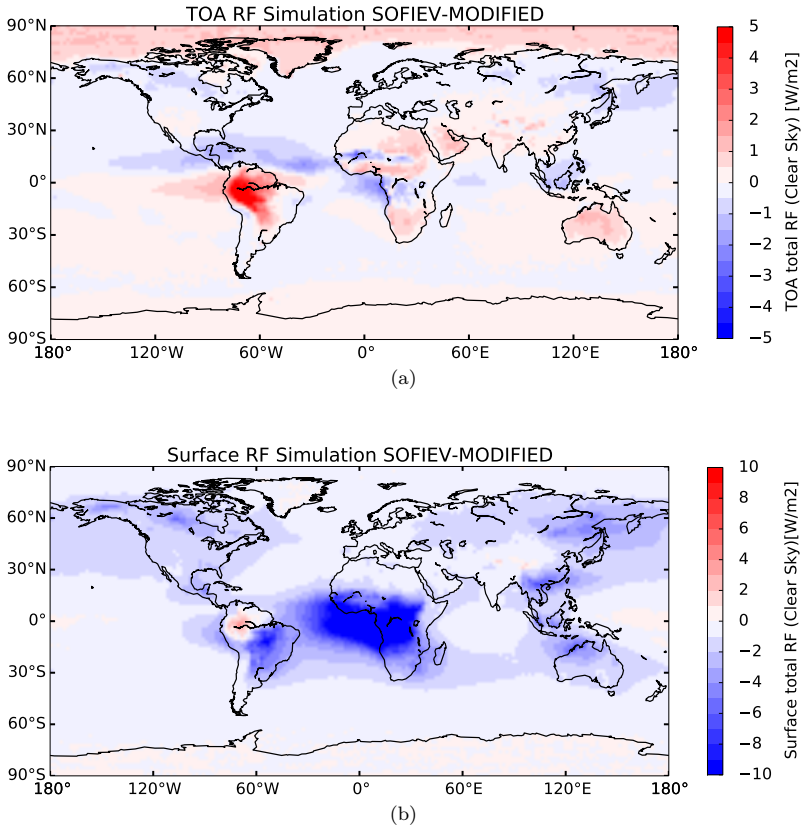

Figure 3.11: Clear sky Top of Atmosphere radiative forcing (top plot) and surface radiative forcing introduced by wildfire emissions (lower plot). Both figures show absolute differences of SOFIEV-MODIFIED (applying the plume height parametrization which matches best to observations) and the NO-WILDFIRES scenario for which all wildfire emissions were turned off.

moderate changes in plume heights of up to a few kilometers. In contrast, for the extreme FT scenario this largely linear response does not apply, because the absorption of solar radiation by BC particles in the stratosphere is particularly important.

Although the global RF introduced by wildfire emissions is negative for all realistic simulations, regionally, positive and negative TOA RF values are observable which exceed the global values by up to one order of magnitude. Global maps of the total sky TOA and surface RF introduced by wildfire emissions for the SOFIEV-MODIFIED simulation, which represents the most realistic emission height scenario, are shown in Fig. 3.11a and b. Maximum TOA RF positive values of up to $+5\,\mathrm{W\,m^{-2}}$ are found over central South America, while a negative TOA RF is observable over most parts of the oceans. Although emission heights have a similar range in the Amazon region and central Africa, the TOA RF in Amazon is clearly positive while regions of positive and negative TOA RF are found in Africa. In contrast, the largest regional radiative effects at the surface are detectable in the vicinity of the African source regions, where the negative surface RF exceeds mean values of $-10\,\mathrm{W\,m^{-2}}$. Between scenarios SURFACE, SOFIEV-ORIGINAL, SOFIEV-DCYCLE, SOFIEV-MODIFIED and SOFIEV-TOP-INJECTION, maximum changes in surface RF introduced by changes in emission heights in the order of 1–3 $\mathrm{W\,m^{-2}}$ are limited to tropical

Africa (not shown). In the extra-tropics, changes in surface RF rarely exceed $\pm 0.5\,\mathrm{W\,m^{-2}}$. In contrast, the switch from GFAS to AEROCOM emissions introduces a regional surface RF of 2–5 $\mathrm{W\,m^{-2}}$ in large parts of topical Africa, South America and also boreal North America.

Tosca et al. (2013) compared a simulation based on GFEDv3 wildfire emissions to a zero wildfire-emission control run to estimate the net change in surface shortwave fluxes in the Community Earth System Model (CESM). The authors only considered a prescribed wildfire emission release at the surface. The difference in net shortwave fluxes at the surface was found to be $-1.3 \pm 0.2\,\mathrm{W\,m^{-2}}$ leading to a surface cooling of $-0.13 \pm 0.01\,\mathrm{K}$. However, in contrast to our study, the sign of the TOA RF was positive ($+0.18 \pm 0.10\,\mathrm{W\,m^{-2}}$).

A strong surface RF over tropical Africa is observable in both studies, but extra-tropical RF patterns show larger differences. For the University of Oslo chemistry-transport model (Oslo-CTM2) model, simulations by Myhre et al. (2009) showed also a positive TOA RF value of $+0.07\,\mathrm{W\,m^{-2}}$. However, Jones et al. (2007) and Unger et al. (2010) found negative TOA RF values of $-0.29 \pm 0.07\,\mathrm{W\,m^{-2}}$ in the HadGEM1 model and $-0.25\,\mathrm{W\,m^{-2}}$ in the Goddard Institute for Space Studies (GISS) atmospheric composition–climate model. TOA RF values simulated by our ECHAM6-HAM2 simulations lie within the range of these references, but the spread between all our realistic simulations (-0.16 ± 0.06 to $-0.24 \pm 0.05\,\mathrm{W\,m^{-2}}$) is considerably smaller than the spread between the models. Presumably the differences in RF between the models are attributed to differences in transport mechanisms, removal processes and absorptivity of BC and OC, not to the emission heights.

3.6 Summary and conclusions

We have investigated the impact of wildfire emission heights on atmospheric BC concentrations, deposition rates and radiation using the aerosol–climate modeling system ECHAM6-HAM2. In addition to extreme scenarios of pure free-tropospheric and pure near-surface emission release, we implemented different versions of a simple plume height parametrization and compared the introduced changes in aerosol concentrations and radiation to simulations with prescribed HAM2 standard emission heights. A hypothetical scenario of a climate-change-induced doubling in emissions and fire intensity provided a first estimate of the relative importance of changes in total emissions and emission heights. By comparison of our simulations to AOT observations from AERONET, MODIS and CALIOP we quantified the magnitude of improvements for climate modeling that can be expected from the implementation of a simple plume height parametrization. Based on the analysis of our results, we present the following findings:

- The atmospheric BC burden, total deposition rates and atmospheric radiative transfer are more sensitive to emission inventories than to the details of the emission height implementation. The application of a diurnal cycle and a model-specific tuning of the plume height parametrization do not significantly change these results.

- Upper tropospheric and lower stratospheric BC concentrations are mainly determined by emission fluxes, tropical convection and the location of the emission release,

while emission heights are of limited importance.

- Future changes in emission fluxes were found to be more important than changes in emission heights.
- Considerable changes in mean plume heights of 1.1–2.5 km alter the mean annual BC deposition rates over in the Arctic and Antarctica by 5–25 % for the unrealistic scenario of prescribed emission release at the surface. Thus, BC deposition rates on snow and subsequent changes in surface albedo show only a moderate sensitivity on wildfire emission heights.
- Our comparison of modeling results to AERONET, MAN and MODIS observations indicates that the ECHAM6-HAM2 model is capable of capturing the magnitude of the AOT variability as well as the seasonality in the vicinity of regions with strong wildfire activity. Mean correlations of $R^2 = 0.4$–0.85 between simulated and observed instantaneous AOT values can be achieved for those regions of strong wildfire activity with small improvements introduced by the plume height parametrization.
- The comparison of simulated, vertically resolved AOT to CALIOP observations shows that close to the regions of strong wildfire activity, the implementation of the semi-empirical plume height parametrization marginally increases the model performance. Nevertheless, the CALIOP measurement uncertainties by far exceed the changes in AOT profiles caused by changes in wildfire emission heights.
- The top-of-atmosphere (TOA) radiative forcing (RF) of the wildfire emissions ranges between $-0.24 \pm 0.05\,\mathrm{W\,m^{-2}}$ for standard prescribed emission heights in ECHAM6-HAM2 (25 % of the emissions injected into the FT) and $-0.16 \pm 0.06\,\mathrm{W\,m^{-2}}$ for pure surface emission release. The application of a modified version of the Sofiev plume height parametrization, which offers the best match to observations, provides a TOA RF of $-0.20 \pm 0.07\,\mathrm{W\,m^{-2}}$ and thus shows little difference to the other plume height implementations. These changes in TOA RF are small compared to the spread of the overall wildfire emission RF in other state-of-the-art climate models (-0.3 to $+0.2\,\mathrm{W\,m^{-2}}$).

Based on these findings, we suggest that for current state-of-the-art climate and Earth system models, simple plume height parametrization are sufficient means to study global aerosol–climate interactions. More complex and advanced plume height models might be more appropriate tools for short-term regional studies of high resolution. Applying a correction factor of 3.4 to the GFAS wildfire emission inventory, fire emission heights turned out to be of limited importance compared to emission fluxes and removal processes. The assessment of the wildfire emission height impact on global BC concentrations, burden and deposition rates demonstrates that wildfire emission heights constitute only a second-order source of uncertainty. The known biases of global aerosol–climate models such as the improper representation of height-dependent aerosol–cloud interactions will persist even though emission heights are more appropriately represented.

Chapter 4

Wildfire emission fluxes, emission heights and black carbon concentrations in 2090-2099

4.1 Introduction

While consensus about a future decrease in carbonaceous aerosol emissions from anthropogenic sources has been achieved (Lamarque et al., 2011; Bond et al., 2013; Shindell et al., 2013), the future trend in aerosol emissions from wildfires is much more uncertain. This is due to the fact that the interactions between fire, land and atmosphere are very complex. First integrated approaches to assess post-fire changes in albedo, radiative forcing of emitted aerosols and subsequent feedbacks on climate have shown that the processes relevant for wildfire-climate interactions cover several magnitudes of temporal and spatial scales (Stavros et al., 2014, and references therein). However, the ability of state-of-the-art Earth system models to appropriately simulate vegetation-fire-climate interactions, is very limited (Carslaw et al., 2010; Ciais et al., 2013; Reichstein et al., 2013). To investigate the future climate impact of wildfires, we are in need of an improved coupling between vegetation-dynamics, wildfire activity, emission release and atmospheric aerosol transport. At the interface of terrestrial and atmospheric processes, emission heights are of importance, because they affect the impact of fire emissions on climate due to their influence on aerosol long-range transport, aerosol-cloud interaction and radiation (Luderer et al., 2006; Samset et al., 2013). On the other hand, emission heights themselves are strongly impacted by atmospheric stability and fire intensity, which are both expected to change in the future (e.g. Joshi et al., 2007; Luo et al., 2013).

First attempts to simulate future wildfire activity emerged in the early 90's (e.g. Flannigan and Wagner, 1991; Price and Rind, 1994; Beer and Williams, 1995). These approaches were based on global predictions of temperature and precipitation by various GCMs. Most of these studies assumed a doubling or triplication of atmospheric CO_2 concentrations and were limited to predictions of changes in the fire weather index (FWI) or burned area. A comprehensive summary of about 40 regional and global studies on the prediction of future fire activity is provided by Flannigan et al. (2009). While a general increase in

burned area and fire occurrence in the extra-tropics during the 21st century was indicated by most these studies, the magnitude of these changes remains uncertain. In the tropics, changes in wildfire activity have been projected to be less pronounced, but regionally strong enhancements as well as reductions in fire activity have been simulated (e.g. Liu et al., 2010b; Flannigan et al., 2013).

As most of the future fire probability projections are based on atmospheric parameters only, no wildfire emission estimates are provided, because these require vegetation-specific information on the biomass available for burning. Therefore recent efforts aim to implement process-based fire models into dynamic global vegetation models (DGVMs) allowing for interactive trace gas and aerosol emission estimates. The fire model SPITFIRE, for example, has been implemented into LPJ (Pfeiffer et al., 2013), JSBACH (Lasslop et al., 2014) and ORCHIDEE (Yue et al., 2014).

However, up to now, the radiative forcing of aerosol emissions from wildfires has primarily been investigated for present day (PD) climate conditions based on prescribed, satellite-based wildfire emission inventories, see e.g. Myhre et al. (2009), Unger et al. (2010) and chapter 3 of this thesis. The total wildfire top of atmosphere radiative forcing in current state-of-the-art climate-aerosol models ranges between $+0.18\pm0.10\,\mathrm{Wm}^{-2}$ (Tosca et al., 2013) and $-0.29\pm0.07\,\mathrm{Wm}^{-2}$ (Jones et al., 2007) for PD climate conditions. In contrast to the prescribed wildfire emission inventories used in the studies mentioned above, Ward et al. (2012) applied interactively simulated wildfire emission estimates based on a fire model by Kloster et al. (2012) and provided a first assessment of simulated wildfire activity, emission release and radiative forcing for the years 1850, 2000 and 2100. The authors found that fire emissions entail an overall negative radiative forcing for all time periods, but the contribution of trace gases and aerosols varies.

To our knowledge, up to now the impact of climate-induced changes in emission heights and their impact on atmospheric BC has not yet been investigated. In chapter 2 and chapter 3 of this thesis, a semi-empirical plume height parametrization was implemented in a global aerosol-climate model and, for the first time, the global emission height impact on atmospheric aerosol-long range transport and radiation for PD climate conditions was quantified.

In this chapter, we integrate fire emission estimates and interactively calculated fire emission heights for future climate conditions and quantify the impact of changes in emission fluxes and emission heights on atmospheric aerosol concentrations. The major research questions addressed are:

- How will wildfire emission fluxes change in the future?
- To what extent will changes in atmospheric conditions and changes in fire intensity impact fire emission heights?
- How will atmospheric BC concentrations respond to changes in wildfire emission fluxes, emission heights and atmospheric conditions?
- Which magnitude of changes in AOT is induced by changes in climate conditions and changes in emission fluxes?

To answer these questions, we use the process-based fire model SPITFIRE within the global vegetation model JSBACH and simulate global wildfire activity, fire intensity and emission fluxes for different Representative Concentration Pathway (RCP) scenarios in the 21st century. In a second step, we apply the global aerosol-climate model ECHAM6-HAM2 extended by a semi-empirical plume height parametrization with JSBACH-SPITFIRE emissions as boundary conditions to simulate aerosol transport, deposition rates and AOT for different RCP scenarios between 2090 and 2099. A range of sensitivity experiments allows us to disentangle the impacts of future changes in climate conditions, emission heights and emission fluxes on the atmospheric aerosol concentrations and AOT.

The next section introduces the specific model components and describes the simulation setup. In the results section, we analyze the contributions of changes in emission fluxes and emission heights on changes in simulated atmospheric BC concentrations and AOT at the end of the 21st century. In the conclusions section we summarize our findings and provide suggestions for future improvements in the representation of vegetation-fire-aerosol-climate interactions in Earth system models.

4.2 Methodology

In the following we introduce the DGVM and the atmospheric aerosol model, which are used to investigate wildfire emission fluxes and related atmospheric aerosol concentrations in a warmer future climate. Moreover, we describe the implementation of wildfire emission heights and the anthropogenic emission inventories applied in this study.

4.2.1 JSBACH-SPITFIRE model description

All fire-related processes and fire emission fluxes in this study are simulated by JSBACH-SPITFIRE (Lasslop et al., 2014) which is an implementation of SPITFIRE (Thonicke et al., 2010) in JSBACH (Brovkin et al., 2013; Reick et al., 2013; Schneck et al., 2013). JSBACH is the land component of the Max Planck Institute Earth System Model (MPI-ESM, Giorgetta et al. 2013). SPITFIRE is a process-based fire model which simulates fires based on guiding physical principles. The number of natural and human ignitions is combined with the rate of fire spread and the fire duration to estimate the burned area. Based on the biomass burned, SPITFIRE calculates daily total carbon emissions which are transformed into aerosol emissions following vegetation-specific emission factors (Akagi et al., 2011).

JSBACH-SPITFIRE is run as described in Lasslop et al. (2014), but for our simulations the dependency of fire size on population density is based on a linear decreasing relationship between population density and observed mean fire size in MODIS data (Hantson et al., 2015). Moreover, the diagnostic parameter total fire radiative power (FRP) of all fires in a particular grid cell was implemented. We consider that only the fuel classes 1 h to 100 h (representing leaves, small branches and large branches) contribute to the flaming process, but not the 1000 h fuel class (representing trunks). In SPITFIRE, the consumed fuel f_{1-100h} of the fuel classes 1 h to 100 h is a function of the biomass available for burning, the fuel moisture and the wind speed. For a more detailed description see Appendix A

of Thonicke et al. (2010) and Lasslop et al. (2014). Following the average consumed fuel per unit area [g biomass m^{-2}] simulated by JSBACH-SPITFIRE and assuming a constant heat capacity h, we derive the diagnostic variable *mean daily FRP*:

$$FRP = \alpha \cdot \frac{f_{1-100h}}{86400\,s} \cdot A \cdot h \tag{4.1}$$

where α describes the fraction of energy which is released as radiation. Here, we choose a globally constant value of $\alpha = 0.15$ based on the references by Wooster et al. (2005), Freeborn et al. (2008), Kremens et al. (2012), Morandini et al. (2013) and Smith et al. (2013), which provide values for α that range between 0.12 and 0.17 for different vegetation types. The parameter A describes the specific grid cell area. For the heat capacity h we apply a constant value of 18,000 Jg^{-1}, which represents an average of experimentally found heat capacity values (e.g. Dickinson and Kirkpatrick, 1985; Reid and Robertson, 2012, and references therein) that are widely used in fire spread models (e.g. Andrews, 2009; Thonicke et al., 2010). Note that the FRP values calculated by equation 4.1 represent the mean total FRP of all fires burning in a grid box, not of individual fires. They are basically comparable to assimilated mean daily FRP values in the Global Fire Assimilation System (GFAS), a satellite-based FRP and emission data set (Kaiser et al., 2012).

Due to the fact that emission heights need to be calculated for individual fires rather than for a mean fire state of a grid box, FRP and emissions, which are only provided as grid box means by JSBACH-SPITFIRE, have to be distributed to individual fires. Therefore, we implement a statistical-empirical distribution function which is based on global mean FRP distributions for single fires in the GFASv1.2 data set. A more detailed description of the FRP distribution scheme, which we implemented in JSBACH-SPITFIRE, is provided by Appendix A.1. An evaluation of the normalized JSBACH-SPITFIRE FRP distribution for PD climate conditions against GFAS is provided in the results section.

The fraction of carbon emitted as black carbon (BC) and organic carbon (OC) is calculated using species-specific wildfire emission factors by Akagi et al. (2011). We also use Akagi et al. (2011) emission factors for SO_2 except for extra-tropical forests, which are not specified in this reference. For the latter we apply emission factors from Andreae and Merlet (2001). For all emission factors, plant functional types (PFTs) in JSBACH are attributed to land cover types (LCTs) provided by Akagi et al. (2011) as shown in Table 4.1.

All JSBACH-SPITFIRE simulations are run for 1850–2005 as described in Lasslop et al. (2014), except that atmospheric forcing is provided by MPI-ESM model output of the model intercomparison project CMIP5 (Giorgetta et al., 2013) and not from reanalysis data. For 2006–2100, MPI-ESM model output for the RCP scenarios RCP2.6, RCP4.5 and RCP8.5 is applied (van Vuuren et al., 2011). Population density for 1850–2005 is prescribed according to the HYDE data base (Goldewijk, 2001; Klein Goldewijk and Verburg, 2013) and has been extended for the years 2006–2100 by population density changes predicted from Shared Socio–economic Pathways (SSPs) relative to HYDE data for 2010. Combinations of SSP and RCP scenarios are chosen according to the suggestions by van Vuuren and Carter (2014): RCP2.6 + SSP1, RCP4.5 + SSP1 and RCP8.5 + SSP3. Land use change is taken from Hurtt et al. (2011).

Table 4.1: Attribution of JSBACH plant functional types (PFTs) to land cover types (LCTs) for emission factors described in Akagi et al. (2011).

JSBACH PFT	**Attributed Akagi LCT**
Tropical Evergreen Trees	Tropical Forest
Tropical Deciduous Trees	Tropical Forest / Savanna [1]
Extra-tropical Evergreen Trees	Extra-topical Forest
Extra-tropical Deciduous Trees	Extra-topical Forest
Raingreen Shrubs	Savanna / Chaparral [2]
Deciduous Shrubs	Savanna / Chaparral [2]
C3 Grass	Savanna
C4 Grass	Savanna
C3 Pasture	Pasture / Savanna [3]
C4 Pasture	Pasture / Savanna [3]
C3 and C4 Crops	Crops [4]

[1] According to the definition of Savanna in Akagi et al. (2011), the JSBACH PFT Tropical Deciduous Trees is attributed to Akagi Tropical Forest, if the sum of the JSBACH PFTs Tropical Evergreen Trees and Tropical Deciduous Trees is greater than 60 %, otherwise it is assigned to the Akagi LCT Savanna.

[2] JSBACH Raingreen Shrubs and Deciduous Shrubs are assigned to the Akagi LCT Savanna in the tropics and the Akagi LCT Chaparral in the extra-tropics.

[3] JSBACH C3 Pasture and C4 Pasture are assigned to the Akagi LCT pasture only if the Pasture fraction is larger than 50 %, otherwise they are attributed to the Akagi LCT Savanna.

[4] Crops in JSBACH are prescribed to be not affected by fires.

4.2.2 ECHAM6-HAM2 model description

In a second step, we use the global circulation model ECHAM6 extended by the aerosol module HAM2 to simulate atmospheric circulation, aerosol microphysics and radiation. ECHAM6, the atmospheric component of MPI-ESM (Giorgetta et al., 2013; Stevens et al., 2013), is run at a horizontal resolution of approximately 1.9° x 1.9° with 47 vertical layers from the surface up to 0.01 hPa; a time step of 10 min is applied. For the RCP scenarios 2090–2099 sea surface temperature (SST) is prescribed according to MPI-ESM CMIP5 simulations, whereas for PD simulations, it is prescribed according to the Atmospheric Model Intercomparison Project AMIP (Hurrell et al., 2008). The aerosol component HAM2 (Stier et al., 2005; Zhang et al., 2012a) models the transport and removal of trace gas and aerosol species including, among others, BC, OC and SO_2, which represent the major wildfire emission species. Aerosol emissions are thereby prescribed as boundary conditions. By use of Mie theory, aerosol optical properties are calculated for 24 solar spectral bands

and serve as input for the ECHAM6 radiation scheme. In addition, a two-moment cloud microphysics scheme (Lohmann et al., 2007) coupled to the aerosol microphysics, enables the simulation of aerosol-cloud interactions.

4.2.3 Wildfire emission heights

Maximum emission heights in ECHAM6-HAM2, also referred to as "top plume heights", are simulated by a semi-empirical plume height parametrization, which is based on the parameters FRP (P_f), Brunt-Väisälä frequency of the atmosphere (N) and PBL height (H_{PBL}). Originally developed by Sofiev et al. (2012), we apply the ECHAM6-HAM2 specific modifications presented in chapter 2 of this thesis including a tuning of FRP for high plumes and the introduction of a diurnal cycle in FRP. Top plume heights (H_p) are simulated as follows:

$$H_p = \alpha H_{PBL} + \beta \left(\frac{P_f}{P_{f0}} \right)^{\gamma} exp\left(-\delta N^2 / N_0^2 \right) \tag{4.2}$$

whereupon

$$P_f = \begin{cases} P_f & \text{if } H_p \leq 1500\,m \\ P_f \times \left(\frac{H_p}{1500\,m} \right)^{0.5} & \text{if } H_p > 1500\,m \end{cases} \tag{4.3}$$

The reference Brunt-Väisälä Frequency (N_0) and the reference FRP (P_{f0}) hold fixed values of $N_0 = \sqrt{2.5 \,\mathrm{x}\, 10^{-4}}\, s^{-1}$ and $P_{f0} = 10^6\, W$, respectively. The constant values of α, β, γ and δ have been determined by use of a computational learning data set; for more detailed information see Sofiev et al. (2012). We distribute all wildfire emissions vertically with constant mass mixing ratio from the top of the plume to the surface.

In order to save computational time, we apply a slightly modified FRP binning scheme as presented in chapter 2 of this thesis. This FRP class scheme summarizes individual fires of similar FRP in specific bins and runs the plume height parametrization only once for each bin. In contrast to the individual observational FRP values of FRP bins 27–41 applied in chapter 2, here the JSBACH-SPITFIRE FRP distribution scheme (see Sect. 4.2.1) requires fixed FRP values for the FRP bins 27–41. Furthermore, we enlarge the number of bins from 41 to 47 to improve the representation of very intense fires. Table 4.2 provides a summary of the FRP bin ranges and bin widths applied in the present study.

Table 4.2: Description of the applied FRP binning scheme which groups fires of a certain FRP range. Mean FRP bin values serve as input for the plume height parametrization applied in ECHAM6-HAM2.

FRP bin No.	**1–10**	**11–15**	**16-21**	**22–31**	**32–38**	**39–43**	**44–46**	**47**
FRP range [MW]	0–100	100–200	200–500	500–1500	1500–5000	5000–10000	10000–25000	25000–50000
Bin width [MW]	10	20	50	100	500	1000	5000	25000

4.2.4 Emission inventories

Wildfire emissions in the ECHAM6-HAM2 simulations are either based on JSBACH-SPITFIRE emissions for PD climate conditions (1996–2005) or JSBACH-SPITFIRE RCP scenarios for 2090–2099. In addition, we run one simulation with GFASv1.2 emissions for 2003–2011 to provide a satellite-based reference simulation for PD conditions. Anthropogenic and biogenic emissions are taken according to the HAM2.2 standard setup using AEROCOM phase II emissions for all simulations (Stier et al., 2005; Dentener et al., 2006). These represent PD emission inventories. To estimate the relative importance of changes in wildfire emissions compared to future changes in anthropogenic BC emissions, we also apply projected changes in anthropogenic BC emissions according to RCP8.5 (Lamarque et al., 2011) for one simulation. Dust, sea salt and dimethyl sulfide (DMS) emissions are calculated interactively in ECHAM6-HAM2.

4.2.5 Experiment setup

We run three JSBACH-SPITFIRE simulations for the scenarios RCP2.6, RCP4.5 and RCP8.5. These simulations provide the wildfire emission and FRP input for the ECHAM6-HAM2 simulations. All scenarios are carried out for the time period 1850–2100 as described in Sect. 4.2.1. The vegetation carbon pools are run into equilibrium prior to 1850 realized by a spin-up of 300 years. The model spin-up equilibrates the fast carbon pools, whereas slow carbon pools are not considered and do not interact with fires. The setup of the ECHAM6-HAM2 simulations is described in Table 4.3.

Table 4.3: Setup of ECHAM6-HAM2 experiments. All SPITFIRE simulations and the CLIMATE-ONLY experiment use wildfire emissions from JSBACH-SPITFIRE output. Simulation 'PD-GFAS' employs wildfire emissions from the Global Fire Assimilation System (GFAS) for the period 2003–2011. Emission heights are calculated by a modified version of the Sofiev plume height parametrization. See text Sect. 4.2.3 to 4.2.5 for more detailed information.

Simulation Name	**Time Period**	**Climate Scenario**	**Anthropogenic Emissions**	**Wildfire Emissions & FRP**
RCP2.6-SPITFIRE	2090–2099	RCP2.6	AEROCOM 2000	SPITFIRE RCP2.6
RCP4.5-SPITFIRE	2090–2099	RCP4.5	AEROCOM 2000	SPITFIRE RCP4.5
RCP8.5-SPITFIRE	2090–2099	RCP8.5	AEROCOM 2000	SPITFIRE RCP8.5
PD-SPITFIRE	1996–2005	AMIP	AEROCOM 2000	SPITFIRE PD
CLIMATE-ONLY	2090–2099	RCP8.5	AEROCOM 2000	SPITFIRE PD
RCP8.5-SPITFIRE+ ACCMIP-2090	2090–2099	RCP8.5	ACCMIP RCP8.5 2090	SPITFIRE RCP8.5
PD-GFAS	2003–2011	AMIP	AEROCOM 2000	GFASv1.2 2003–2013

The ECHAM6-HAM2 experiments RCP2.6-SPITFIRE, RCP4.5-SPITFIRE and RCP8.5-SPITFIRE are run for the period 2090–2099. They combine the change in wildfire emissions, FRP and projected changes in climate, which impact emission heights, dust, DMS and sea salt mobilization, aerosol transport and aerosol removal rates. Compared to simulation PD-SPITFIRE, which represents PD wildfire emissions and climate, these simulations demonstrate the potential effects of climate-induced changes in wildfire emissions on atmospheric aerosol concentrations in a warmer climate at the end of the 21st century. In experiment CLIMATE-ONLY, PD SPITFIRE emission fluxes are applied together with future climate conditions from the RCP8.5 scenario. The comparison of simulation CLIMATE-ONLY to simulation RCP8.5-SPITFIRE enables us to disentangle the combined impact of changes in FRP, emission fluxes and emission heights from changes caused by altered atmospheric conditions alone.

Simulation RCP8.5-SPITFIRE+ACCMIP-2090 is identical to RCP8.5-SPITFIRE except for the anthropogenic emissions which represent projected future RCP8.5 emissions of the year 2090 (Lamarque et al., 2011). These anthropogenic ACCMIP BC emission projections for the year 2090 are only 47 % of the PD anthropogenic AEROCOM BC emissions used in all other simulations. Thus, the comparison between simulation RCP8.5-SPITFIRE+ACCMIP-2090 and RCP8.5-SPITFIRE provides an estimate of how the relative wildfire contribution to the overall aerosol concentrations might change in the future due to changes in anthropogenic aerosol emissions. The last simulation called PD-GFAS applies satellite-based wildfire emission estimates reported in GFASv1.2 for 2003–2011. It represents a reference simulation for the comparison of JSBACH-SPITFIRE emissions in PD climate conditions to satellite-based emission estimates. Although GFASv1.2 data were available for 2003–2013 at the start of this study, the availability of AMIP SST and sea ice was limited to 2003–2011; therefore simulation PD-GFAS covers only the period 2003–2011. For all scenarios, one year of ECHAM6-HAM2 model spin-up is run prior to the start year of the simulations.

SPITFIRE emissions have been tuned against the Global Fire Emissions Database (GFED, van der Werf et al. (2010)), which are known to results in a global underestimation of AOT. Therefore, we apply a zero-order emission correction factor of 3.4 for wildfire emissions as described in Huijnen et al. (2012), Kaiser et al. (2012) and von Hardenberg et al. (2012) for all simulations.

4.3 Analysis of model simulations

First, we will discuss the simulated JSBACH-SPITFIRE emission fluxes (Sect. 4.3.1) and JSBACH-SPITFIRE FRP (Sect. 4.3.2) for PD climate conditions including a comparison to satellite-based data sets. Second, we will analyze the differences in emission fluxes between the RCP scenarios for 2090–2099 and discuss the changes compared to PD climate conditions (Sect. 4.3.3). In Sect. 4.3.4 potential drivers for the simulated regional changes in future wildfire emission fluxes will be investigated. In a third step, we will assess the resulting changes in emission heights, atmospheric BC concentrations and AOT (Sect. 4.3.5, 4.3.6 and 4.3.7, respectively).

4.3.1 Emission estimates for present day climate conditions

The ability of an interactive fire model to realistically simulate global fire activity and fire emissions is largely determined by the process representation of the fire model itself, the general performance of the global vegetation model and the meteorological forcing applied. A detailed general analysis of the JSBACH-SPITFIRE model performance has been discussed by Lasslop et al. (2014). Here, we focus on the evaluation of simulated emission fluxes and FRP against satellite-based emission and FRP inventories. Figure 4.1 illustrates a comparison of the mean global total wildfire emission release simulated by JSBACH-SPITFIRE to the satellite-based emission inventories GFASv1.2 (2003–2013) and GFEDv2 (1997–2008).

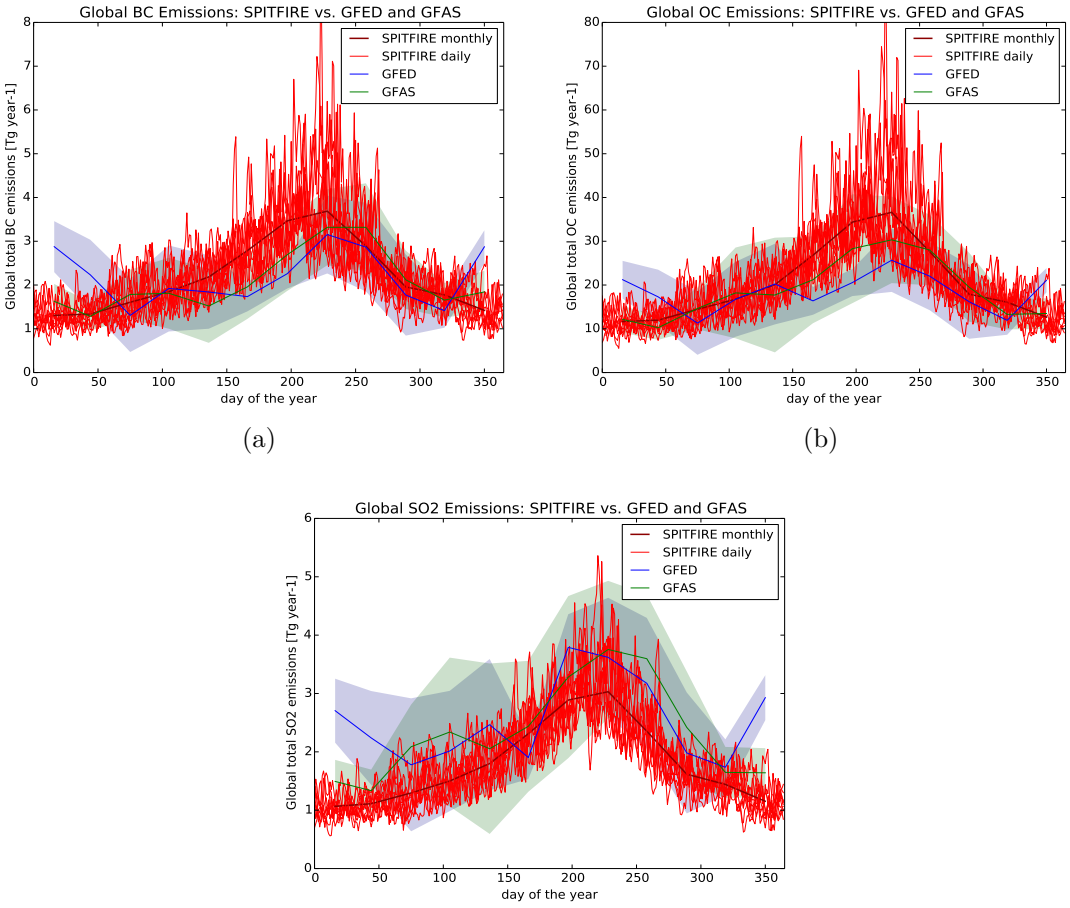

Figure 4.1: Global mean emission fluxes of BC (a), OC (b) and SO_2 (c) from wildfires simulated by JSBACH-SPITFIRE for the years 1996–2005 compared to multi-year monthly means of the satellite-based emission inventories GFED and GFAS. Blue and green shadings represent one standard deviation of multi-year monthly means in the observational data sets.

The global total wildfire BC emissions simulated by JSBACH-SPITFIRE for the years 1996–2005 lie approximately 5 % above the satellite-based emission inventories GFED and GFAS. For OC, the JSBACH-SPITFIRE emission estimates are 13 % and 8 % larger than

GFED and GFAS, respectively; for SO_2 negative discrepancies of -28 % and -23 % are found. The seasonality is only partly captured by the model with a slightly too early onset of the Northern Hemispheric fire season. The large differences in emission flux estimates between GFED and GFAS in January and February, however, depict the large uncertainties which are included in the satellite-based data sets. Overall, the differences between the simulated and the satellite-based global emission estimates lie within the range of the natural inter-annual variations indicating a reasonable global model performance of JSBACH-SPITFIRE.

4.3.2 FRP estimates for present day climate conditions

As described in Sect. 4.2.1, only the daily mean total FRP of a grid cell is calculated by the JSBACH-SPITFIRE model. The distribution of the total FRP to individual fires is realized by an empirical-statistical distribution scheme which is described in more detail in Appendix A.1. Figure 4.2 shows a comparison of the number of fires and individual FRP values simulated by the empirical FRP distribution scheme applied in the JSBACH-SPITFIRE simulations to assimilated observational data from GFAS.

Although the transitions between FRP bins with different widths (see Table 4.2) are slightly smoothed out by the empirical distribution scheme, the JSBACH-SPITFIRE FRP spectrum follows the basic shape of the observational GFAS FRP distribution. Taking into account the large measurement uncertainties included in GFAS, the model describes a reasonable distribution of FRP to individual FRP classes.

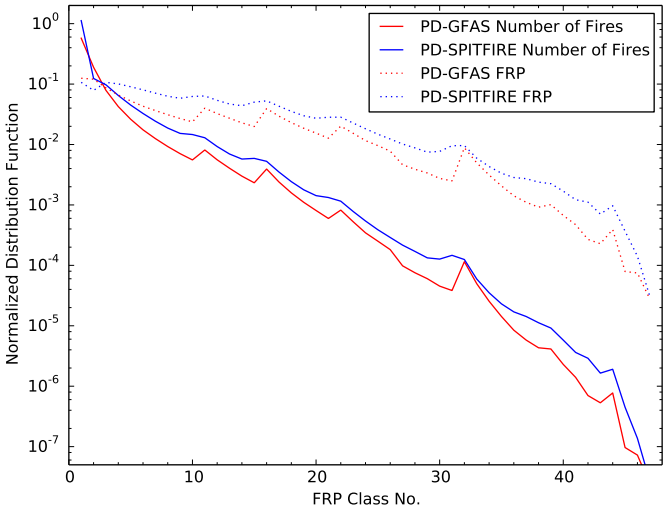

Figure 4.2: Global mean attribution of normalized FRP and number of fire distributions to FRP classes. Blue lines represent simulated JSBACH-SPITFIRE distributions (1996–2005), red lines show observational GFAS data (2003–2013). For a description of the FRP class scheme, see Sect. 4.2.3, respectively Sect. 2.2.4.

The global mean FRP simulated by JSBACH-SPITFIRE (1996–2005) is approximately 47 % higher than the GFAS global average for 2003–2013. This discrepancy can partly be explained by the fact that a large number of small fires is not included GFASv1.2

(due to the lower detection limit of the MODIS instrument) but simulated by JSBACH-SPITFIRE. Note that the assimilation techniques applied for low FRP fires in GFAS have changed from GFASv1.1 to GFASv1.2 leading to a significant reduction of fires with FRP values smaller than 1 MW in GFASv1.2.

However, Fig. 4.3 demonstrates that, regionally, the modeled FRP shows substantial differences to the satellite-based FRP patterns. These differences are most pronounced in Central North America and Australia. Most likely these bias patterns can be primarily attributed to an overestimation in the modelled JSBACH net primary productivity (NPP) and the available fuel in these regions (Lasslop et al., 2014). In boreal regions of North America and Eurasia, emission fluxes and FRP are presumably also underestimated by SPITFIRE because of a distinct underestimation in the number of simulated human ignition events and meteorological conditions favorable for fires. In contrast, the FRP patterns of SPITFIRE show good agreement to GFAS in large parts of the tropics which represent the major source regions of wildfire emissions globally.

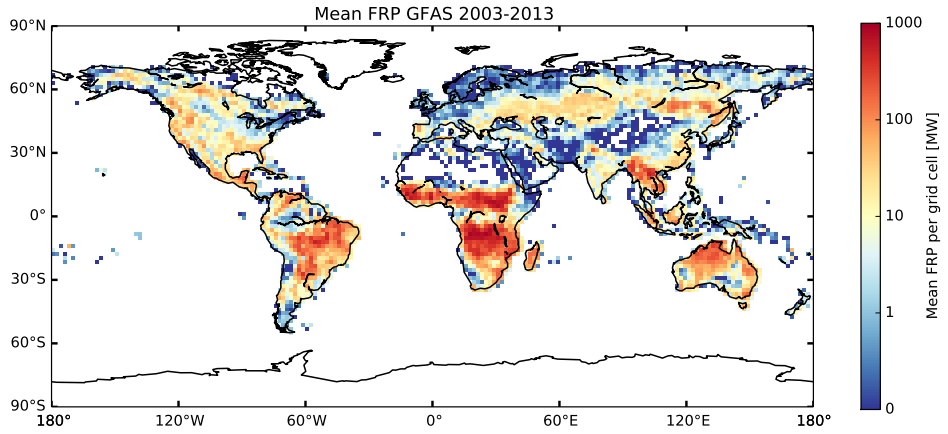

(a)

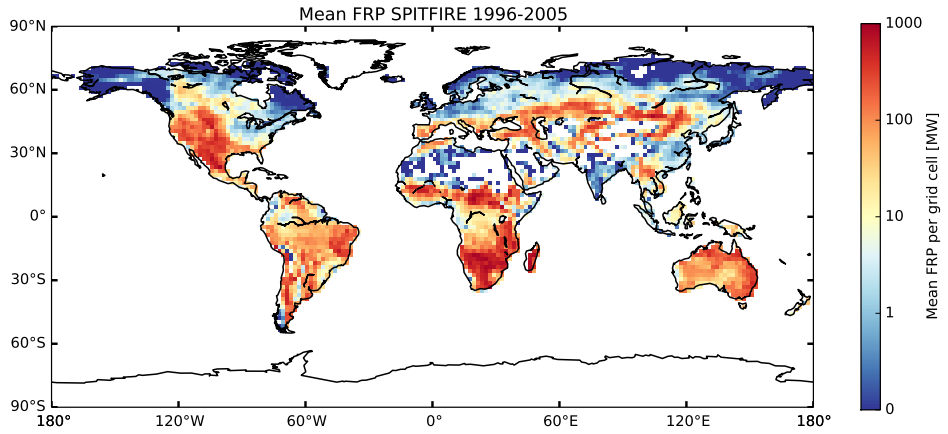

(b)

Figure 4.3: Mean annual FRP per grid cell in the observational GFAS data set 2003–2013 (a) and simulated by JSBACH-SPITFIRE for 1996–2005 (b).

General region-specific discrepancies in wildfire emission estimates between implementations of SPITFIRE in DGVMs and the satellite-based GFED data set have also been identified in previous studies. Yue et al. (2014) implemented the SPITFIRE model into the global vegetation model ORCHIDEE. The authors found similar regional bias patterns in SPITFIRE burned area and wildfire emission fluxes compared to GFED. Nevertheless, other satellite-based data sets (e.g. L3JRC and GLOBCARBON) provide burned area estimates, which show significantly better agreement to SPITFIRE, e.g. in North America (Yue et al., 2015). For Central Africa, Zhang et al. (2014) analyzed eight different satellite-based emission estimates and found large variations between the observational data sets of up to a factor of 10. These regional differences are even larger than most of the regional biases we detect when comparing JSBACH-SPITFIRE to GFAS and GFED.

4.3.3 Changes in wildfire emission release over the 21st century

Simulated changes in wildfire activity within the 21st century are driven by the complex interaction of human activity, climate change and changes in vegetation cover. A time series of the total global wildfire carbon emissions simulated by JSBACH-SPITFIRE between 1996–2100 is provided by Fig. 4.4. To understand the projected changes in future wildfire carbon emissions, a more detailed analysis of the regional modifications is required.

Figure 4.5 presents global maps of the relative changes in BC emission fluxes for all RCP scenarios 2090–2099 vs. 1996–2005. A general increase in boreal wildfire emissions is simulated for all RCP scenarios, with the magnitude of the increase gradually strengthening from RCP2.6 to RCP8.5. While emissions in Africa are consistently simulated to decrease for all RCP scenarios, other tropical and subtropical regions (e.g. the Amazon and South East Asia) show different directions of changes in emission fluxes.

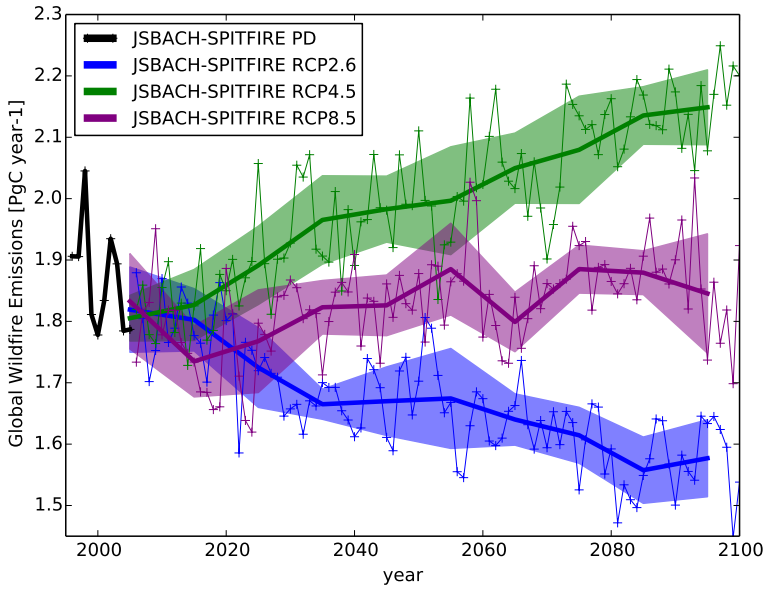

Figure 4.4: Time series of total C emissions simulated by JSBACH-SPITFIRE for PD and RCP scenarios RCP2.6, RCP4.5 and RCP8.5. Thick solid lines represent decadal means, shadings represent one standard deviation of decadal means. Thin lines show individual yearly means.

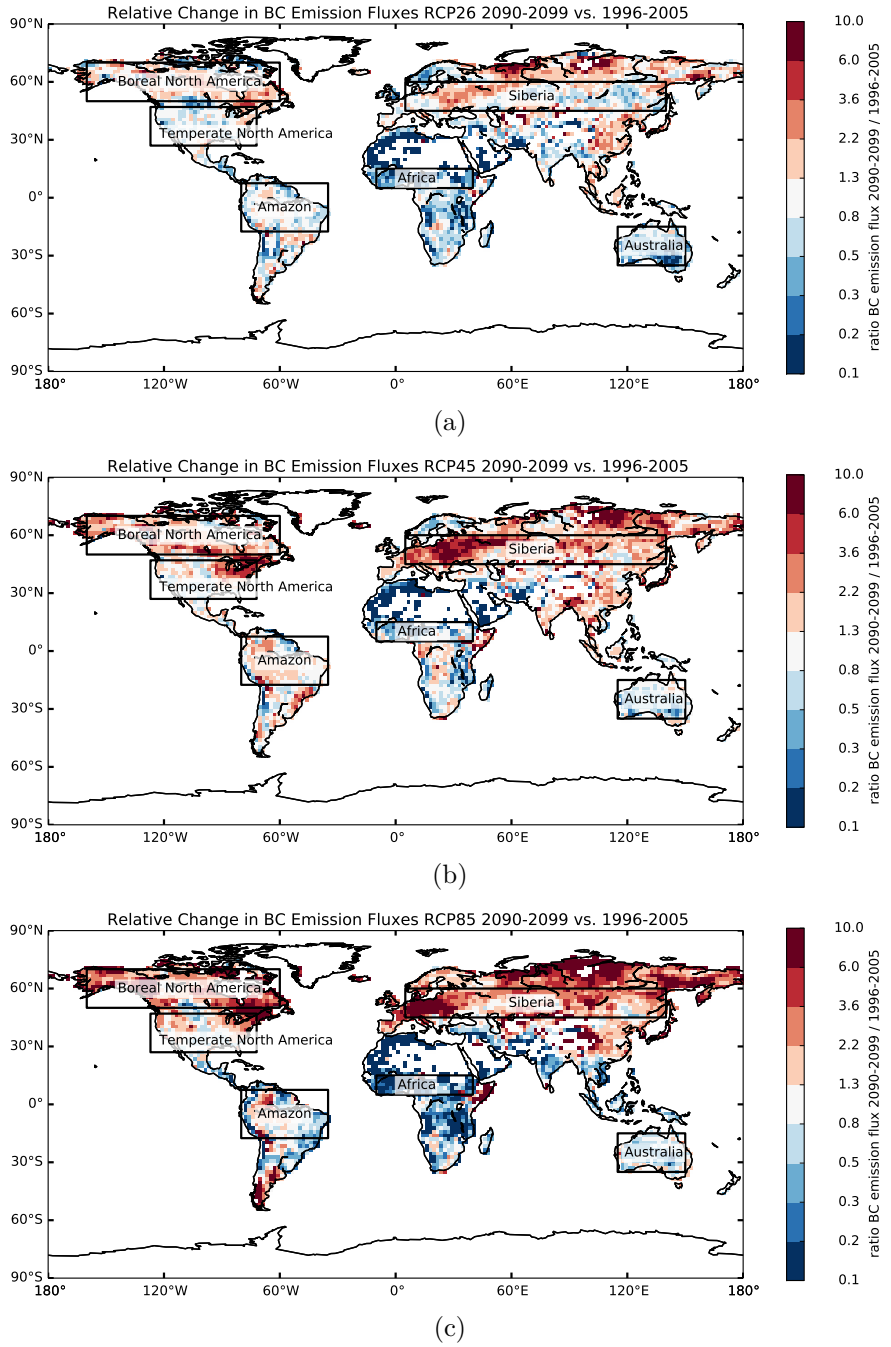

Figure 4.5: Relative changes in BC emission fluxes simulated by JSBACH-SPITFIRE for RCP2.6 (a), RCP4.5 (b) and RCP8.5 (c) for 2090–2099. All plots show relative differences to present day (PD) climate conditions (1996–2005). Red colors indicate an increase in emission fluxes, blue colors indicate a decrease in emission fluxes compared to PD. Black rectangles represent region classifications discussed in Sect. 4.3.4.

Table 4.4: Mean tropical and extra-tropical wildfire emission fluxes for the emission species BC, OC and SO_2. The tropics represent 24.375° N to 24.375° S. All emission fluxes shown in this table describe emission fluxes simulated by JSBACH-SPITFIRE. For the ECHAM6-HAM2 simulations, these emission fluxes are multiplied by the 3.4 correction factor described in Kaiser et al. (2012). Uncertainty estimates represent one standard deviation of annual means.

Simulation	**PD-SPITFIRE**	**RCP2.6-SPITFIRE**	**RCP4.5-SPITFIRE**	**RCP8.5-SPITFIRE**
Tropics BC [$\mathrm{Tg\,yr^{-1}}$]	1.11±0.11	0.78±0.09	0.95±0.08	0.70±0.10
NH Extra-tropics BC [$\mathrm{Tg\,yr^{-1}}$]	0.76±0.12	0.82±0.11	1.09±0.15	1.25±0.15
SH Extra-tropics BC [$\mathrm{Tg\,yr^{-1}}$]	0.32±0.05	0.26±0.03	0.35±0.04	0.36±0.05
Tropics OC [$\mathrm{Tg\,yr^{-1}}$]	9.87±0.97	7.05±0.87	8.24±0.70	6.77±0.93
NH Extra-tropics OC [$\mathrm{Tg\,yr^{-1}}$]	8.05±1.33	8.70±1.24	11.97±1.70	13.68±1.67
SH Extra-tropics OC [$\mathrm{Tg\,yr^{-1}}$]	2.72±0.45	2.21±0.32	2.96±0.39	3.55±0.51
Tropics SO_2 [$\mathrm{Tg\,yr^{-1}}$]	0.93±0.09	0.64±0.08	0.87±0.07	0.45±0.06
NH Extra-tropics SO_2 [$\mathrm{Tg\,yr^{-1}}$]	0.64±0.09	0.71±0.09	1.12±0.15	1.18±0.13
SH Extra-tropics SO_2 [$\mathrm{Tg\,yr^{-1}}$]	0.24±0.04	0.19±0.02	0.28±0.03	0.25±0.03

Table 4.4 provides a quantitative summary of mean annual tropical and extra-tropical wildfire emission fluxes for all RCP scenarios and emission species. The decrease in tropical wildfire BC emission fluxes ranges from -14 % for RCP4.5 to -37 % for RCP8.5. In contrast, extra-tropical wildfire emissions stay nearly constant for RCP2.6, while they are increased by +32 % for RCP4.5 and +49 % for RCP8.5, with only negligible differences between emission species. Due to the fact that the FRP is proportional to the biomass burned and thus to the emissions released by a fire, all changes discussed for wildfire emissions similarly apply to changes in FRP.

Besides the mean annual changes, also the seasonal cycle in wildfire emission fluxes is of importance for the atmospheric long-range transport. Figure 4.6 and Fig. 4.7 illustrate mean zonal daily relative and absolute changes in BC emission fluxes. Mid-latitude and boreal fire seasons are simulated to largely expand by up to 1–3 months for RCP8.5. Furthermore, fire activity significantly tends to shift north in the Northern Hemisphere and south in the Southern Hemisphere for RCP8.5. The absolute increase in the mid-latitude and boreal BC emission fluxes, which roughly compensates the decrease in the tropical emission fluxes, indicates that the relative importance of extra-tropical wildfires compared to tropical wildfires might be significantly enhanced in the future. In addition to the analysis of the changes in emission fluxes, Fig. 4.8 shows the FRP- and number-of-fires-spectrum simulated for all RCP scenarios compared to PD-SPITFIRE. For RCP2.6, FRP and the number of fires slightly decrease, while little change is observable for RCP4.5. For RCP8.5, the fraction of intense fires with FRP > 1000 MW is moderately increased compared to PD conditions. In contrast, the fraction of low FRP fires slightly decreases.

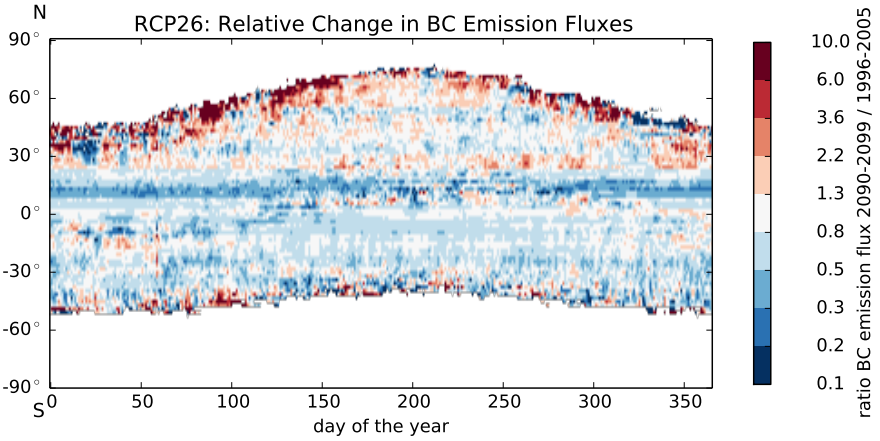

(a)

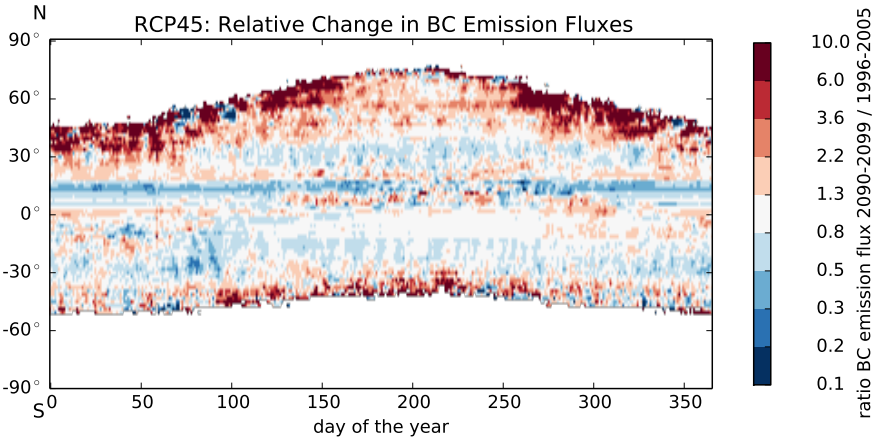

(b)

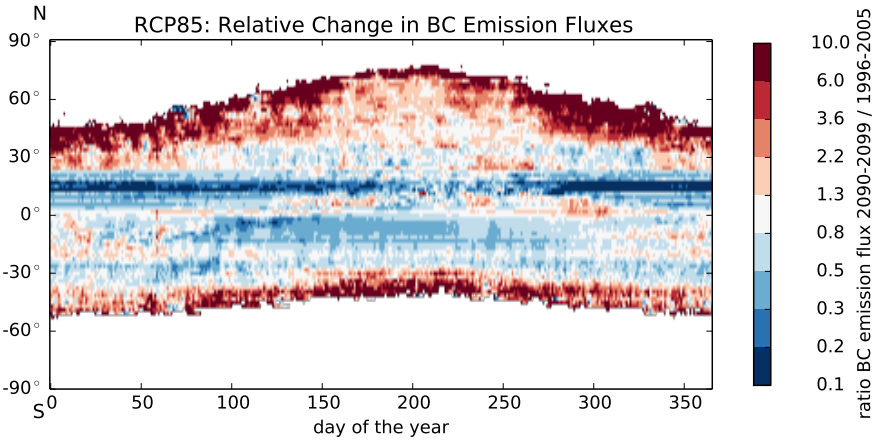

(c)

Figure 4.6: Seasonal cycle of zonal mean relative changes in BC emission fluxes simulated by JSBACH-SPITFIRE for RCP2.6 (a), RCP4.5 (b) and RCP8.5 (c) for 2090–2099. All plots show relative differences to present day (PD) climate conditions (1996–2005).

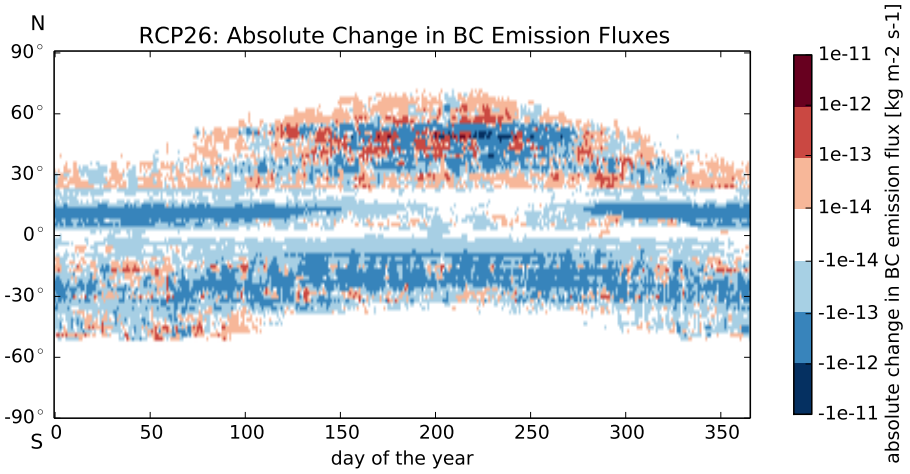

(a)

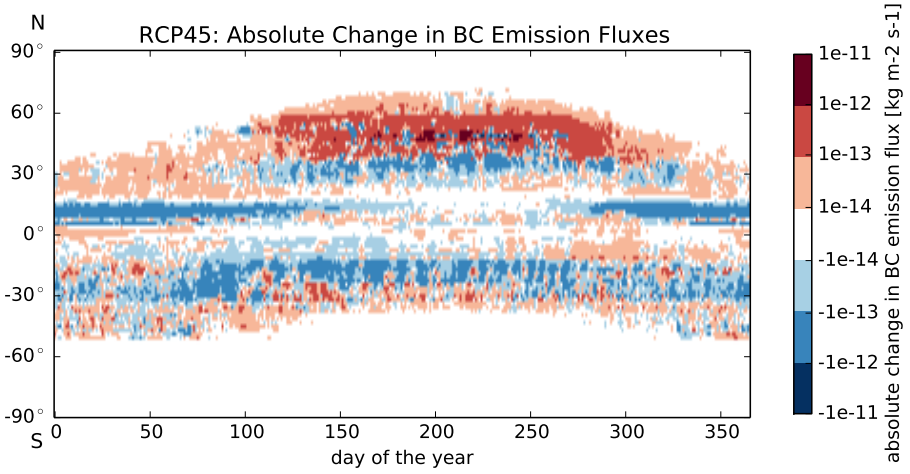

(b)

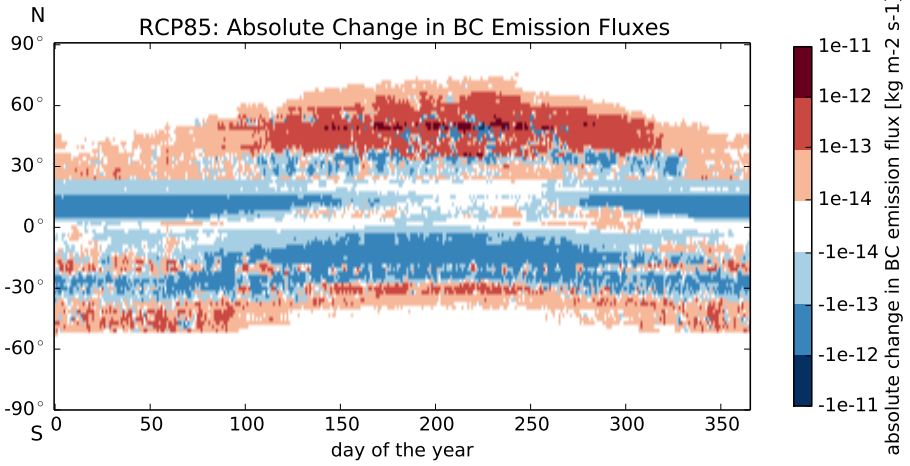

(c)

Figure 4.7: Seasonal cycle of simulated zonal mean absolute changes in BC emission fluxes simulated by JSBACH-SPITFIRE for RCP2.6 (a), RCP4.5 (b) and RCP8.5 (c) for 2090–2099 vs. present day (PD) conditions (1996–2005).

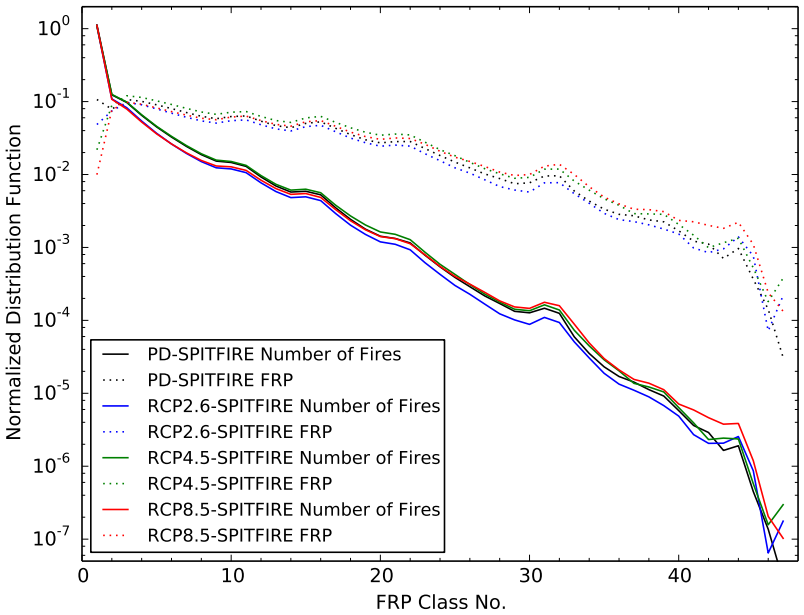

Figure 4.8: Global mean attribution of normalized FRP and number of fire distributions to FRP classes. Blue, green and red lines represent JSBACH-SPITFIRE distributions for the RCP scenarios 2.6, 4.5 and 8.5 (years 2090–2099), black lines represent JSBACH-SPITFIRE distributions for PD climate conditions (1996–2005).

4.3.4 Potential drivers of future changes in fire activity

Although it is not possible to fully disentangle all individual parameters which impact fire activity in our set of simulations, we analyze four region-specific basic drivers of changes in fire activity: human ignitions, fuel available for burning, fire danger index (FDI) and precipitation. These quantities are analyzed in six regions of distinct changes in emission fluxes (see Fig. 4.5) by calculating Pearson correlation coefficients between changes in specific parameters and the changes in emission fluxes. In summary, the strongest correlations can be found between fire emission fluxes and increased precipitation and fuel availability in North America and Siberia. In Africa, a strong decrease in human ignitions due to an increase in population density and land-use change represents the driving force for the strong decrease in fire activity. Scenario RCP8.5 shows the largest and most significant correlations, whereas for scenario RCP2.6 and scenario RCP4.5 statistically significant drivers of changes in fire activity could only be found for boreal North America and Africa. The results of our analysis are described in more detail for all regions in Appendix A.2.

4.3.5 Emission heights

While substantial differences in emission fluxes, meteorology and FRP exist between the RCP scenarios, mean top plume heights in all our simulations show little variation. Between simulation RCP2.6-SPITFIRE featuring the lowest mean plume height (1353 ± 428 m) and PD-SPITFIRE (1640 ± 560 m) featuring the highest mean plume

height, a difference of only 300 m is simulated. Figure 4.9 provides globally averaged plume height distributions for all simulations.

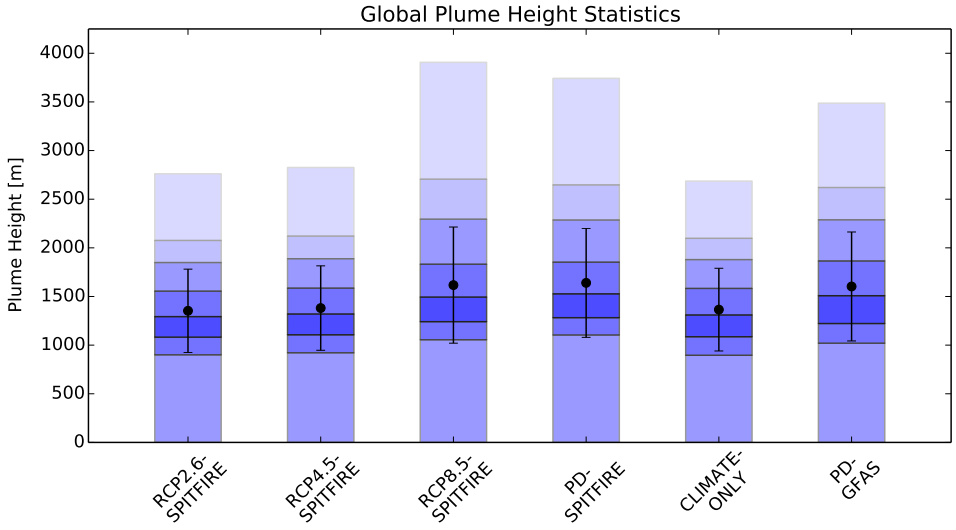

Figure 4.9: Global plume height statistics for all RCP-SPITFIRE experiments (2090–2099), simulation PD-SPITFIRE (1996–2005), simulation CLIMATE-ONLY (2090–2099) and PD-GFAS (2003–2011). Bluish bars represent 10^{th}, 25^{th}, 50^{th}, 75^{th}, 90^{th}, 95^{th} and 99^{th} percentiles.

Simulation CLIMATE-ONLY represents an RCP8.5 scenario for which wildfire emissions and FRP are kept identical to PD-SPITFIRE, but the meteorology is similar to RCP8.5-SPITFIRE. The largest differences between these simulations are observed for the 99^{th} plume height percentile. Simulation PD-SPITFIRE (3742 m) lies approximately 1.1 km above CLIMATE-ONLY (2686 m) indicating that, globally, climate warming entails more stable lower tropospheric conditions which tend to dampen plume heights. Due to the fixed fire locations and FRP, global changes in plume heights between simulations PD-SPITFIRE and CLIMATE-ONLY can only be attributed to decreased PBL heights and increased Brunt-Väisälä frequencies (see equation 4.2). As no significant changes in Brunt-Väisälä frequencies could be detected (not shown), the observed reduction in plume heights is primarily introduced by an average reduction in PBL heights due to decreased lapse-rates. A general decrease in atmospheric lapse-rates in a warmer climate and a reduction of PBL heights over land (particularly in the summer season) has also been indicated by several previous studies (e.g. Joshi et al., 2007; Penrod et al., 2014).

The comparison of simulation CLIMATE-ONLY to simulation RCP8.5-SPITFIRE enables us to disentangle the effects of climate change versus changes in emission fluxes and FRP on plume heights. With simulation RCP8.5-SPITFIRE showing the highest (3907 m) and CLIMATE-ONLY showing the lowest 99^{th} plume height percentile value (2686 m), we conclude that the increase in FRP overcompensates the climate effect on plume heights for the RCP8.5 scenario and therefore leads to larger plume heights, if both effects are considered. Note that all mean plume heights represent FRP-weighted daily mean plume height values, i.e. fires with high FRP values contribute disproportionately larger to the overall mean. We apply this weighting function to take into account the importance of emission fluxes which linearly scale with FRP (see Sect. 4.2.1).

Besides global statistics, the spatial plume height patterns of particularly deep emission injection events are of interest especially for air quality, long-range transport and removal processes. Figure 4.10 shows global maps of individual maximum plume heights in the period 2090–2099 for the RCP-SPITFIRE experiments. In addition, Fig. 4.11 illustrates the global distribution of maximum plume heights for simulation PD-SPITFIRE, simulation CLIMATE-ONLY and simulation PD-GFAS.

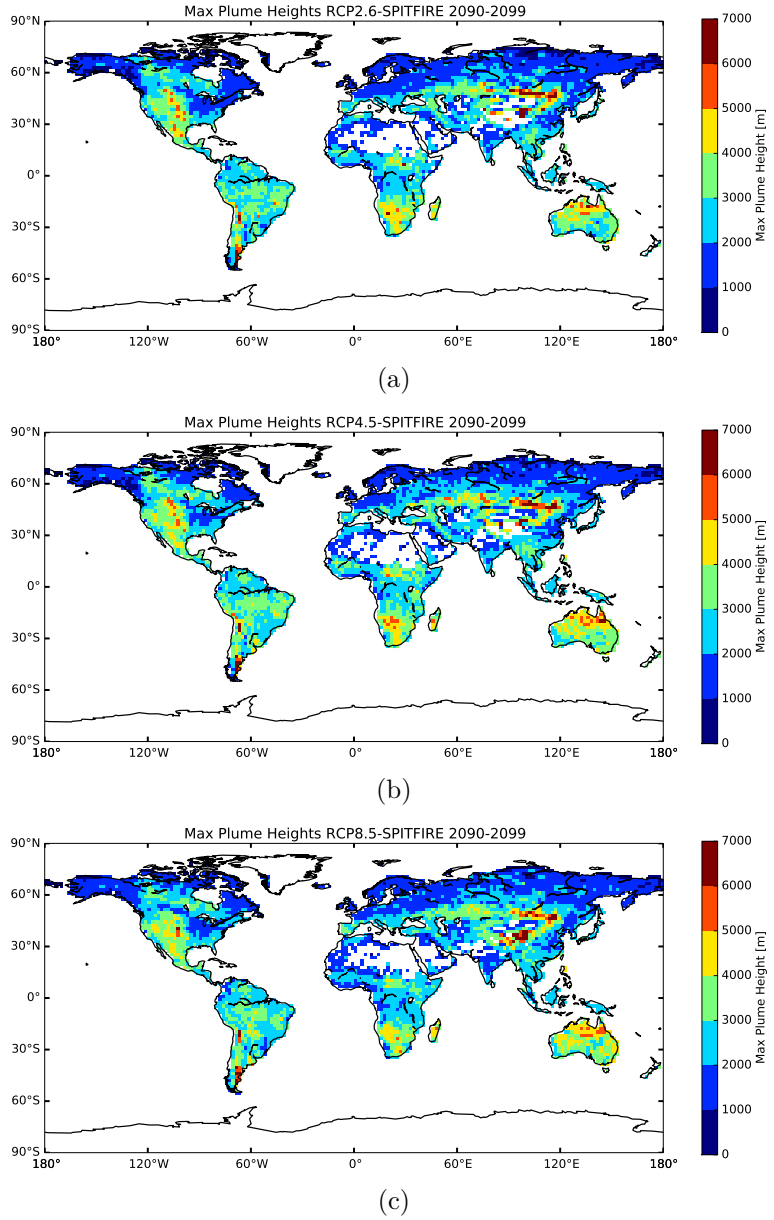

(a)

(b)

(c)

Figure 4.10: Maximum plume heights of individual fires for RCP2.6-SPITFIRE (a), RCP4.5-SPITFIRE (b) and RCP8.5-SPITFIRE (c) for 2090–2099.

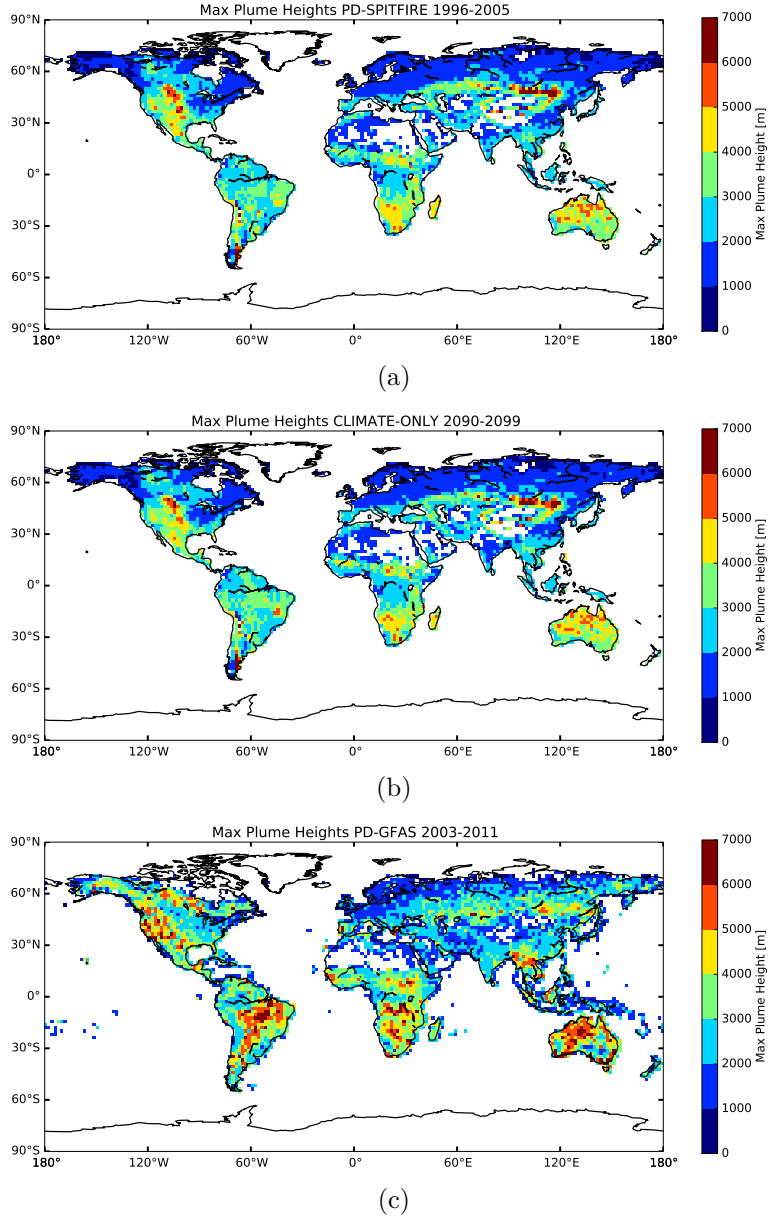

(a)

(b)

(c)

Figure 4.11: Maximum plume heights of individual fires for simulation PD-SPITFIRE (a), simulation CLIMATE-ONLY (b) and simulation PD-GFAS (c).

The general global patterns are fairly similar for all six simulations. The increased fire activity in boreal latitudes for simulation RCP4.5-SPITFIRE and RCP8.5-SPITFIRE compared to PD-SPITFIRE causes a slight expansion of maximum plume height >2km to the north which is not observable for simulation RCP2.6. This northward shift of deep plumes is mainly driven by increased FRP values in these regions. In contrast, plume heights in the Sahel zone are decreased in simulation RCP8.5-SPITFIRE, due to a sharp decline in FRP.

The less intense tropical fire activity for the RCP-SPITFIRE scenarios compared to PD conditions is also represented by lower maximum plume heights in central Africa and Northern Australia. Global plume height patterns in simulation CLIMATE-ONLY are very similar to simulation PD-SPITFIRE, but a moderate decrease in tropical plume heights is observable due to more stable atmospheric conditions in the RCP8.5 climate state. The comparison of simulation PD-SPITFIRE to PD-GFAS qualitatively demonstrates the limitations of the model to simulate regional plume height patterns due to biases in fire activity patterns. Although the global mean plume height statistics show very good agreement for both simulations, the model largely underestimates maximum individual plume heights in Alaska, Northern Siberia, South America and Australia. Reasonable agreement is achieved for Africa, Europe and Central Asia. The underestimation of emission fluxes and plume heights in boreal latitudes is presumably related to a poor representation of favorable fire conditions which cause too low FRP values.

4.3.6 Black carbon concentration profiles

BC concentrations throughout the troposphere are determined by emission fluxes as well as vertical and horizontal transport and removal processes. Figure 4.12 and Fig. 4.13 show relative differences of mean zonal BC profiles for all simulations shown in Table 4.3. Lower tropospheric BC concentrations (below 500 hPa) are in all cases vastly correlated to the regional changes in emission fluxes (see Fig. 4.7). On the other hand, simulation RCP8.5-SPITFIRE clearly demonstrates that upper tropospheric and lower stratospheric BC concentrations are mainly dominated by tropical emission fluxes, because differences in plume heights are negligible and upper tropospheric extra-tropical BC concentrations decrease even though local emission fluxes are increased (Fig. 4.12c). These findings are consistent with similar aerosol transport mechanisms identified for present day climate conditions (see Sect. 3.3.2).

Figure 4.13a illustrates that tropical deep convection is generally decreased for RCP8.5 climate conditions leading to a decrease in upper tropospheric BC concentrations by 10-50 %, if wildfire emissions are kept constant at PD levels. The impact of changes in emission heights is expected to be small, because in the tropics BC concentrations show a moderate increase between 600 hPa and the surface even though emission heights are decreased in these regions compared to PD conditions. The comparison of simulation RCP8.5-SPITFIRE (Fig. 4.12c) and simulation RCP8.5-SPITFIRE+AMCCMIP-2090 (Fig. 4.13b) indicates that changes in wildfire emissions are of similar importance as the projected reduction (-53 %) in BC emissions from anthropogenic sources.

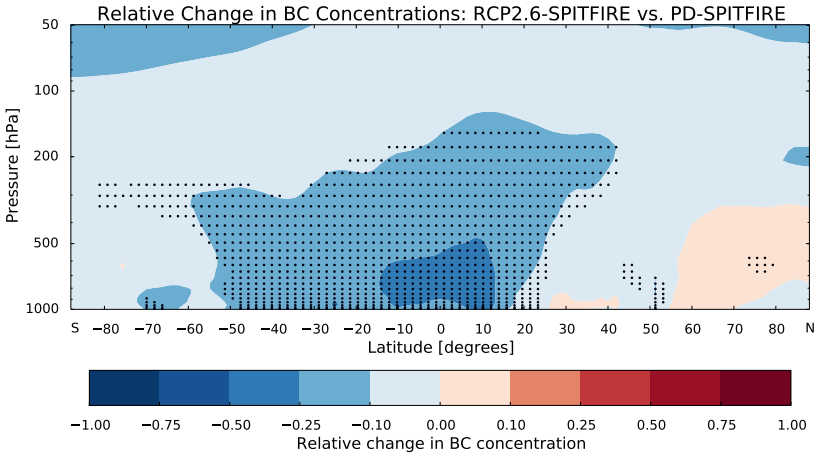

(a)

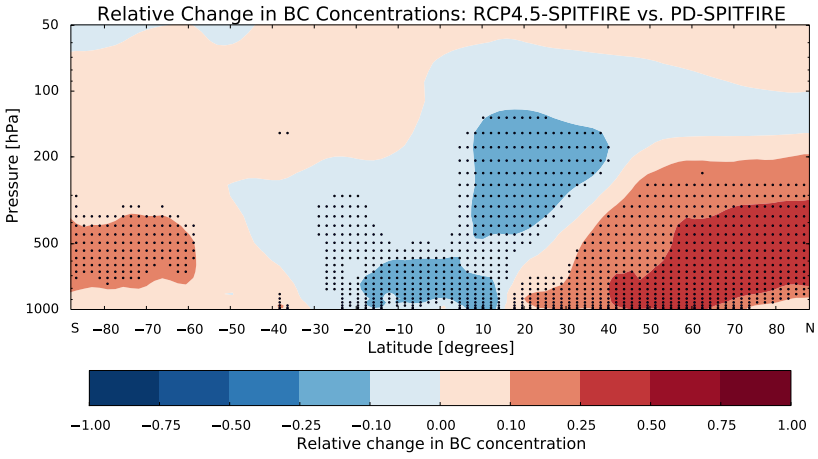

(b)

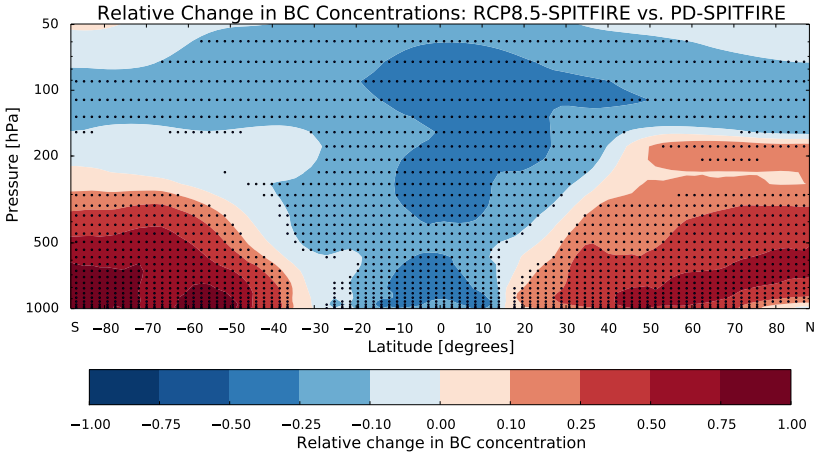

(c)

Figure 4.12: Relative change in mean zonal BC concentrations for simulation RCP2.6-SPITFIRE (a), RCP4.5-SPITFIRE (b) and RCP8.5-SPITFIRE (c) for 2090–2099; reference simulation is PD-SPITFIRE 1996–2005. Black dots indicate significance based on a student-t-test at a 95 % confidence interval.

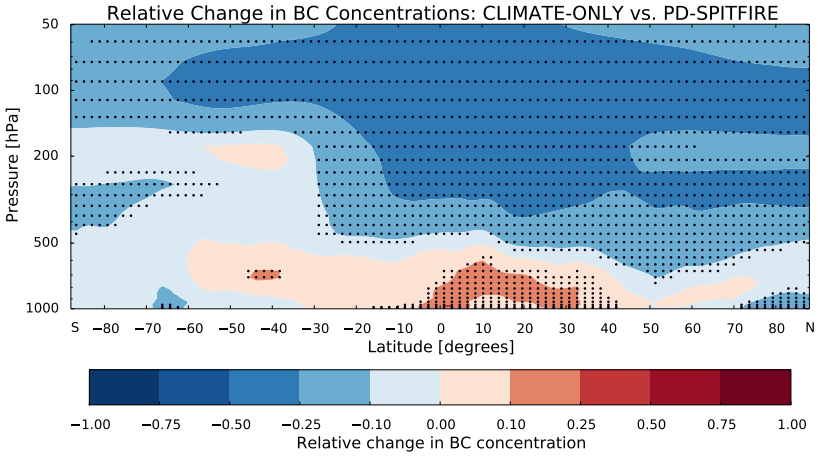

(a)

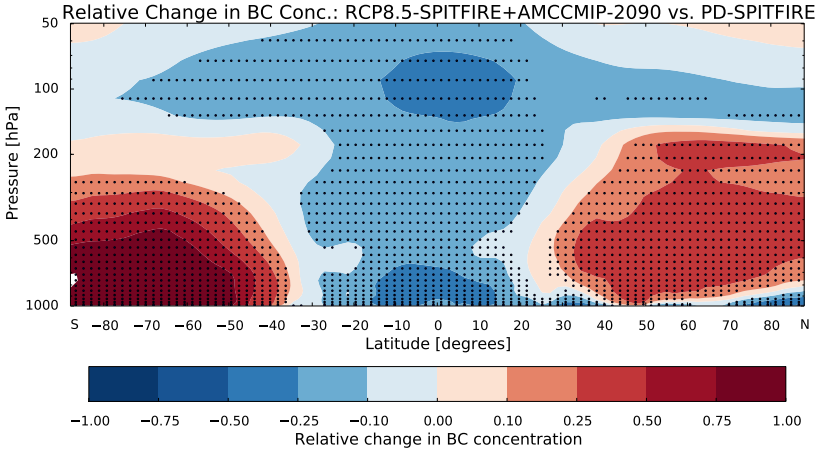

(b)

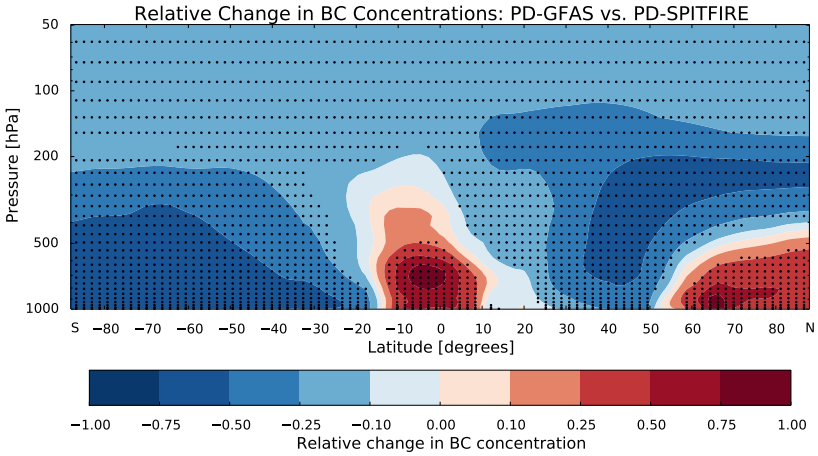

(c)

Figure 4.13: Relative change in mean zonal BC concentrations for simulation CLIMATE-ONLY (a), RCP8.5-SPITFIRE+ACCMIP-2090 (b) and simulation PD-GFAS (c); reference simulation is PD-SPITFIRE 1996–2005. Black dots indicate significance based on a student-t-test at a 95 % confidence interval.

The comparison of simulation PD-GFAS and simulation PD-SPITFIRE (see Fig. 4.13c) provides an estimate, how the differences between a satellite-based emission inventory and the interactively simulated wildfire emissions from JSBACH-SPITFIRE impact atmospheric BC concentrations. While the total global emission fluxes differ by only 5 % for present day climate conditions (see Sect. 4.3.1), strong regional deviations in atmospheric BC concentrations occur. These regional differences in BC concentrations between simulation PD-SPITFIRE and PD-GFAS show a similar magnitude as the changes from present day climate conditions to the future RCP climate scenarios. In Sect. 3.3.2 of this thesis, however, we found comparable regional differences in BC concentrations of up to 50 % between GFAS and AEROCOM (based on GFEDv2) emission inventories, which are both satellite-based. Therefore the presented differences in BC concentrations, which emerge from the choice of the wildfire emission inventory, do not represent model biases in a strict sense, but only provide a rough idea about the uncertainties introduced by the choice of the emission inventory.

Besides BC concentration profiles, BC removal rates in the polar regions might represent a relevant parameter for the overall fire-climate impact, because BC deposition on snow decreases the albedo leading to enhanced melting. A summary of mean annual BC deposition rates is provided in Table 4.5. Overall changes in future Arctic deposition rates compared to PD-SPITFIRE are small for scenario RCP2.6-SPITFIRE, while a strong increase in BC deposition up to 53 % is simulated for RCP8.5-SPITFIRE due to a strong increase in boreal wildfire activity. The comparison of simulation RCP8.5-SPITFIRE to RCP8.5-SPITFIRE+ACCMIP-2090 illustrates that Arctic deposition rates in the RCP8.5 scenarios are largely determined by BC emissions from wildfires, not by anthropogenic emission which are approximately cut by half in the scenario RCP8.5-SPITFIRE+ACCMIP-2090.

Table 4.5: Total removal rates represent the sum of wet and dry deposition and sedimentation. Polar regions represent 67° N - 90° N and 67° S to 90° S, respectively. Uncertainty estimates represent one standard deviation of annual means.

Simulation	RCP2.6-SPITFIRE	RCP4.5-SPITFIRE	RCP8.5-SPITFIRE	PD-SPITFIRE	CLIMATE-ONLY	RCP8.5-SPITFIRE+ACCMIP-2090	PD-GFAS
Global removal rates [mg m-2 y-1]	22.63±0.42	26.15±0.51	25.68±0.89	24.81±0.62	24.81±0.62	20.32±0.86	22.70±3.95
NH Polar removal rates [mg m-2 y-1]	5.35±0.53	7.21±0.80	8.09±0.93	5.29±0.60	5.85±0.40	7.32±0.74	6.13±1.67
SH Polar removal rates [mg m-2 y-1]	0.39±0.06	0.47±0.05	0.65±0.08	0.44±0.04	0.46±0.05	0.67±0.07	0.23±0.07

4.3.7 Aerosol optical thickness

The simulated future changes in AOT at 550 nm are caused by combined changes in aerosol emission fluxes and by changes in atmospheric aerosol processing via transport and aerosol-cloud interactions. Table 4.6 provides AOT values as global, tropical and Northern Hemisphere (NH) and Southern Hemisphere (SH) extra-tropical means for all ECHAM6-HAM2 experiments. While only moderate changes in global AOT are simulated for RCP2.6 (0.131±0.002) and RCP4.5 (0.139±0.003) compared to PD-SPITFIRE (0.134±0.002), a considerably stronger increase in AOT is modelled for RCP8.5 (0.151±0.004).

As dust, sea salt and DMS emission fluxes in ECHAM6-HAM2 are calculated interactively and depend on the specific atmospheric conditions, only the comparison of simulation CLIMATE-ONLY to RCP8.5-SPITFIRE enables us to disentangle the particular impact of changes in wildfire emissions from other emission sources. Globally, the significant increase in AOT for simulation CLIMATE-ONLY compared to PD-SPITFIRE of +10.4±1.1 % can be assigned to the increase in atmospheric dust, sea salt and DMS burdens of +13.6±5.2%, +7.1±0.8 % and +23.2±0.6 %, respectively (see Appendix A.3 for spatial patterns). The differences in AOT between simulation CLIMATE-ONLY and simulation RCP8.5-SPITFIRE can be attributed to changes in wildfire emissions alone. In the extra-tropical NH, the wildfire-induced increase in AOT for simulation RCP8.5-SPITFIRE (+0.021±0.002) compared to PD-SPITFIRE is about two times larger than the climate change induced reduction in AOT in simulation CLIMATE-ONLY (-0.010±0.001).

Moreover, the modeled total increase in extra-tropical NH AOT due to changes in wildfire activity is comparable to the counteracting projected decrease in AOT in the order of -0.030 caused by a decrease in anthropogenic BC emissions (see Table 4.6, RCP8.5-SPITFIRE+ACCMIP-2090). In the tropics, however, the reduction of tropical wildfire emissions in simulation RCP8.5-SPITFIRE compared to simulation CLIMATE-ONLY slightly decreases the mean AOT by -0.005±0.003.

Table 4.6: Mean AOT values for 2090–2099 (all RCP simulations) and 1996–2005 (simulation PD-SPITFIRE) as well as 2003–2011 (PD-GFAS). Uncertainty estimates represent one standard deviation of annual mean AOT values.

Simulation	RCP2.6-SPITFIRE	RCP4.5-SPITFIRE	RCP8.5-SPITFIRE	PD-SPITFIRE	CLIMATE-ONLY	RCP8.5-SPITFIRE+ACCMIP-2090	PD-GFAS
Global mean AOT	0.131±0.002	0.139±0.003	0.151±0.004	0.134±0.002	0.148±0.004	0.136±0.002	0.131±0.006
Tropics mean AOT	0.156±0.004	0.164±0.005	0.179±0.006	0.162±0.003	0.184±0.008	0.165±0.004	0.167±0.009
Extropics NH mean AOT	0.124±0.003	0.136±0.004	0.147±0.005	0.126±0.004	0.116±0.002	0.117±0.004	0.115±0.009
Extropics SH mean AOT	0.104±0.002	0.108±0.002	0.116±0.003	0.104±0.001	0.130±0.004	0.116±0.002	0.098±0.002

In addition to the globally and zonally averaged AOT values presented in Table 4.6, Fig. 4.14 and Fig. 4.15 provide global maps of relative changes in AOT and BC burdens for the simulations CLIMATE-ONLY vs. PD-SPITFIRE and RCP8.5-SPITFIRE vs. PD-SPITFIRE to allow for region-specific analysis of the simulated changes in AOT. In large parts of North America, Asia and sub-Saharan Africa, distinct changes in BC burdens of -50 % to +100 % correspond to AOT changes of similar magnitude for simulation RCP8.5-SPITFIRE (see Fig. 4.14b and Fig. 4.15b, respectively), whereas these regional changes in BC burden and AOT are less pronounced or nonexistent in simulation CLIMATE-ONLY (see Fig. 4.14a and Fig. 4.15a, respectively). Therefore, the simulated changes in wildfire emissions can be identified to represent the major drivers of changes in AOT in these regions of strong wildfire activity. Other region-specific patterns such as the strong relative increase in AOT around Antarctica and a moderate increase in AOT over large parts of the tropical oceans, are similarly observable in simulation CLIMATE-ONLY and RCP8.5-SPITFIRE. In these regions the BC burdens do not hold comparable changes and therefore we conclude that changes in AOT in the polar regions and over the tropical oceans are not primarily caused by changes in wildfire activity, but by changes in dust, sea salt and DMS emission fluxes (see also Appendix A.3).

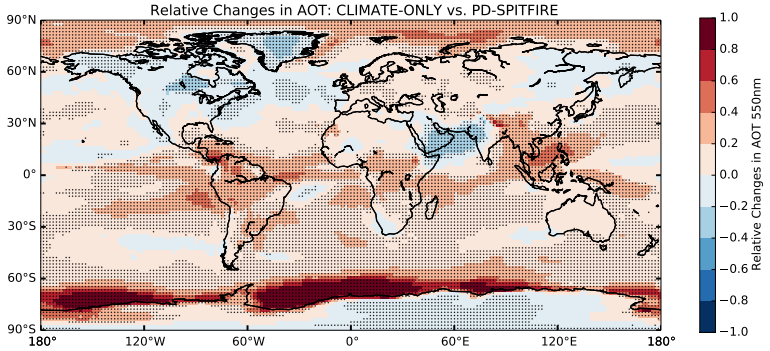

(a)

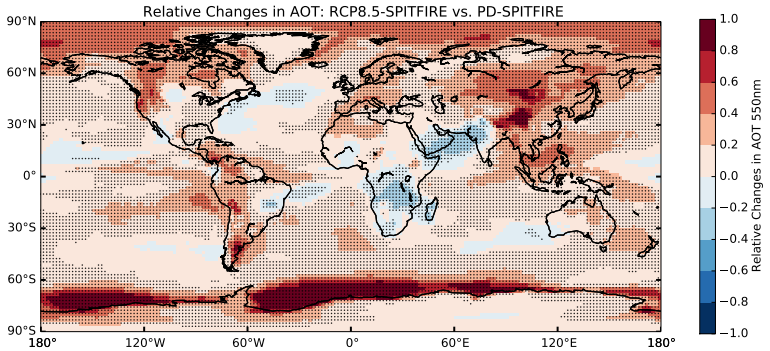

(b)

Figure 4.14: Relative changes in AOT at 550nm for simulations CLIMATE-ONLY (a) and RCP8.5-SPITFIRE (b) both representing the time period 2090–2099 compared to the reference simulation PD-SPITFIRE (1996–2005). Black dots indicate significance based on a student-t-test 95 % confidence interval.

Overall, the changes in wildfire emissions can be identified to represent the major driver in AOT changes only in the vicinity of those regions featuring strong wildfire activity. It is uncertain, whether a similar AOT impact of changes in wildfire emissions and climate conditions is applicable to the scenarios RCP2.6 and RCP4.5. For a more detailed analysis, further simulations with RCP2.6 and RCP4.5 climate conditions and fixed PD wildfire emissions would be required. But due to the high computational costs, they could not be carried out in the framework of this study.

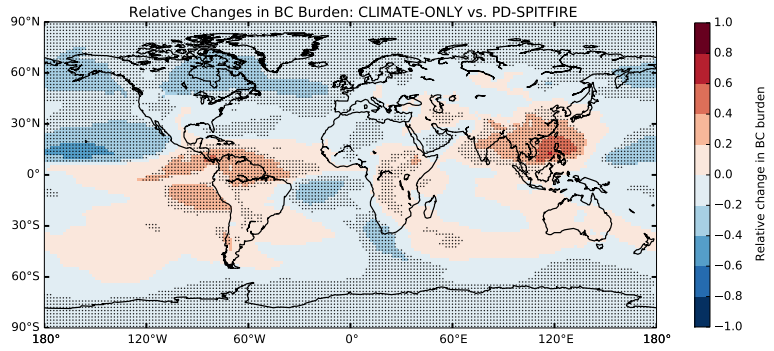

(a)

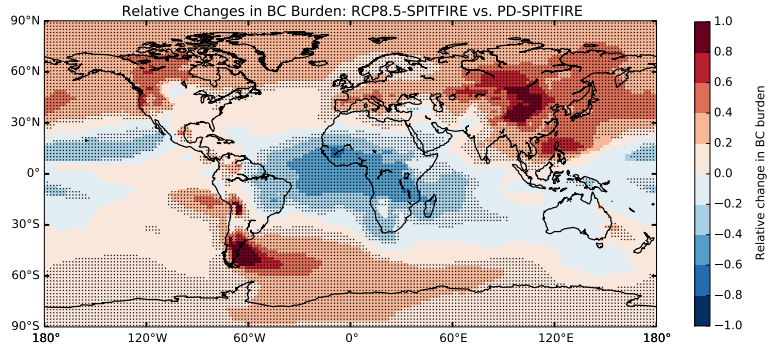

(b)

Figure 4.15: Relative changes in BC burden for simulations CLIMATE-ONLY (a) and RCP8.5-SPITFIRE (b) both representing the time period 2090–2099 compared to the reference simulation PD-SPITFIRE (1996–2005). Black dots indicate significance based on a student-t-test at a 95 % confidence interval.

4.4 Summary and conclusions

In this chapter, the process-based global vegetation-fire model JSBACH-SPITFIRE (Lasslop et al., 2014) was used to simulate changes in wildfire emission fluxes and FRP during the 21st century. In our simulations we prescribed atmospheric conditions according to RCP scenarios of the MPI-ESM (Giorgetta et al., 2013), population density changes according to SSP scenarios described by van Vuuren and Carter (2014) and land-use changes from Hurtt et al. (2011). Wildfire emission fluxes and FRP simulated by JSBACH-SPITFIRE were employed to investigate the fate of the wildfire aerosol emissions in the

atmosphere using the aerosol-climate model ECHAM6-HAM2 for the period 2090–2099 (Stier et al., 2005; Zhang et al., 2012a).

The emission release into the atmosphere in ECHAM6-HAM2 was implemented by a semi-empirical plume height parametrization. Based on FRP from JSBACH-SPITFIRE and atmospheric stability parameters from ECHAM6-HAM2, the parametrization simulates plume heights of individual fires (Sofiev et al., 2012).

The combined set of JSBACH-SPITFIRE and ECHAM6-HAM2 model simulations enabled us to quantify not only the projected future changes in wildfire emission fluxes, but also to assess the impact of changes in emission heights and emission fluxes on atmospheric BC concentrations and AOT. The major findings of this study can be summarized as follows:

- The complex interactions of changes in climate conditions, population density and land-use within the 21st century result in diverse, region-specific changes in future wildfire activity. While extra-tropical fire emissions stay nearly constant for the RCP2.6 scenario in 2090-2099 compared to present day, substantial enhancements in extra-tropical emission fluxes of +32 % and +48 % are simulated for RCP4.5 and RCP8.5. The length of the boreal and temperate fire seasons is enlarged by 1–3 months on average. In the tropics, wildfire emissions are decreased by -14 to -37 % for all RCP scenarios.

- Compared to present day conditions, a future increase in atmospheric stability generally tends to dampen the mean plume heights by about -0.3 km and the 99th percentile by approximately -1.1 km for RCP8.5. An increase of similar magnitude in the mean plume heights and in the 99th percentile of +0.3 km and +1.2 km is introduced by a significant intensification of strong fires in RCP8.5. For RCP2.6 and RCP4.5, plume heights are reduced primarily due to the combined increase in atmospheric stability and decreased or constant fire intensities. Overall, we conclude that future changes in fire emission heights are of minor importance for future changes in BC long-range transport and the overall wildfire climate impact.

- Lower tropospheric BC concentrations basically demonstrate the response to the regional changes in wildfire emission fluxes. Upper tropospheric BC concentrations, however, are mainly determined by tropical convection with little influence of the emission heights.

- Our results for the RCP8.5 scenario demonstrate that the changes in wildfire emissions may largely compensate the projected reduction in anthropogenic BC emissions by the end of the 21st century.

- For the strongest warming scenario RCP8.5, a significant increase in AOT of +0.031±0.002 is introduced by the changes in wildfire emissions for the Northern Hemisphere extra-tropics. Globally, however, the mean increase in AOT is small (+0.003±0.002) because of the substantial decrease in tropical wildfire activity.

Although different in it's magnitude, a distinct increase in future boreal and mid-latitude wildfire activity and a decrease in tropical wildfire activity has been indicated by

a large number of previous studies (Flannigan et al., 2009, and references therein). Our results are basically in line with the general findings of those studies, but depending on the specific RCP scenario, the magnitude of changes in wildfire emission release shows large regional variations. Fire activity projections by Pechony and Shindell (2010) suggested that future fire activity might primarily be driven by temperature change rather than anthropogenic activities. For our JSBACH-SPITFIRE simulations only extra-tropical changes in fire activity are mainly driven by climate conditions whereas human activities prescribed in this study dominate the changes in tropical fire activity. The lengthening of the mid-latitude and boreal fire seasons by up to three months presented in this study and the increased spread of fires to northern latitudes show basic agreement to the studies by Spracklen et al. (2009), Moritz et al. (2012), de Groot et al. (2013) and Flannigan et al. (2013), which were based on more simplified fire modeling approaches.

To our knowledge no references of future FRP estimates have been provided by other studies and the use of FRP as a diagnostic parameter in JSBACH-SPITFIRE is a novel approach. However, de Groot et al. (2013) applied three GCMs (CGCM3.1, HadCM3 and IPSL-CM4) to simulate fire activity and fire line intensity in Canada and Siberia between 2091–2100. Overall, the fire line intensity of individual fires was expected to increase substantially in the future. An increase in FRP in these regions is similarly projected in our simulations, but globally, only a weak shift towards more intense fires is found even for the RCP8.5 scenario.

The simulated future regional changes in boreal and mid-latitude AOT due to changes in wildfire emissions show a magnitude which is similar to results presented by Ward et al. (2012). But due to the differences in fire model representations, population density projections and atmospheric conditions, the results of this study are only in line with the extra-tropical increase in AOT, not with the strong tropical increase in AOT shown by Ward et al. (2012). These results indicate that the response of fire activity to global warming emerges to be more uncertain in the tropics than in the extra-tropics.

In the vicinity of the major wildfire activity regions, wildfire-induced positive and negative changes in AOT of up to 50–100 % are substantial. Previous studies have shown that regional changes in wildfire aerosol concentrations of this magnitude can lead to a local suppression or intensification of convective precipitation (e.g. Andreae et al., 2004; Grell et al., 2011) and can even impact atmospheric large-scale systems like the Hadley circulation (Tosca et al., 2013). A more detailed assessment of the expected future wildfire aerosol-cloud interactions and their impact on large-scale circulation is desirable, but would require a fully coupled land-ocean-atmosphere-aerosol model which was not yet available at the time of the present study.

With the next generation of Earth system models, fully coupled high resolution simulations will potentially provide more appropriate settings to study local vegetation-wildfire-aerosol-cloud interactions and potential feedbacks. The methodological approaches applied in this study, which link vegetation-modeling, emission heights and aerosol-climate modeling, may help to step forward towards a more accurate assessment of the future interactions between wildfires and climate.

Chapter 5

Conclusions

5.1 Summary

The combined discussion of the three individual chapters 2, 3 and 4 enables a detailed assessment of the research questions raised in chapter 1.3:

I) Which degree of plume height parametrization complexity is required to adequately represent wildfire emission heights in state-of-the-art global climate models?

The implementation of a semi-empirical plume height parametrization (Sofiev et al., 2012) enables a reasonable simulation of regional heterogeneities in global plume height patterns compared to observations. Although the prediction skills for individual plumes remain uncertain, the variables FRP (satellite-based), Brunt-Väisälä frequency and PBL height (both simulated by the model) applied in the parametrization are basically sufficient to calculate realistic global plume height distributions. The introduction of a diurnal cycle and the compensation of the underestimation of high FRP values due to smoke opacity effects enables an accurate simulation of deep emission injections above 4 km which is not accounted for in the original parametrization by Sofiev et al. (2012). Compared to the application of prescribed standard emission heights in ECHAM6-HAM2, which do not take into account fire intensity and atmospheric stability, the modified Sofiev parametrization represents a significant improvement in the representation of fire emission heights in ECHAM6-HAM2. A computationally more expensive, fully analytical model (Freitas et al., 2007; Paugam et al., 2015) does not lead to improved plume height predictions. Hence, one can conclude that for coarse resolution climate modelling, empirically derived and computationally inexpensive parametrizations provide adequate plume height representations for global climate models.

II) How do wildfire emission heights impact global BC concentrations, BC deposition rates and atmospheric radiative transfer?

Although the representation of emission heights in ECHAM6-HAM2 could be substantially improved, the subsequent improvement in AOT model performance is found to be small and limited to the major biomass burning regions. The results presented in this study clearly show that global BC concentrations, BC deposition rates and atmospheric

radiative transfer are more sensitive to emission inventories than to the details of the emission height implementation. Upper tropospheric and lower stratospheric BC concentrations are mainly determined by tropical convection and regional emission release patterns rather than by the specific plume height parametrization applied. The differences in the total wildfire emission TOA RF between prescribed emission heights (at the surface / in the lower free troposphere) and parametrized emission heights range between 0.04 to 0.08 $\mathrm{W\,m^{-2}}$. For mean plume height differences of 1.1–2.5 km between prescribed and parametrized emission heights, BC deposition rates in the Arctic and Antarctica are altered by 5–25 %. These results imply that, on average, plume heights only have a limited impact on the BC-induced decrease in snow and ice albedo. Against the background of the large biases which are persistent in all state-of-the-art emission inventories, the emission height impact on global long-range transport and atmospheric radiative transfer can be identified to be small compared to the emission inventories.

III) How might future changes in fire emissions and fire emission heights in a warmer climate impact atmospheric BC concentrations and atmospheric radiative transfer?

Depending on the choice of the RCP scenario, a moderate to strong increase in Northern Hemisphere extra-tropical wildfire emission fluxes of about 8–64 % is found for the time period 2090–2099 compared to present day in the applied JSBACH-SPITFIRE simulations. The intensity of the increase in emission fluxes as well as a lengthening in the fire season scales with the magnitude of the extra-tropical warming. In the tropics, all RCP scenarios project a 14–37 % decrease in fire activity which is primarily driven by changes in human land-use and changes in climate. Changes in climate generally tend do decrease emission heights due to increased atmospheric stability. While these changes in atmospheric stability are dominant for the RCP2.6 and the RCP4.5 scenario, the effect is overcompensated by a substantial increase in fire intensity for the strongest warming scenario RCP8.5. Compared to the distinct changes in regional emission flux patterns, the changes in emission heights represent only a second-order effect for BC long-range transport and atmospheric radiative transfer. Overall, changes in wildfire BC emission fluxes have a similar strength as the projected decrease in anthropogenic BC emissions. Thus, for aerosol-climate modelling studies of future climate scenarios, the relative importance of wildfires emissions will substantially increase in the extra-tropics. The magnitude of changes in regional AOT of -20 to +80 % caused by changes in wildfire emission fluxes could potentially impact atmospheric circulation patterns and precipitation rates, but the layout of this study did not allow to investigate possible feedbacks due to a lack of coupling between land, ocean and atmosphere in the model setup.

5.2 Discussion

The results of this study should be discussed in the interdisciplinary context of our current scientific understanding of wildfire-climate interactions. With the recent implementation of the process-based fire model SPITFIRE in JSBACH (Lasslop et al., 2014) which is part of the MPI-ESM (Giorgetta et al., 2013; Stevens et al., 2013), the existing gaps in linking fire as a vegetation disturbance process with atmospheric processes are expected to narrow.

However, the results of this thesis demonstrate that the uncertainties in vegetation-fire as well as in aerosol modelling remain large. This is the case even if emission heights are parametrized more accurately in aerosol-climate models.

Compared to previous studies which prescribed emission heights at the surface or at fixed atmospheric levels (Dentener et al., 2006; Tosca et al., 2013), the modified implementation of the semi-empirical plume height parametrization by Sofiev et al. (2012) implies a substantial progress in the representation of the physical processes, which link the terrestrial biosphere and the atmosphere. The new fire intensity binning technique implemented in ECHAM6-HAM2 and the novel statistical-empirical FRP distribution scheme included in JSBACH-SPITFIRE offer a consistent framework to appropriately simulate the emission release of individual fires in ESMs. Although the results of this study show that emissions heights are of limited importance for coarse resolution modelling, the introduced methodological approaches may easily be applied in follow-up studies of higher resolution in the newly developed icosahedral non-hydrostatic (ICON) general circulation model. The quantification of the sensitivity of atmospheric BC transport and radiation to emission height implementations shown in this study provides a reference for future model inter-comparison studies.

However, related to the plume height parametrization used in this study, some major limitations apply:

- The applied Sofiev parametrization does not provide any information about the vertical distribution of the injected emissions, but only about top emission heights. As it has been shown by the sensitivity study presented in chapter 3, uncertainties in the vertical emission profiles alter BC transport and radiation by a magnitude that is comparable to emission height changes of 1-2 kilometers. A very limited number of vertical plume measurements was provided by Liu et al. (2013) and Archer-Nicholls et al. (2015), but extensive statistics for a broad range of emission profiles would be required to make considerable progress with regards to the representation of vertical emission distributions in global models.

- Rare events of emission injections into the lower stratosphere represent extreme phenomena where intense plume dynamics interact with fires and local topography and trigger the development of strong thunderstorms, sometimes even fire-induced tornados (Fromm et al., 2006; Peterson et al., 2015). The occurrence numbers and impacts of these events are uncertain and thus they are not accounted for in the applied model, even though they might be of importance for global atmospheric radiative transfer as several authors have demonstrated (Jost, 2004; Fromm et al., 2008, 2010).

- Plume height predictions in the Sofiev parametrization are only based on the parameters Brunt–Väisälä frequency, PBL height and FRP. Other atmospheric and fire-related processes like entrainment, wind drag or a multiple core structure of fires are known to impact the fire-induced convection and thus the emission heights (e.g. Freitas et al., 2010; Rio et al., 2010), but these parameters are only implicitly accounted for in the modified semi-empirical parametrization of Sofiev et al. (2012) which was applied in this study.

Even though the uncertainties in plume height predictions introduced by the limitations of the semi-empirical plume height parametrization are numerous, the results of this study indicate that the application of a more sophisticated plume model can not be expected to improve the plume height modelling results. Val Martin et al. (2012) and Ichoku et al. (2012) also stated that an improvement in individual plume height predictions would require substantially higher temporal and spatial resolution of land-surface, fire and atmospheric properties. For all current state-of-the-art plume models and parametrizations, no distinct differences in model performance could be found between the different plume models. In addition, a recent study by Archer-Nicholls et al. (2015) underlines these conclusions as even for higher resolution local WRF modeling, the widely used analytical PRM model (Freitas et al., 2007) vastly fails to reproduce realistic emission heights. Combined with the limited impact of changes in emission heights on atmospheric transport and radiation shown in this study, the hypothesis that ESMs would significantly benefit from implementations of sophisticated plume rise models (Paugam et al., 2015), can be rejected.

Compared to emission heights, wildfire emission inventories represent an even lager source of uncertainties. The simulations presented in this study were either directly based on the satellite-based emission inventories GFED and GFAS or on JSBACH-SPITFIRE emission estimates which were tuned against these observational estimates. Therefore the following major issues remain:

- All bottom-up emission inventories (including GFED and GFAS applied in this study) need to apply specific tuning factors in order to provide reasonably simulated AOT values in aerosol-climate models. As it has been demonstrated by Huijnen et al. (2012), Kaiser et al. (2012) and von Hardenberg et al. (2012) and also in the present study, a zero-order approximation of a globally constant tuning factor of 3.4 provides reasonable results for GFAS as well as GFED. However, it remains unclear, why the use of the untuned wildfire aerosol emission inventories leads to a general underestimation of AOT in all state-of-the-art GCMs. An underestimation in the species-specific emission factors may presumably represent one major reason as model biases are significantly smaller for GFAS trace gas species in ECHAM6-HAMMOZ (Martin Schultz, personal communication) and in the MACC project (Inness et al., 2013), even though they are based on the same FRP data set.

- The comparison of emission fluxes and FRP from the present day JSBACH-SPITFIRE simulations to the satellite-based data sets demonstrates that in some regions, e.g. Alaska and Australia, JSBACH-SPITFIRE does not adequately reproduce observed wildfire activity.

- For the future scenarios human activity significantly impacts land-use, population density and fire management. The population density and land-use projections by Klein Goldewijk and Verburg (2013) and Hurtt et al. (2011) applied in this study represent idealized scenarios which have a strong impact on fire activity via fire ignitions and suppression.

The listed issues in emission height and emission flux representations could not be eliminated in the applied model, but the analysis of the presented modeling experiments enabled the quantification of some of these uncertainties.

5.3 Research perspective

The results of this study indicate that for the current generation of ESMs, sophisticated and computationally expensive plume model implementations exceed the model capabilities of ESMs to represent small scale fires and atmospheric properties relevant for the smoke plume development. The modified Sofiev plume height parametrization (Sofiev et al., 2012), which has successfully been modified and applied in other models (Kukkonen et al., 2014; Konovalov et al., 2015), holds the potential to become a standard implementation in aerosol-climate modeling applications where long-range transport and regional aerosol-radiation interactions are of major importance. For long-term simulations it might even be sufficient to prescribe region-, fire-intensity- or climate-specific plume heights based on plume height climatologies. Within an ongoing collaboration between the Laboratoire des Sciences du Climat et de l'Environnement (LSCE) and the Max Planck Institute for Meteorology, a comprehensive, region-specific plume height climatology is currently developed. This global climatology will be based on three data sets: observational data of an updated version of the MPHP data set providing global coverage, several years of ECHAM6-HAM2 simulations with the Sofiev plume height parametrization and several years of MACC simulations with an extended version of the fully analytical PRM model by Paugam et al. (2015). This global plume height climatology will add to the less sophisticated and regional plume height data sets by Val Martin et al. (2012), Sofiev et al. (2013) and Dentener et al. (2006). With the new implementation of fire emission heights in ECHAM6-HAM2 and the additional fire parameters provided by JSBACH-SPITFIRE presented in this study, a novel framework for a full coupling between the land-surface and the atmospheric aerosol model is provided. Although no distinct feedbacks of emission heights, emission fluxes, cloud micro-physics and mesoscale atmospheric dynamics could be identified in this study (partly due to the layout of the experiments), previous studies have shown indications for feedbacks between tropical fire activity and ENSO respectively the Hadley circulation (Tosca et al., 2010, 2013). The use of the fully interactive MPI-ESM with integrated JSBACH-SPITFIRE and extended by the aerosol module HAM will enable new investigations of such potential feedbacks between vegetation dynamics, cloud micro-physics and atmospheric circulation.

Moreover, this study has also shown that, in contrast to emission heights, improved representations of wildfire emission inventories hold a high potential for improvements in aerosol-climate model performance. In consideration of the large uncertainties in all available wildfire emission inventories, the further investigation of two key parameters is required: First, the improvement of high-resolution satellite-based burned area and FRP estimates. The exploration of the sub-pixel-based calculation of MODIS FRP by Peterson et al. (2013a,b, 2014) presents a promising approach to gradually overcome these challenges. Second, the recalibration and extension of species-specific emission factors by the use of up-to-date measurement techniques might substantially reduce the emission

estimate uncertainties. Current activities in this field are largely limited to specific regions and trace gas species (e.g. Akagi et al., 2013; Urbanski, 2014), but a comprehensive research project on an emission factor characterization for carbonaceous aerosol particles would be highly desirable.

Closely linked to improvements in observation-based emission estimates is the representation of wildfire emission release in DGVMs. The comparison of JSBACH-SPITFIRE emission estimates to satellite-based GFAS data provided in this study indicates that the model has difficulties to adequately simulate fire activity in boreal areas. Kantzas et al. (2013) analyzed the fire activity model performance in three state-of-the-art DGVMs and showed that all models fail to reproduce the observed spatial and temporal fire patterns with differences between models of up to a factor of 4. An improved representation of subgrid-scale heterogeneities such as permafrost patterns, landscape fragmentation and a more adequate representation of species-specific fire behavior are expected to decrease the fundamental limitations which still apply to current DGVMs (Kantzas et al., 2013; Alencar et al., 2015; Rogers et al., 2015).

By use of the increasing computational capabilities, it might be possible to significantly improve the complex representation of fires in DVGMs within the next decade. Based on better constrained emission inventories for PD and more realistically simulated emission estimates for future climate conditions, a substantial reduction in aerosol-climate modelling uncertainties might be achieved.

For now, with all the uncertainties included in emission inventories, atmospheric transport and removal processes, an interdisciplinary joint effort is required to step forward towards a more reliable assessment of the fire-climate impact. Sponsored by the Integrated Land Ecosystem Atmosphere Processes Study (iLEAPS) and the World Meteorological Organization (WMO), the Interdisciplinary Biomass Burning Initiative (IBBI) is a promising collaboration which aims to enhance the exchange and communication between vegetation modelers, satellite experts and aerosol-climate modeling groups. In the framework of IBBI, the first vegetation-fire model inter-comparison project is currently initiated. It is highly desirable to strengthen this collaboration and to develop a strategic plan how the scientific community can consolidate the individual progress that has been made so far. Hopefully the results of this PhD study will contribute valuable knowledge to target the right directions of vegetation-fire and aerosol-climate model development in the near future.

Appendix

A.1 Description of the FRP distribution scheme

In the original version of the SPITFIRE model by Thonicke et al. (2010) neither information on FRP nor on the attribution of FRP and emissions to individual fires is included. As described in Sect. 4.2.1, we introduced the diagnostic variable FRP of all fires within a grid cell in JSBACH-SPITFIRE. In addition, we developed an empirical-statistical scheme that aims to distribute the total FRP of a grid box to a given number of individual fires provided by JSBACH-SPITFIRE. Therefore we first calculate a probability density function (PDF) of the FRP distribution to individual fires based on satellite-based GFASv1.2 data. We limit our analysis to FRP classes which bin FRP values in specific ranges, see Sect. 4.2.3. The empirical-statistical FRP distribution scheme is designed to achieve a JSBACH-SPITFIRE PDF which is similar to the PDF derived from GFAS data. To preserve the number of fires and the total FRP of a grid cell simulated by JSBACH-SPITFIRE, modifications have to be applied to the satellite-based GFAS PDF. This is done in the following:

We distribute the total FRP of all fires in a grid cell ($\sum$ FRP) to individual FRP classes as described in Fig. A.1.1. First, we divide $\sum$ FRP by the simulated number of fires N to get an FRP value for the assumption that all fires would have the same FRP. This FRP value α (see red stars in Fig. A.1.1) is compared to the mean FRP value of an individual fire in GFAS, $\overline{FRP_{GFAS}}$. If α is larger than $\overline{FRP_{GFAS}}$, α represents the turning point of the subsequent PDF tuning (see right diagram in Fig. A.1.1). The PDF of all FRP classes larger than α is increased by a factor α / $\overline{FRP_{GFAS}}$. All FRP classes smaller than α are decreased by a factor which scales the remaining FRP classes linearly in a way that the integral over the PDF remains 1, see upward and downward arrows right and left to the red star in the right diagram of Fig. A.1.1. If α is smaller than $\overline{FRP_{GFAS}}$, the up- and down-scaling of FRP classes is applied in different directions as described before.

The updated PDF is used together with a random number generator to calculate a potential FRP of one specific fire. We then test whether the FRP of this fire is smaller or equal the total FRP of all fires $\sum$ FRP in order to decide if the individual FRP is still consistent with the total FRP of a grid cell simulated by JSBACH-SPITFIRE. If the remaining $\sum$ FRP would become negative, the random generator is run once again. Otherwise the specific FRP is subtracted from the remaining $\sum$ FRP and the number of fires N is reduced by 1. Thereafter another iteration of the algorithm is started in case the number of fires is greater than zero. For the last remaining fire within a grid box, the total remaining FRP is automatically adjusted to the nearest FRP class value.

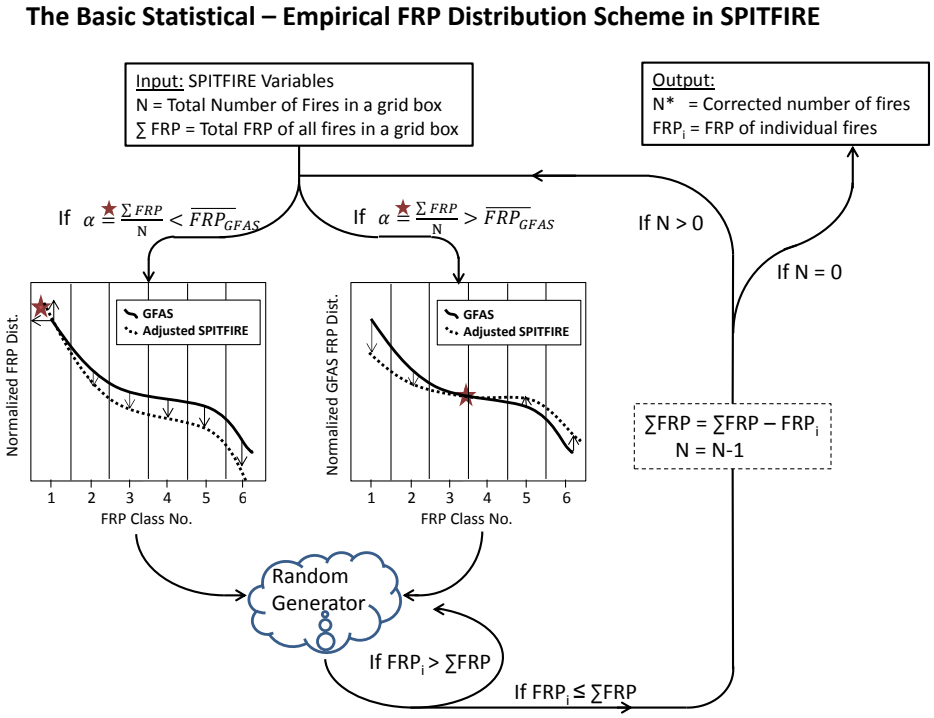

Figure A.1.1: FRP distribution scheme applied in JSBACH-SPITFIRE. Note that the schematic drawing of the normalized FRP distribution includes only six FRP classes for reasons of clarity, but in reality 47 FRP classes are applied.

In rare cases where α is smaller than the FRP of class 1, the standard FRP distribution scheme would a-priori be incapable to realistically allocate the number of fires simulated by JSBACH-SPITFIRE to individual FRP classes. Therefore the FRP value of FRP class no. 1 has to be adjusted. Here, we apply an adjustment of FRP class 1 to a value of $0.25*\alpha$. The value of 0.25 is to some extend arbitrarily chosen, but our empirical test cases indicated a reasonable FRP distribution for this factor.

A.2 Analysis of future regional changes in wildfire activity

In the following, we make an attempt to analyze the main drivers for changes in wildfire emission fluxes in our JSBACH-SPITFIRE simulations. All changes refer to relative differences in total carbon emission fluxes between the JSBACH-SPITFIRE RCP scenarios 2.6, 4.5 and 8.5 for 2090–2099 compared to JSBACH-SPITFIRE PD emissions for 1996–2005. Region-specific analyses are carried out for six major biomass burning regions: Boreal North America, Temperate North America, the Amazon, Africa, Siberia and Australia (see Fig. 4.5). For these regions, we calculate Pearson correlation coefficients between changes in emission fluxes and changes in parameters which are assumed to be the driving forces of wildfires according to the fire process representations in JSBACH-SPITFIRE. The parameters chosen for the analysis are the number of human ignitions, the available fuel of fuel classes 1–100 h, the FDI and precipitation. The results of all parameter analyses are summarized in Table A1.

Generally, significant correlations can be detected for many regions and parameters for RCP8.5, but not for RCP2.6 and RCP4.5, except for Africa and Boreal North America. For RCP8.5, fuel availability is clearly identified to be the major driver of extra-tropical changes in wildfire emissions. The large decrease in African emissions observed in RCP8.5 can primarily be attributed to a strong decrease in human ignition rates caused by land-use change and increasing population density.

Note that the linear correlation analysis shown in this study represents only a rough first estimate of potential drivers for future fire activity. Furthermore, the analysis is limited to 10-year periods in which vegetation dynamics and long-term internal climate variability are not accounted for. A more sophisticated analysis would require an ensemble of separate model simulations with individually fixed parameters. But due to the high computational expenses of the long-term model experiments, these extensions go beyond the scope of the present study.

Table A1: Correlations between changes in fire-driving parameters and changes in carbon emission fluxes for 2090–2099 vs. 1996–2005. Circles (∘) indicate very week or insignificant correlations ($R^2 < 0.2$), plus and minus signs (+/-) represent weak but significant (at a 95 % confidence interval) positive and negative correlations of $0.2 < R^2 < 0.5$ and $-0.5 < R^2 < -0.2$, respectively. Double plus signs (++) indicate strong positive correlations $R^2 > 0.5$.

Parameter	**Temperate NA**	**Boreal NA**	**Siberia**	**Amazon**	**Australia**	**Africa**
RCP2.6 Ignitions	∘	∘	∘	∘	∘	+
RCP2.6 Fuel 1–100 h	∘	+	∘	∘	∘	+
RCP2.6 FDI	∘	+	∘	∘	∘	∘
RCP2.6 Precipitation	∘	∘	∘	∘	∘	+
RCP4.5 Ignitions	∘	∘	∘	∘	∘	∘
RCP4.5 Fuel 1–100 h	∘	∘	∘	∘	∘	+
RCP4.5 FDI	∘	∘	∘	∘	∘	-
RCP4.5 Precipitation	∘	∘	∘	∘	∘	+
RCP8.5 Ignitions	∘	∘	∘	∘	+	++
RCP8.5 Fuel 1–100 h	++	++	+	∘	+	∘
RCP8.5 FDI	∘	+	∘	+	+	∘
RCP8.5 Precipitation	∘	∘	∘	∘	+	∘

A.3 Future changes in dust, sea salt and DMS burdens

In Sect. 4.3.7 the simulated future changes in AOT are discussed and compared to changes in atmospheric burdens of different aerosol species. In addition to the BC burden analysis provided in Sect. 4.3.7, Figure A.3.1 shows relative changes in dust, sea salt and DMS burdens for the CLIMATE-ONLY simulation compared to PD-SPITFIRE.

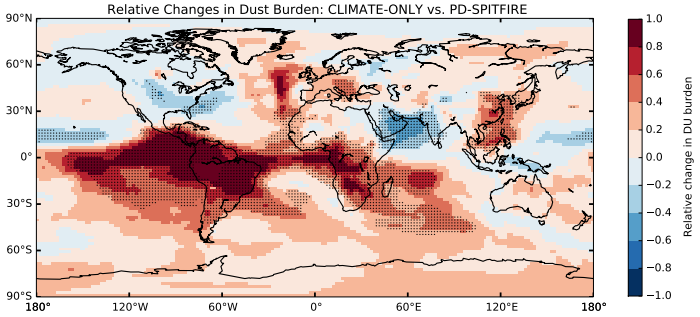

(a)

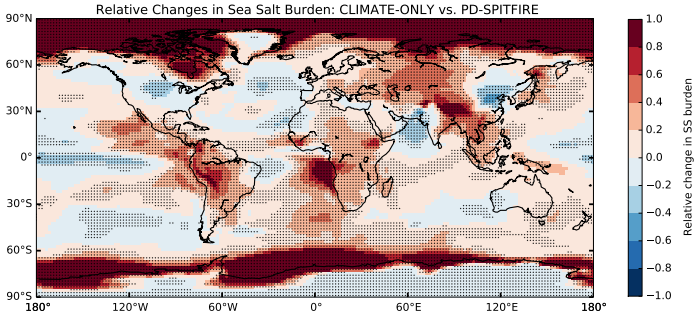

(b)

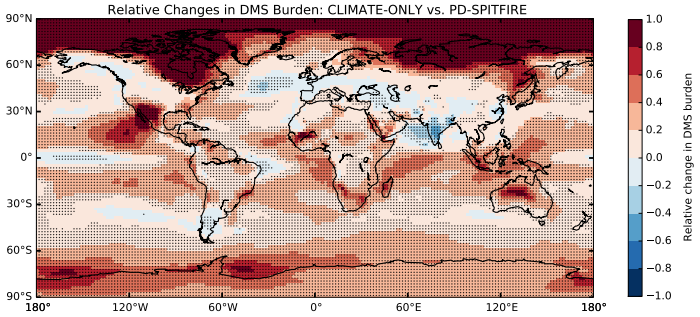

(c)

Figure A.3.1: Relative changes in dust (a), sea salt (b) and DMS (c) burdens for simulation CLIMATE-ONLY (period 2090–2099) compared to the reference simulation PD-SPITFIRE based on the period 1996–2005. Black dots indicate significance of yearly means based on a student-t-test at a 95 % confidence interval.

References

Achtemeier, G. L., Goodrick, S. a., Liu, Y., Garcia-Menendez, F., Hu, Y., and Odman, M. T. (2011). Modeling Smoke Plume-Rise and Dispersion from Southern United States Prescribed Burns with Daysmoke. *Atmosphere*, 2(3):358–388.

Adames, A. F., Reynolds, M., Smirnov, A., Covert, D. S., and Ackerman, T. P. (2011). Comparison of Moderate Resolution Imaging Spectroradiometer ocean aerosol retrievals with ship–based Sun photometer measurements from the Around the Americas expedition. *J. Geophysical Research*, 116.

Akagi, S. K., Yokelson, R. J., Burling, I. R., Meinardi, S., Simpson, I., Blake, D. R., McMeeking, G. R., Sullivan, A., Lee, T., Kreidenweis, S., Urbanski, S., Reardon, J., Griffith, D. W. T., Johnson, T. J., and Weise, D. R. (2013). Measurements of reactive trace gases and variable O3 formation rates in some South Carolina biomass burning plumes. *Atmospheric Chemistry and Physics*, 13(3):1141–1165.

Akagi, S. K., Yokelson, R. J., Wiedinmyer, C., Alvarado, M. J., Reid, J. S., Karl, T., Crounse, J. D., and Wennberg, P. O. (2011). Emission factors for open and domestic biomass burning for use in atmospheric models. *Atmospheric Chemistry and Physics*, 11(9):4039–4072.

Albrecht, B. (1989). Aerosols, cloud microphysics, and fractional cloudiness. *Science*, 245(4923):1227–1230.

Alencar, A., Brando, P., Asner, G., and Putz, F. (2015). Landscape Fragmentation, Severe Drought and the New Amazon Forest Fire Regime. *Ecological Applications*, doi:10.1890/14-1528.1.

Andreae, M. and Gelencsér, A. (2006). Black carbon or brown carbon? The nature of light-absorbing carbonaceous aerosols. *Atmospheric Chemistry and Physics*, 6(10):3131–3148.

Andreae, M. and Merlet, P. (2001). Emission of trace gases and aerosols from biomass burning. *Global biogeochemical cycles*, 15(4):955–966.

Andreae, M. and Rosenfeld, D. (2008). Aerosol-cloud-precipitation interactions. Part 1. The nature and sources of cloud-active aerosols. *Earth-Science Reviews*, 89(1-2):13–41.

Andreae, M. O., Rosenfeld, D., Artaxo, P., Costa, a. a., Frank, G. P., Longo, K. M., and Silva-Dias, M. a. F. (2004). Smoking rain clouds over the Amazon. *Science*, 303(5662):1337–42.

Andrews, P. (2009). *BehavePlus fire modeling system, version 5.0: Variables*. Rocky Mountain Research Station Publishing Services, Fort Collins, Colorado, USA.

Ångström, A. (1962). Atmospheric turbidity, global illumination and planetary albedo of the earth. *Tellus*, 14:435–450.

Archer-Nicholls, S., Lowe, D., Darbyshire, E., Morgan, W. T., Bela, M. M., Pereira, G., Trembath, J., Kaiser, J. W., Longo, K. M., Freitas, S. R., Coe, H., and McFiggans, G. (2015). Characterising Brazilian biomass burning emissions using WRF-Chem with MOSAIC sectional aerosol. *Geoscientific Model Development*, 8(3):549–577.

Arora, V. K. and Boer, G. J. (2005). Fire as an interactive component of dynamic vegetation models. *Journal of Geophysical Research*, 110(G2):G02008.

Ban-Weiss, G. a., Cao, L., Bala, G., and Caldeira, K. (2011). Dependence of climate forcing and response on the altitude of black carbon aerosols. *Climate Dynamics*, 38(5-6):897–911.

Beer, T. and Williams, A. (1995). Estimating Australian forest fire danger under conditions of doubled carbon dioxide concentrations. *Climatic change*, 29(2):169–188.

Bond, T. C., Doherty, S. J., Fahey, D. W., Forster, P. M., Berntsen, T., DeAngelo, B. J., Flanner, M. G., Ghan, S., Kärcher, B., Koch, D., Kinne, S., Kondo, Y., Quinn, P. K., Sarofim, M. C., Schultz, M. G., Schulz, M., Venkataraman, C., Zhang, H., Zhang, S., Bellouin, N., Guttikunda, S. K., Hopke, P. K., Jacobson, M. Z., Kaiser, J. W., Klimont, Z., Lohmann, U., Schwarz, J. P., Shindell, D., Storelvmo, T., Warren, S. G., and Zender, C. S. (2013). Bounding the role of black carbon in the climate system: A scientific assessment. *Journal of Geophysical Research: Atmospheres*, 118(11):5380–5552.

Bond, W. J. and Keeley, J. E. (2005). Fire as a global 'herbivore': the ecology and evolution of flammable ecosystems. *Trends in ecology and evolution*, 20(7):387–94.

Boucher, O., Randall, D., Artaxo, P., Bretherton, C., Feingold, G., Forster, P., Kerminen, V.-M., Kondo, Y., Liao, H., Lohmann, U., Rasch, P., Satheesh, S., Sherwood, S., Stevens, B., and Zhang, X. (2013). *Clouds and Aerosols*, book section 7, pages 571–657. Cambridge University Press, Cambridge, United Kingdom and New York, NY, USA.

Bourgeois, Q. and Bey, I. (2011). Pollution transport efficiency toward the Arctic: Sensitivity to aerosol scavenging and source regions. *Journal of Geophysical Research*, 116(D8):D08213.

Bowman, D. M. J. S., Balch, J. K., Artaxo, P., Bond, W. J., Carlson, J. M., Cochrane, M. a., D'Antonio, C. M., Defries, R. S., Doyle, J. C., Harrison, S. P., Johnston, F. H., Keeley, J. E., Krawchuk, M. a., Kull, C. a., Marston, J. B., Moritz, M. a., Prentice, I. C., Roos, C. I., Scott, A. C., Swetnam, T. W., van der Werf, G. R., and Pyne, S. J. (2009). Fire in the Earth system. *Science*, 324(5926):481–4.

Bréon, F.-M., Vermeulen, A., and Descloitres, J. (2011). An evaluation of satellite aerosol products against sunphotometer measurements. *Remote Sensing of Environment*, 115(12):3102–3111.

Briggs, G. (1969). Optimum formulas for buoyant plume rise. *Philosophical Transactions of the Royal Society of London. Series A, Mathematical and Physical Sciences*, 265(1161):197–203.

Briggs, G. (1975). Plume Rise Predictions. *Lectures on air pollution and environmental impact analysis*, pages 59–111.

Brovkin, V., Boysen, L., Raddatz, T., Gayler, V., Loew, A., and Claussen, M. (2013). Evaluation of vegetation cover and land-surface albedo in MPI-ESM CMIP5 simulations. *Journal of Advances in Modeling Earth Systems*, 5(1):48–57.

Campbell, J. R., Reid, J. S., Westphal, D. L., Zhang, J., Tackett, J. L., Chew, B. N., Welton, E. J., Shimizu, A., Sugimoto, N., Aoki, K., and Winker, D. M. (2013). Characterizing the vertical profile of aerosol particle extinction and linear depolarization over Southeast Asia and the Maritime Continent: The 2007–2009 view from CALIOP. *Atmospheric Research*, 122:520–543.

Carslaw, K. S., Boucher, O., Spracklen, D. V., Mann, G. W., Rae, J. G. L., Woodward, S., and Kulmala, M. (2010). A review of natural aerosol interactions and feedbacks within the Earth system. *Atmospheric Chemistry and Physics*, 10(4):1701–1737.

Certini, G. (2005). Effects of fire on properties of forest soils: a review. *Oecologia*, 143(1):1–10.

Chen, Y., Li, Q., Randerson, J. T., Lyons, E. a., Kahn, R. a., Nelson, D. L., and Diner, D. J. (2009). The sensitivity of CO and aerosol transport to the temporal and vertical distribution of North American boreal fire emissions. *Atmospheric Chemistry and Physics*, 9(17):6559—-6580.

Ciais, P., Sabine, C., Bala, G., Bopp, L., Brovkin, V., Canadell, J., Chhabra, A., DeFries, R., Galloway, J., Heimann, M., Jones, C., LeQuéré, C., Myneni, R., Piao, S., and Thornton, P. (2013). *Carbon and Other Biogeochemical Cycles*, book section 6, pages 465–570. Cambridge University Press, Cambridge, United Kingdom and New York, NY, USA.

Colarco, P. R. (2004). Transport of smoke from Canadian forest fires to the surface near Washington, D.C.: Injection height, entrainment, and optical properties. *Journal of Geophysical Research*, 109(D6):D06203.

Crutzen, P. and Andreae, M. (1990). Biomass burning in the tropics: Impact on atmospheric chemistry and biogeochemical cycles. *Science*, 250(4988):1669–1678.

Damoah, R., Spichtinger, N., Servranckx, R., Fromm, M., Eloranta, E. W., Razenkov, I. a., James, P., Shulski, M., Forster, C., and Stohl, a. (2006). A case study of pyro-convection using transport model and remote sensing data. *Atmospheric Chemistry and Physics*, 6(1):173–185.

de Groot, W. J., Flannigan, M. D., and Cantin, A. S. (2013). Climate change impacts on future boreal fire regimes. *Forest Ecology and Management*, 294:35–44.

Dee, D. P., Uppala, S. M., Simmons, a. J., Berrisford, P., Poli, P., Kobayashi, S., Andrae, U., Balmaseda, M. a., Balsamo, G., Bauer, P., Bechtold, P., Beljaars, a. C. M., van de Berg, L., Bidlot, J., Bormann, N., Delsol, C., Dragani, R., Fuentes, M., Geer, a. J., Haimberger, L., Healy, S. B., Hersbach, H., Hólm, E. V., Isaksen, L., Kå llberg, P., Köhler, M., Matricardi, M., McNally, a. P., Monge-Sanz, B. M., Morcrette, J.-J., Park, B.-K., Peubey, C., de Rosnay, P., Tavolato, C., Thépaut, J.-N., and Vitart, F. (2011). The ERA-Interim reanalysis: configuration and performance of the data assimilation system. *Quarterly Journal of the Royal Meteorological Society*, 137(656):553–597.

Dentener, F., Drevet, J., Lamarque, J. F., Bey, I., Eickhout, B., Fiore, a. M., Hauglustaine, D., Horowitz, L. W., Krol, M., Kulshrestha, U. C., Lawrence, M., Galy-Lacaux, C., Rast, S., Shindell, D., Stevenson, D., Van Noije, T., Atherton, C., Bell, N., Bergman, D., Butler, T., Cofala, J., Collins, B., Doherty, R., Ellingsen, K., Galloway, J., Gauss, M., Montanaro, V., Müller, J. F., Pitari, G., Rodriguez, J., Sanderson, M., Solmon, F., Strahan, S., Schultz, M., Sudo, K., Szopa, S., and Wild, O. (2006). Nitrogen and sulfur deposition on regional and global scales: A multimodel evaluation. *Global Biogeochemical Cycles*, 20(4).

Dickinson, K. and Kirkpatrick, J. (1985). The flammability and energy content of some important plant species and fuel components in the forests of southeastern Tasmania. *Journal of Biogeography*, 12(2):121–134.

Diner, D., Beckert, J., Reilly, T., Bruegge, C., Conel, J., Kahn, R., Martonchik, J., Ackerman, T., Davies, R., Gerstl, S., Gordon, H., Muller, J., Myneni, R., Sellers, P., Pinty, B., and Verstraete, M. (1998). Multi-angle Imaging SpectroRadiometer (MISR) instrument description and experiment overview. *IEEE Transactions on Geoscience and Remote Sensing*, 36(4):1072–1087.

Diner, D. J., Nelson, D. L., Chen, Y., Kahn, R. a., Logan, J., Leung, F.-Y., and Val Martin, M. (2008). Quantitative studies of wildfire smoke injection heights with the Terra Multi-angle Imaging SpectroRadiometer. *Proceedings of SPIE*, 7089.

Dirksen, R. J., Folkert Boersma, K., de Laat, J., Stammes, P., van der Werf, G. R., Val Martin, M., and Kelder, H. M. (2009). An aerosol boomerang: Rapid around-the-world transport of smoke from the December 2006 Australian forest fires observed from space. *Journal of Geophysical Research*, 114(D21):D21201.

Dumont, M., Brun, E., Picard, G., Michou, M., Libois, Q., Petit, J.-R., Geyer, M., Morin, S., and Josse, B. (2014). Contribution of light-absorbing impurities in snow to Greenland's darkening since 2009. *Nature Geoscience*, 7(7):509–512.

Eck, T. F., Holben, B. N., Reid, J. S., Dubovik, O., Smirnov, A., Neill, N. T. O., Slutsker, I., and Kinne, S. (1999). Wavelength dependence of optical depth of biomass burning, urban and desert dust aerosols. *J. Geophysical Research*, 104:31,333 – 3,349.

Flanner, M. G., Zender, C. S., Randerson, J. T., and Rasch, P. J. (2007). Present-day climate forcing and response from black carbon in snow. *Journal of Geophysical Research*, 112(D11):D11202.

Flannigan, M., Cantin, A. S., de Groot, W. J., Wotton, M., Newbery, A., and Gowman, L. M. (2013). Global wildland fire season severity in the 21st century. *Forest Ecology and Management*, 294:54–61.

Flannigan, M. and Wagner, C. (1991). Climate change and wildfire in Canada. *Canadian Journal of Forest Research*, 21(1):66–72.

Flannigan, M. D., Krawchuk, M. a., de Groot, W. J., Wotton, B. M., and Gowman, L. M. (2009). Implications of changing climate for global wildland fire. *International Journal of Wildland Fire*, 18(5):483.

Freeborn, P. H., Wooster, M. J., Hao, W. M., Ryan, C. a., Nordgren, B. L., Baker, S. P., and Ichoku, C. (2008). Relationships between energy release, fuel mass loss, and trace gas and aerosol emissions during laboratory biomass fires. *Journal of Geophysical Research*, 113(D1):D01301.

Freitas, S. R., Longo, K. M., Chatfield, R., Latham, D., Silva Dias, M. A. F., Andreae, M. O., Prins, E., Santos, J. C., Gielow, R., and Carvalho, J. A. (2007). Including the sub-grid scale plume rise of vegetation fires in low resolution atmospheric transport models. *Atmospheric Chemistry and Physics*, 7(13):3385–3398.

Freitas, S. R., Longo, K. M., Trentmann, J., and Latham, D. (2010). Technical Note: Sensitivity of 1-D smoke plume rise models to the inclusion of environmental wind drag. *Atmospheric Chemistry and Physics*, 10(2):585–594.

Fromm, M., Lindsey, D. T., Servranckx, R., Yue, G., Trickl, T., Sica, R., Doucet, P., and Godin-Beekmann, S. (2010). The Untold Story of Pyrocumulonimbus. *Bulletin of the American Meteorological Society*, 91(9):1193–1209.

Fromm, M., Torres, O., Diner, D., Lindsey, D., Vant Hull, B., Servranckx, R., Shettle, E. P., and Li, Z. (2008). Stratospheric impact of the Chisholm pyrocumulonimbus eruption: 1. Earth-viewing satellite perspective. *Journal of Geophysical Research*, 113(D8):D08202.

Fromm, M., Tupper, A., Rosenfeld, D., Servranckx, R., and McRae, R. (2006). Violent pyro-convective storm devastates Australia's capital and pollutes the stratosphere. *Geophysical Research Letters*, 33(5):L05815.

Giglio, L., Van Der Werf, G. R., Randerson, J. T., Collatz, G. J., and Kasibhatla, P. (2006). Global estimation of burned area using MODIS active fire observations. *Atmospheric Chemistry and Physics*, 6(4):957–974.

Giorgetta, M. a., Jungclaus, J., Reick, C. H., Legutke, S., Bader, J., Böttinger, M., Brovkin, V., Crueger, T., Esch, M., Fieg, K., Glushak, K., Gayler, V., Haak, H., Hollweg, H.-D., Ilyina, T., Kinne, S., Kornblueh, L., Matei, D., Mauritsen, T., Mikolajewicz, U., Mueller, W., Notz, D., Pithan, F., Raddatz, T., Rast, S., Redler, R., Roeckner, E., Schmidt, H., Schnur, R., Segschneider, J., Six, K. D., Stockhause, M., Timmreck, C., Wegner, J., Widmann, H., Wieners, K.-H., Claussen, M., Marotzke, J., and Stevens, B. (2013). Climate and carbon cycle changes from 1850 to 2100 in MPI-ESM simulations for the Coupled Model Intercomparison Project phase 5. *Journal of Advances in Modeling Earth Systems*, 5(3):572–597.

Goldewijk, K. (2001). Estimating global land use change over the past 300 years: the HYDE database. *Global Biogeochemical Cycles*, 15(2):417–433.

Gonzi, S. and Palmer, P. I. (2010). Vertical transport of surface fire emissions observed from space. *Journal of Geophysical Research*, 115(D2):D02306.

Gonzi, S., Palmer, P. I., Paugam, R., Wooster, M., and Deeter, M. N. (2015). Quantifying pyroconvective injection heights using observations of fire energy: sensitivity of spaceborne observations of carbon monoxide. *Atmospheric Chemistry and Physics*, 15(8):4339–4355.

Goodrick, S., Achtemeier, G., and Larkin, N. (2012). Modelling smoke transport from wildland fires: a review. *International Journal of Wildland Fire*, 22(1):83–94.

Grell, G., Freitas, S. R., Stuefer, M., and Fast, J. (2011). Inclusion of biomass burning in WRF-Chem: impact of wildfires on weather forecasts. *Atmospheric Chemistry and Physics*, 11(11):5289–5303.

Hansen, J. and Nazarenko, L. (2004). Soot climate forcing via snow and ice albedos. *Proceedings of the National Academy of Sciences of the United States of America*, 101(2):423–8.

Hantson, S., Lasslop, G., Kloster, S., and Chuvieco, E. (2015). Anthropogenic effects on global mean fire size. *International Journal of Wildland Fire*, 24:589–596.

Haywood, J. and Boucher, O. (2000). Estimates of the direct and indirect radiative forcing due to tropospheric aerosols: A review. *Reviews of Geophysics*, 38(4):513–543.

Heald, C. L., Ridley, D. a., Kroll, J. H., Barrett, S. R. H., Cady-Pereira, K. E., Alvarado, M. J., and Holmes, C. D. (2014). Contrasting the direct radiative effect and direct radiative forcing of aerosols. *Atmospheric Chemistry and Physics*, 14(11):5513–5527.

Heikes, K. E. and Angeles, L. (1990). Numerical simulation of small area fires. *Atmospheric Environment. Part A.*, 24(2):297–307.

Heilman, W. E., Liu, Y., Urbanski, S., Kovalev, V., and Mickler, R. (2013). Wildland fire emissions, carbon, and climate: Plume rise, atmospheric transport, and chemistry processes. *Forest Ecology and Management*, 317:80–96.

Henderson, S. B., Ichoku, C., Burkholder, B. J., Brauer, M., and Jackson, P. L. (2010). The validity and utility of MODIS data for simple estimation of area burned and aerosols emitted by wildfire events. *International Journal of Wildland Fire*, 19(7):844.

Hodzic, A., Madronich, S., Bohn, S., Massie, S., Menut, L., and Wiedinmyer, C. (2007). Wildfire particulate matter in Europe during summer 2003: meso-scale modeling of smoke emissions, transport and radiative effects. *Atmospheric Chemistry and Physics*, 7(2):4705–4760.

Holben, B. N., Eck, T. F., Slutsker, I., Tanre, D., Buis, J. P., Setzer, A., Vermote, E., Reagan, J. A., Kaufman, Y. J., Nakajima, T., Lavenu, F., Jankowiak, I., and Smirnov, A. (1998). AERONET - A Federated Instrument Network and Data Archive for Aerosol Characterization. *Remote Sensing of Environment*, 66:1–16.

Huijnen, V., Flemming, J., Kaiser, J. W., Inness, a., Leitão, J., Heil, a., Eskes, H. J., Schultz, M. G., Benedetti, a., Hadji-Lazaro, J., Dufour, G., and Eremenko, M. (2012). Hindcast experiments of tropospheric composition during the summer 2010 fires over western Russia. *Atmospheric Chemistry and Physics*, 12(9):4341–4364.

Hurrell, J. W., Hack, J. J., Shea, D., Caron, J. M., and Rosinski, J. (2008). A New Sea Surface Temperature and Sea Ice Boundary Dataset for the Community Atmosphere Model. *Journal of Climate*, 21(19):5145–5153.

Hurtt, G. C., Chini, L. P., Frolking, S., Betts, R. a., Feddema, J., Fischer, G., Fisk, J. P., Hibbard, K., Houghton, R. a., Janetos, a., Jones, C. D., Kindermann, G., Kinoshita, T., Klein Goldewijk, K., Riahi, K., Shevliakova, E., Smith, S., Stehfest, E., Thomson, a., Thornton, P., Vuuren, D. P., and Wang, Y. P. (2011). Harmonization of land-use scenarios for the period 1500-2100: 600 years of global gridded annual land-use transitions, wood harvest, and resulting secondary lands. *Climatic Change*, 109(1-2):117–161.

Hyer, E. J., Allen, D. J., and Kasischke, E. S. (2007). Examining injection properties of boreal forest fires using surface and satellite measurements of CO transport. *Journal of Geophysical Research*, 112(D18):D18307.

Hyer, E. J., Reid, J. S., and Zhang, J. (2011). An over-land aerosol optical depth data set for data assimilation by filtering, correction, and aggregation of MODIS Collection 5 optical depth retrievals. *Atmos. Meas. Tech.*, 4:379–408.

Ichoku, C. and Ellison, L. (2014). Global top-down smoke-aerosol emissions estimation using satellite fire radiative power measurements. *Atmospheric Chemistry and Physics*, 14(13):6643–6667.

Ichoku, C., Kahn, R., and Chin, M. (2012). Satellite contributions to the quantitative characterization of biomass burning for climate modeling. *Atmospheric Research*, 111:1–28.

Inness, A., Baier, F., Benedetti, A., Bouarar, I., Chabrillat, S., Clark, H., Clerbaux, C., Coheur, P., Engelen, R. J., Errera, Q., Flemming, J., George, M., Granier, C., Hadji-Lazaro, J., Huijnen, V., Hurtmans, D., Jones, L., Kaiser, J. W., Kapsomenakis, J., Lefever, K., Leitão, J., Razinger, M., Richter, A., Schultz, M. G., Simmons, A. J., Suttie, M., Stein, O., Thépaut, J.-N., Thouret, V., Vrekoussis, M., and Zerefos, C. (2013). The MACC reanalysis: an 8 yr data set of atmospheric composition. *Atmospheric Chemistry and Physics*, 13(8):4073–4109.

Jian, Y. and Fu, T.-M. (2014). Injection heights of springtime biomass-burning plumes over peninsular Southeast Asia and their impacts on long-range pollutant transport. *Atmospheric Chemistry and Physics*, 14(8):3977–3989.

Johnson, B. T., Shine, K. P., and Forster, P. M. (2004). The semi-direct aerosol effect: Impact of absorbing aerosols on marine stratocumulus. *Quarterly Journal of the Royal Meteorological Society*, 130(599):1407–1422.

Jones, A., Haywood, J. M., and Boucher, O. (2007). Aerosol forcing, climate response and climate sensitivity in the Hadley Centre climate model. *Journal of Geophysical Research: Atmospheres*, 112(D20).

Joshi, M. M., Gregory, J. M., Webb, M. J., Sexton, D. M. H., and Johns, T. C. (2007). Mechanisms for the land/sea warming contrast exhibited by simulations of climate change. *Climate Dynamics*, 30(5):455–465.

Jost, H.-J. (2004). In-situ observations of mid-latitude forest fire plumes deep in the stratosphere. *Geophysical Research Letters*, 31(11):L11101.

Kacenelenbogen, M., Vaughan, M. a., Redemann, J., Hoff, R. M., Rogers, R. R., Ferrare, R. a., Russell, P. B., Hostetler, C. a., Hair, J. W., and Holben, B. N. (2011). An accuracy assessment of the CALIOP/CALIPSO version 2/version 3 daytime aerosol extinction product based on a detailed multi-sensor, multi-platform case study. *Atmospheric Chemistry and Physics*, 11(8):3981–4000.

Kahn, R. A., Chen, Y., Nelson, D. L., Leung, F.-Y., Li, Q., Diner, D. J., and Logan, J. A. (2008). Wildfire smoke injection heights: Two perspectives from space. *Geophysical Research Letters*, 35(4):18–21.

Kahn, R. A., Li, W.-H., Moroney, C., Diner, D. J., Martonchik, J. V., and Fishbein, E. (2007). Aerosol source plume physical characteristics from space-based multiangle imaging. *Journal of Geophysical Research*, 112(D11):D11205.

Kaiser, J. W., Heil, a., Andreae, M. O., Benedetti, A., Chubarova, N., Jones, L., Morcrette, J.-J., Razinger, M., Schultz, M. G., Suttie, M., and van der Werf, G. R. (2012). Biomass burning emissions estimated with a global fire assimilation system based on observed fire radiative power. *Biogeosciences*, 9(1):527–554.

Kantzas, E., Lomas, M., and Quegan, S. (2013). Fire at high latitudes: Data-model comparisons and their consequences. *Global Biogeochemical Cycles*, 27(3):677–691.

Keywood, M., Kanakidou, M., Stohl, A., Dentener, F., Grassi, G., Meyer, C. P., Torseth, K., Edwards, D., Thompson, A. M., Lohmann, U., and Burrows, J. (2013). Fire in the Air - Biomass burning impacts in a changing climate. *Critical Reviews in Environmental Science and Technology*, 43(January):40–83.

Kinne, S., Schulz, M., and Textor, C. (2006). An AeroCom initial assessment - optical properties in aerosol component modules of global models. *Atmospheric Chemistry and Physics*, 6(7):1815–1834.

Kipling, Z., Stier, P., Schwarz, J. P., Perring, a. E., Spackman, J. R., Mann, G. W., Johnson, C. E., and Telford, P. J. (2013). Constraints on aerosol processes in climate models from vertically-resolved aircraft observations of black carbon. *Atmospheric Chemistry and Physics*, 13(12):5969–5986.

Klein Goldewijk, K. and Verburg, P. H. (2013). Uncertainties in global-scale reconstructions of historical land use: an illustration using the HYDE data set. *Landscape Ecology*, 28(5):861–877.

Kloster, S., Mahowald, N. M., Randerson, J. T., and Lawrence, P. J. (2012). The impacts of climate, land use, and demography on fires during the 21st century simulated by CLM-CN. *Biogeosciences*, 9(1):509–525.

Kloster, S., Mahowald, N. M., Randerson, J. T., Thornton, P. E., Hoffman, F. M., Levis, S., Lawrence, P. J., Feddema, J. J., Oleson, K. W., and Lawrence, D. M. (2010). Fire dynamics during the 20th century simulated by the Community Land Model. *Biogeosciences*, 7(6):1877–1902.

Koch, D., Schulz, M., Kinne, S., Bond, T. C., Balkanski, Y., Bauer, S., Berntsen, T., Boucher, O., Chin, M., Clarke, A., De Luca, N., Dentener, F., Diehl, T., Dubovik, O., Easter, R., Fahey, D. W., Feichter, J., Fillmore, D., Freitag, S., Ghan, S., Ginoux, P., Gong, S., Horowitz, L., Iversen, T., Kirkevå g, A., Klimont, Z., Kondo, Y., Krol, M., Liu, X., McNaughton, C., Miller, R., Montanaro, V., Moteki, N., Myhre, G., Penner, J. E., Perlwitz, J., Pitari, G., Reddy, S., Sahu, L., Sakamoto, H., Schuster, G., Schwarz, J. P., Seland, O., Spackman, J. R., Stier, P., Takegawa, N., Takemura, T., Textor, C., Van Aardenne, J. A., and Zhao, Y. (2009). Evaluation of black carbon estimations in global aerosol models. *Atmospheric Chemistry and Physics*, 9(4):9001–9026.

Koffi, B., Schulz, M., Bréon, F.-M., Griesfeller, J., Winker, D., Balkanski, Y., Bauer, S., Berntsen, T., Chin, M., Collins, W. D., Dentener, F., Diehl, T., Easter, R., Ghan, S., Ginoux, P., Gong, S., Horowitz, L. W., Iversen, T., Kirkevå g, A., Koch, D., Krol, M., Myhre, G., Stier, P., and Takemura, T. (2012). Application of the CALIOP layer product to evaluate the vertical distribution of aerosols estimated by global models: AeroCom phase I results. *Journal of Geophysical Research*, 117(D10):D10201.

Konovalov, I. B., Beekmann, M., Berezin, E. V., Petetin, H., Mielonen, T., Kuznetsova, I. N., and Andreae, M. O. (2015). The role of semi-volatile organic compounds in the mesoscale evolution of biomass burning aerosol: a modelling case study of the 2010 mega-fire event in Russia. *Atmospheric Chemistry and Physics Discussions*, 15:9107–9172.

Konovalov, I. B., Berezin, E. V., Ciais, P., Broquet, G., Beekmann, M., Hadji-Lazaro, J., Clerbaux, C., Andreae, M. O., Kaiser, J. W., and Schulze, E.-D. (2014). Constraining CO2 emissions from open biomass burning by satellite observations of co-emitted species: a method and its application to wildfires in Siberia. *Atmospheric Chemistry and Physics*, 14(19):10383–10410.

Kremens, R., Dickinson, M., and Bova, A. (2012). Radiant flux density, energy density and fuel consumption in mixed-oak forest surface fires. *International Journal of Wildland Fire*, 21:722–730.

Kukkonen, J., Nikmo, J., Sofiev, M., Riikonen, K., Petäjä, T., Virkkula, A., Levula, J., Schobesberger, S., and Webber, D. M. (2014). Applicability of an integrated plume rise model for the dispersion from wild-land fires. *Geoscientific Model Development Discussions*, 7(1):483–527.

Lamarque, J.-F., Kyle, G. P., Meinshausen, M., Riahi, K., Smith, S. J., van Vuuren, D. P., Conley, A. J., and Vitt, F. (2011). Global and regional evolution of short-lived radiatively-active gases and aerosols in the Representative Concentration Pathways. *Climatic Change*, 109(1-2):191–212.

Langmann, B., Duncan, B., Textor, C., Trentmann, J., and van der Werf, G. R. (2009). Vegetation fire emissions and their impact on air pollution and climate. *Atmospheric Environment*, 43(1):107–116.

Lasslop, G., Thonicke, K., and Kloster, S. (2014). SPITFIRE within the MPI Earth system model: Model development and evaluation. *Journal of Advances in Modeling Earth Systems*, 6.

Lavoué, D., Liousse, C., Cachier, H., Stocks, B. J., and Goldammer, J. G. (2000). Modeling of carbonaceous particles emitted by boreal and temperate wildfires at northern latitudes. *Journal of Geophysical Research*, 105:26871–26890.

Leung, F.-Y. T., Logan, J. A., Park, R., Hyer, E., Kasischke, E., Streets, D., and Yurganov, L. (2007). Impacts of enhanced biomass burning in the boreal forests in 1998 on tropospheric chemistry and the sensitivity of model results to the injection height of emissions. *Journal of Geophysical Research*, 112(D10):D10313.

Liousse, C., Penner, J. E., Chuang, C., Walton, J. J., Eddleman, H., and Cachier, H. (1996). A global three-dimensional model study of carbonaceous aerosols. *Journal of Geophysical Research*, 101(95):19411–19432.

Liu, Y., Achtemeier, G. L., Goodrick, S. L., and Jackson, W. a. (2010a). Important parameters for smoke plume rise simulation with Daysmoke. *Atmospheric Pollution Research*, 1(September 2006):250–259.

Liu, Y., Goodrick, S. L., Achtemeier, G. L., Forbus, K., and Combs, D. (2013). Smoke plume height measurement of prescribed burns in the south-eastern United States. *International Journal of Wildland Fire*, 22:130–147.

Liu, Y., Stanturf, J., and Goodrick, S. (2010b). Trends in global wildfire potential in a changing climate. *Forest Ecology and Management*, 259(4):685–697.

Loehman, R. A., Reinhardt, E., and Riley, K. L. (2014). Wildland fire emissions, carbon, and climate: Seeing the forest and the trees - A cross-scale assessment of wildfire and carbon dynamics in fire-prone, forested ecosystems. *Forest Ecology and Management*, 317:9–19.

Lohmann, U. and Feichter, J. (2005). Global indirect aerosol effects: a review. *Atmospheric Chemistry and Physics*, 5(3):715–737.

Lohmann, U., Stier, P., Hoose, C., Ferrachat, S., Kloster, S., Roeckner, E., and Zhang, J. (2007). Cloud microphysics and aerosol indirect effects in the global climate model ECHAM5-HAM. *Atmospheric Chemistry and Physics*, 7(13):3425–3446.

Luderer, G., Trentmann, J., Winterrath, T., Textor, C., Herzog, M., Graf, H. F., and Andreae, M. O. (2006). Modeling of biomass smoke injection into the lower stratosphere by a large forest fire (Part II): sensitivity studies. *Atmospheric Chemistry and Physics*, 6(4):5261–5277.

Luo, L., Tang, Y., Zhong, S., Bian, X., and Heilman, W. E. (2013). Will Future Climate Favor More Erratic Wildfires in the Western United States? *Journal of Applied Meteorology and Climatology*, 52(11):2410–2417.

Ma, X., Bartlett, K., Harmon, K., and Yu, F. (2013). Comparison of AOD between CALIPSO and MODIS: significant differences over major dust and biomass burning regions. *Atmospheric Measurement Techniques*, 6(9):2391–2401.

Marlon, J. R., Bartlein, P. J., Carcaillet, C., Gavin, D. G., Harrison, S. P., Higuera, P. E., Joos, F., Power, M. J., and Prentice, I. C. (2008). Climate and human influences on global biomass burning over the past two millennia. *Nature Geoscience*, 1(10):697–702.

Matichuk, R. I., Colarco, P. R., Smith, J. a., and Toon, O. B. (2007). Modeling the transport and optical properties of smoke aerosols from African savanna fires during the Southern African Regional Science Initiative campaign (SAFARI 2000). *Journal of Geophysical Research*, 112(D8):D08203.

Mazzoni, D., Logan, J. a., Diner, D., Kahn, R., Tong, L., and Li, Q. (2007). A data-mining approach to associating MISR smoke plume heights with MODIS fire measurements. *Remote Sensing of Environment*, 107(1-2):138–148.

Melnikov, V. M., Zrnic, D. S., Rabin, R. M., and Zhang, P. (2008). Radar polarimetric signatures of fire plumes in Oklahoma. *Geophysical Research Letters*, 35(14):L14815.

Mims, S., Kahn, R., Moroney, C., Gaitley, B., Nelson, D., and Garay, M. (2010). MISR Stereo Heights of Grassland Fire Smoke Plumes in Australia. *IEEE Transactions on Geoscience and Remote Sensing*, 48(1):25–35.

Morandini, F., Perez-Ramirez, Y., Tihay, V., Santoni, P.-A., and Barboni, T. (2013). Radiant, convective and heat release characterization of vegetation fire. *International Journal of Thermal Sciences*, 70:83–91.

Moritz, M., Parisien, M., and Batllori, E. (2012). Climate change and disruptions to global fire activity. *Ecosphere*, 3:1–22.

Myhre, G., Berglen, T. F., Johnsrud, M., Hoyle, C. R., Berntsen, T. K., Christopher, S. A., and Fahey, D. W. (2009). Modelled radiative forcing of the direct aerosol effect with multi-observation evaluation. *Atmospheric Chemistry and Physics*, 9(4):1365–1392.

Myhre, G., Samset, B. H., Schulz, M., Balkanski, Y., Bauer, S., Berntsen, T. K., Bian, H., Bellouin, N., Chin, M., Diehl, T., Easter, R. C., Feichter, J., Ghan, S. J., Hauglustaine, D., Iversen, T., Kinne, S., Kirkevå g, a., Lamarque, J.-F., Lin, G., Liu, X., Lund, M. T., Luo, G., Ma, X., van Noije, T., Penner, J. E., Rasch, P. J., Ruiz, a., Seland, O., Skeie, R. B., Stier, P., Takemura, T., Tsigaridis, K., Wang, P., Wang, Z., Xu, L., Yu, H., Yu, F., Yoon, J.-H., Zhang, K., Zhang, H., and Zhou, C. (2013). Radiative forcing of the direct aerosol effect from AeroCom Phase II simulations. *Atmospheric Chemistry and Physics*, 13(4):1853–1877.

Neary, D. G., Klopatek, C. C., DeBano, L. F., and Ffolliott, P. F. (1999). Fire effects on belowground sustainability: a review and synthesis. *Forest Ecology and Management*, 122(1-2):51–71.

Nelson, D., Garay, M., Kahn, R., and Dunst, B. (2013). Stereoscopic Height and Wind Retrievals for Aerosol Plumes with the MISR INteractive eXplorer (MINX). *Remote Sensing*, 5(9):4593–4628.

Nelson, D. L., Chen, Y., Kahn, R. a., Diner, D. J., and Mazzoni, D. (2008). Example applications of the MISR INteractive eXplorer (MINX) software tool to wildfire smoke plume analyses. *Proceedings of SPIE*, 7089:708909–708909–11.

Paugam, R., Wooster, M., Atherton, J., Freitas, S. R., Schultz, M. G., and Kaiser, J. W. (2015). Development and optimization of a wildfire plume rise model based on remote sensing data inputs - Part 2. *Atmospheric Chemistry and Physics Discussions*, 15(6):9815–9895.

Pechony, O. and Shindell, D. T. (2010). Driving forces of global wildfires over the past millennium and the forthcoming century. *Proceedings of the National Academy of Sciences of the United States of America*, 107(45):19167–70.

Penrod, A., Zhang, Y., Wang, K., Wu, S.-Y., and Leung, L. R. (2014). Impacts of future climate and emission changes on U.S. air quality. *Atmospheric Environment*, 89:533–547.

Peterson, D., Hyer, E., and Wang, J. (2013a). A short-term predictor of satellite-observed fire activity in the North American boreal forest: Toward improving the prediction of smoke emissions. *Atmospheric Environment*, 71:304–310.

Peterson, D., Hyer, E., and Wang, J. (2014). Quantifying the potential for high-altitude smoke injection in the North American boreal forest using the standard MODIS fire products and subpixel-based methods. *Journal of Geophysical Research: Atmospheres*, 119(6):3401–3419.

Peterson, D. and Wang, J. (2013). A sub-pixel-based calculation of fire radiative power from MODIS observations: 2. Sensitivity analysis and potential fire weather application. *Remote Sensing of Environment*, 129:231–249.

Peterson, D., Wang, J., Ichoku, C., Hyer, E., and Ambrosia, V. (2013b). A sub-pixel-based calculation of fire radiative power from MODIS observations: 1 Algorithm development and initial assessment. *Remote Sensing of Environment*, 129:262–279.

Peterson, D. A., Hyer, E. J., Campbell, J. R., Fromm, M. D., Hair, J. W., Butler, C. F., and Fenn, M. a. (2015). The 2013 Rim Fire: Implications for Predicting Extreme Fire Spread, Pyroconvection, and Smoke Emissions. *Bulletin of the American Meteorological Society*, 96(2):229–247.

Petrenko, M., Kahn, R., Chin, M., Soja, A., and Kucsera, T. (2012). The use of satellite-measured aerosol optical depth to constrain biomass burning emissions source strength in the global model GOCART. *Journal of Geophysical Research*, 117(D18):D18212.

Pfeiffer, M., Spessa, a., and Kaplan, J. O. (2013). A model for global biomass burning in preindustrial time: LPJ-LMfire (v1.0). *Geoscientific Model Development*, 6(3):643–685.

Price, C. and Rind, D. (1994). The impact of a 2x CO2 climate on lightning-caused fires. *Journal of Climate*, 7(10):1484–1494.

Randerson, J. T., Liu, H., Flanner, M. G., Chambers, S. D., Jin, Y., Hess, P. G., Pfister, G., Mack, M. C., Treseder, K. K., Welp, L. R., Chapin, F. S., Harden, J. W., Goulden, M. L., Lyons, E., Schuur, J. C. N. E. A. G., and Zender, C. S. (2006). The Impact of Boreal Forest Fire on Climate Warming. *Science*, 314:1130–1132.

Redemann, J., Vaughan, M. a., Zhang, Q., Shinozuka, Y., Russell, P. B., Livingston, J. M., Kacenelenbogen, M., and Remer, L. a. (2012). The comparison of MODIS-Aqua (C5) and CALIOP (V2 & V3) aerosol optical depth. *Atmospheric Chemistry and Physics*, 12(6):3025–3043.

Reichstein, M., Bahn, M., Ciais, P., Frank, D., Mahecha, M. D., Seneviratne, S. I., Zscheischler, J., Beer, C., Buchmann, N., Frank, D. C., Papale, D., Rammig, A., Smith, P., Thonicke, K., van der Velde, M., Vicca, S., Walz, A., and Wattenbach, M. (2013). Climate extremes and the carbon cycle. *Nature*, 500(7462):287–95.

Reick, C. H., Raddatz, T., Brovkin, V., and Gayler, V. (2013). Representation of natural and anthropogenic land cover change in MPI-ESM. *Journal of Advances in Modeling Earth Systems*, 5(3):459–482.

Reid, A. M. and Robertson, K. M. (2012). Energy content of common fuels in upland pine savannas of the south-eastern US and their application to fire behaviour modelling. *International Journal of Wildland Fire*, 21:591–595.

Reid, J. S., Koppmann, R., Eck, T. F., and Eleuterio, D. P. (2005). A review of biomass burning emissions part II: intensive physical properties of biomass burning particles. *Atmospheric Chemistry and Physics*, 5(3):799–825.

Remer, L., Kaufman, Y., Tanre, D., Mattoo, S., Chu, D., Martins, J., Li, R.-R., Ichoku, C., Levy, R., Kleidman, R., Eck, T., Vermote, E., and Holben, B. (2005). The MODIS Aerosol Algorithm, Products, and Validation. *J. Atmospheric Sciences*, 62:947 – 973.

Rio, C., Hourdin, F., and Ch, A. (2010). Numerical simulation of tropospheric injection of biomass burning products by pyro-thermal plumes. *Atmospheric Chemistry and Physics*, 10:3463–3478.

Rogers, B. M., Soja, A. J., Goulden, M. L., and Randerson, J. T. (2015). Influence of tree species on continental differences in boreal fires and climate feedbacks. *Nature Geoscience*, 8:228–234.

Rosário, N. E., Longo, K. M., Freitas, S. R., Yamasoe, M. a., and Fonseca, R. M. (2013). Modeling the South American regional smoke plume: aerosol optical depth variability and surface shortwave flux perturbation. *Atmospheric Chemistry and Physics*, 13(6):2923–2938.

Samset, B. H., Myhre, G., Schulz, M., Balkanski, Y., Bauer, S., Berntsen, T. K., Bian, H., Bellouin, N., Diehl, T., Easter, R. C., Ghan, S. J., Iversen, T., Kinne, S., Kirkevå g, a., Lamarque, J.-F., Lin, G., Liu, X., Penner, J. E., Seland, O., Skeie, R. B., Stier, P., Takemura, T., Tsigaridis, K., and Zhang, K. (2013). Black carbon vertical profiles strongly affect its radiative forcing uncertainty. *Atmospheric Chemistry and Physics*, 13(5):2423–2434.

Schmid, B., Michalsky, J., Halthore, R., Beauharnois, M., Harnson, L., Livingston, J., Russell, P., Holben, B., Eck, T., and Smirnov, A. (1999). Comparison of Aerosol Optical Depth from Four Solar Radiometers During the Fall 1997 ARM Intensive Observation Period. *Geophys. Res. Lett.*, 26(17):2725–2728.

Schneck, R., Reick, C. H., and Raddatz, T. (2013). Land contribution to natural CO2 variability on time scales of centuries. *Journal of Advances in Modeling Earth Systems*, 5(2):354–365.

Schroeder, W., Ellicott, E., Ichoku, C., Ellison, L., Dickinson, M. B., Ottmar, R. D., Clements, C., Hall, D., Ambrosia, V., and Kremens, R. (2014). Integrated active fire retrievals and biomass burning emissions using complementary near-coincident ground, airborne and spaceborne sensor data. *Remote Sensing of Environment*, 140:719–730.

Schutgens, N. A. J. and Stier, P. (2014). A pathway analysis of global aerosol processes. *Atmospheric Chemistry and Physics*, 14(21):11657–11686.

Schwarz, J. P., Samset, B. H., Perring, a. E., Spackman, J. R., Gao, R. S., Stier, P., Schulz, M., Moore, F. L., Ray, E. a., and Fahey, D. W. (2013). Global-scale seasonally resolved black carbon vertical profiles over the Pacific. *Geophysical Research Letters*, 40:5542–5547.

Sessions, W. R., Fuelberg, H. E., Kahn, R. a., and Winker, D. M. (2011). An investigation of methods for injecting emissions from boreal wildfires using WRF-Chem during ARCTAS. *Atmospheric Chemistry and Physics*, 11(12):5719–5744.

Shi, Y., Zhang, J., Reid, J. S., Hyer, E. J., Eck, T. F., Holben, B. N., and Kahn, R. a. (2011). A critical examination of spatial biases between MODIS and MISR aerosol products - application for potential AERONET deployment. *Atmospheric Measurement Techniques*, 4:2823–2836.

Shindell, D. T., Lamarque, J.-F., Schulz, M., Flanner, M., Jiao, C., Chin, M., Young, P. J., Lee, Y. H., Rotstayn, L., Mahowald, N., Milly, G., Faluvegi, G., Balkanski, Y., Collins, W. J., Conley, a. J., Dalsoren, S., Easter, R., Ghan, S., Horowitz, L., Liu, X., Myhre, G., Nagashima, T., Naik, V., Rumbold, S. T., Skeie, R., Sudo, K., Szopa, S., Takemura, T., Voulgarakis, A., Yoon, J.-H., and Lo, F. (2013). Radiative forcing in the ACCMIP historical and future climate simulations. *Atmospheric Chemistry and Physics*, 13(6):2939–2974.

Siddaway, J. M. and Petelina, S. V. (2011). Transport and evolution of the 2009 Australian Black Saturday bushfire smoke in the lower stratosphere observed by OSIRIS on Odin. *Journal of Geophysical Research*, 116(D6):1–9.

Smirnov, A., Holben, B. N., Giles, D. M., Slutsker, I., O'Neill, N. T., Eck, T. F., Macke, A., Croot, P., Courcoux, Y., Sakerin, S. M., Smyth, T. J., Zielinski, T., Zibordi, G., Goes, J. I., Harvey, M. J., Quinn, P. K., Nelson, N. B., Radionov, V. F., Duarte, C. M., Losno, R., Sciare, J., Voss, K. J., Kinne, S., Nalli, N. R., Joseph, E., Krishna Moorthy, K., Covert, D. S., Gulev, S. K., Milinevsky, G., Larouche, P., Belanger, S., Horne, E., Chin, M., Remer, L. a., Kahn, R. a., Reid, J. S., Schulz, M., Heald, C. L., Zhang, J., Lapina, K., Kleidman, R. G., Griesfeller, J., Gaitley, B. J., Tan, Q., and Diehl, T. L. (2011). Maritime aerosol network as a component of AERONET - first results and comparison with global aerosol models and satellite retrievals. *Atmospheric Measurement Techniques*, 4(3):583–597.

Smith, A. M. S., Tinkham, W. T., Roy, D. P., Boschetti, L., Kremens, R. L., Kumar, S. S., Sparks, A. M., and Falkowski, M. J. (2013). Quantification of fuel moisture effects on biomass consumed derived from fire radiative energy retrievals. *Geophysical Research Letters*, 40(23):6298–6302.

Sofiev, M., Ermakova, T., and Vankevich, R. (2012). Evaluation of the smoke-injection height from wild-land fires using remote-sensing data. *Atmospheric Chemistry and Physics*, 12(4):1995–2006.

Sofiev, M., Vankevich, R., Ermakova, T., and Hakkarainen, J. (2013). Global mapping of maximum emission heights and resulting vertical profiles of wildfire emissions. *Atmospheric Chemistry and Physics*, 13(14):7039–7052.

Spichtinger, N., Wenig, M., James, P., Wagner, T., Platt, U., and Stohl, A. (2001). Satellite detection of a continental-scale plume of nitrogen oxides from boreal forest fires. *Geophysical Research Letters*, 28(24):4579–4582.

Spracklen, D. V., Mickley, L. J., Logan, J. A., Hudman, R. C., Yevich, R., Flannigan, M. D., and Westerling, A. L. (2009). Impacts of climate change from 2000 to 2050 on wildfire activity and carbonaceous aerosol concentrations in the western United States. *Journal of Geophysical Research*, 114(D20):D20301.

Stavros, E. N., McKenzie, D., and Larkin, N. (2014). The climate-wildfire-air quality system: interactions and feedbacks across spatial and temporal scales. *Wiley Interdisciplinary Reviews: Climate Change*, 5(6):719–733.

Stein, A. F., Rolph, G. D., Draxler, R. R., Stunder, B., and Ruminski, M. (2009). Verification of the NOAA Smoke Forecasting System: Model Sensitivity to the Injection Height. *Weather and Forecasting*, 24(2):379–394.

Stevens, B., Giorgetta, M., Esch, M., Mauritsen, T., Crueger, T., Rast, S., Salzmann, M., Schmidt, H., Bader, J., Block, K., Brokopf, R., Fast, I., Kinne, S., Kornblueh, L., Lohmann, U., Pincus, R., Reichler, T., and Roeckner, E. (2013). Atmospheric component of the MPI-M Earth System Model: ECHAM6. *Journal of Advances in Modeling Earth Systems*, 5(2):146–172.

Stier, P., Feichter, J., Kinne, S., Kloster, S., Vignati, E., Wilson, J., Ganzeveld, L., Tegen, I., and Werner, M. (2005). The aerosol-climate model ECHAM5-HAM. *Atmospheric Chemistry and Physics*, 5(4):1125–1156.

Stocks, B., Fosberg, M., and Lynham, T. (1998). Climate change and forest fire potential in Russian and Canadian boreal forests. *Climatic Change*, 38:1–13.

Strada, S., Freitas, S. R., Mari, C., Longo, K. M., and Paugam, R. (2013). One-dimensional simulation of fire injection heights in contrasted meteorological scenarios with PRM and Meso-NH models. *Geoscientific Model Development Discussions*, 6(1):721–790.

Tanre, D., Kaufman, Y. J., Herman, M., and Mattoo, S. (1997). Remote sensing of aerosol properties over ocean using the MODIS/EOS spectral radiances. *Journal of Geophysical Research*, 102:16971 – 16988.

Textor, C., Schulz, M., Guibert, S., Kinne, S., Balkanski, Y., Bauer, S., Berntsen, T., Berglen, T., Boucher, O., Chin, M., Dentener, F., Diehl, T., Easter, R., Feichter, H., Fillmore, D., Ghan, S., Ginoux, P., Gong, S., Grini, a., Hendricks, J., Horowitz, L., Huang, P., Isaksen, I., Iversen, I., Kloster, S., Koch, D., Kirkevå g, a., Kristjansson, J. E., Krol, M., Lauer, a., Lamarque, J. F., Liu, X., Montanaro, V., Myhre, G., Penner, J., Pitari, G., Reddy, S., Seland, O., Stier, P., Takemura, T., and Tie, X. (2006). Analysis and quantification of the diversities of aerosol life cycles within AeroCom. *Atmospheric Chemistry and Physics*, 6(7):1777–1813.

Thonicke, K., Spessa, A., Prentice, I. C., Harrison, S. P., Dong, L., and Carmona-Moreno, C. (2010). The influence of vegetation, fire spread and fire behaviour on biomass burning and trace gas emissions: results from a process-based model. *Biogeosciences*, 7(6):1991–2011.

Thonicke, K., Venevsky, S., Sitch, S., and Cramer, W. (2001). The role of fire disturbance for global vegetation dynamics: coupling fire into a Dynamic Global Vegetation Model. *Global Ecology and Biogeography*, 10:661–677.

Tosca, M., Randerson, J., Zender, C. S., Flanner, M. G., and Rasch, P. J. (2010). Do biomass burning aerosols intensify drought in equatorial Asia during El Niño? *Atmospheric Chemistry and Physics*, 10(8):3515–3528.

Tosca, M. G., Randerson, J. T., and Zender, C. S. (2013). Global impact of smoke aerosols from landscape fires on climate and the Hadley circulation. *Atmospheric Chemistry and Physics*, 13(10):5227–5241.

Tosca, M. G., Randerson, J. T., Zender, C. S., Nelson, D. L., Diner, D. J., and Logan, J. a. (2011). Dynamics of fire plumes and smoke clouds associated with peat and deforestation fires in Indonesia. *Journal of Geophysical Research*, 116(D8):1–14.

Trentmann, J., Luderer, G., Winterrath, T., Fromm, M. D., Servranckx, R., Textor, C., Herzog, M., and Graf, H. (2006). Modeling of biomass smoke injection into the lower stratosphere by a large forest fire (Part I): reference simulation. *Atmospheric Chemistry and Physics*, 6(1999):5247–5260.

Twomey, S. (1977). The influence of pollution on the shortwave albedo of clouds. *Journal of the atmospheric sciences*, 34:1149–1152.

Unger, N., Bond, T. C., Wang, J. S., Koch, D. M., Menon, S., Shindell, D. T., and Bauer, S. (2010). Attribution of climate forcing to economic sectors. *Proceedings of the National Academy of Sciences of the United States of America*, 107(8):3382–3387.

Urbanski, S. (2014). Wildland fire emissions, carbon, and climate: Emission factors. *Forest Ecology and Management*, 317:51–60.

Val Martin, M., Kahn, R. A., Logan, J. A., Paugam, R., Wooster, M., and Ichoku, C. (2012). Space-based observational constraints for 1-D fire smoke plume-rise models. *Journal of Geophysical Research*, 117(D22):D22204.

Val Martin, M., Logan, J. A., Kahn, R. A., Leung, F.-Y., Nelson, D. L., and Diner, D. J. (2010). Smoke injection heights from fires in North America: analysis of 5 years of satellite observations. *Atmospheric Chemistry and Physics*, 10(4):1491–1510.

van der Werf, G., Randerson, J. T., Giglio, L., Collatz, G. J., Kasibhatla, P. S., and Arellano, A. F. (2006). Interannual variability in global biomass burning emissions from 1997 to 2004. *Atmospheric Chemistry and Physics*, 6:3423–3441.

van der Werf, G. R., Randerson, J. T., Giglio, L., Collatz, G. J., Mu, M., Kasibhatla, P. S., Morton, D. C., DeFries, R. S., Jin, Y., and van Leeuwen, T. T. (2010). Global fire emissions and the contribution of deforestation, savanna, forest, agricultural, and peat fires (1997–2009). *Atmospheric Chemistry and Physics*, 10(23):11707–11735.

van Vuuren, D. P. and Carter, T. R. (2014). Climate and socio-economic scenarios for climate change research and assessment: reconciling the new with the old. *Climatic Change*, 122(3):415–429.

van Vuuren, D. P., Edmonds, J., Kainuma, M., Riahi, K., Thomson, A., Hibbard, K., Hurtt, G. C., Kram, T., Krey, V., Lamarque, J.-F., Masui, T., Meinshausen, M., Nakicenovic, N., Smith, S. J., and Rose, S. K. (2011). The representative concentration pathways: an overview. *Climatic Change*, 109(1-2):5–31.

von Hardenberg, J., Vozella, L., Tomasi, C., Vitale, V., Lupi, A., Mazzola, M., van Noije, T. P. C., Strunk, A., and Provenzale, A. (2012). Aerosol optical depth over the Arctic: a comparison of ECHAM-HAM and TM5 with ground-based, satellite and reanalysis data. *Atmospheric Chemistry and Physics*, 12(15):6953–6967.

Wang, J., Christopher, S. a., Nair, U. S., Reid, J. S., Prins, E. M., Szykman, J., and Hand, J. L. (2006). Mesoscale modeling of Central American smoke transport to the United States: 1. "Top-down" assessment of emission strength and diurnal variation impacts. *Journal of Geophysical Research*, 111(D5):1–21.

Ward, D. S., Kloster, S., Mahowald, N. M., Rogers, B. M., Randerson, J. T., and Hess, P. G. (2012). The changing radiative forcing of fires: global model estimates for past, present and future. *Atmospheric Chemistry and Physics*, 12(22):10857–10886.

Wiedinmyer, C., Akagi, S. K., Yokelson, R. J., Emmons, L. K., Al-Saadi, J. A., Orlando, J. J., and Soja, A. J. (2011). The Fire INventory from NCAR (FINN): a high resolution global model to estimate the emissions from open burning. *Geoscientific Model Development*, 4(3):625–641.

Winker, D. M., Pelon, J., Coakley, J. a., Ackerman, S. A., Charlson, R. J., Colarco, P. R., Flamant, P., Fu, Q., Hoff, R. M., Kittaka, C., Kubar, T. L., Le Treut, H., McCormick, M. P., Mégie, G., Poole, L., Powell, K., Trepte, C., Vaughan, M. A., and Wielicki, B. A. (2010). The CALIPSO Mission: A Global 3D View of Aerosols and Clouds. *Bulletin of the American Meteorological Society*, 91(9):1211–1229.

Winker, D. M., Tackett, J. L., Getzewich, B. J., Liu, Z., Vaughan, M. a., and Rogers, R. R. (2013). The global 3-D distribution of tropospheric aerosols as characterized by CALIOP. *Atmospheric Chemistry and Physics*, 13(6):3345–3361.

Wooster, M. J., Roberts, G., Perry, G. L. W., and Kaufman, Y. J. (2005). Retrieval of biomass combustion rates and totals from fire radiative power observations: FRP derivation and calibration relationships between biomass consumption and fire radiative energy release. *Journal of Geophysical Research*, 110(D24):D24311.

Wotawa, G. and Trainer, M. (2000). The Influence of Canadian Forest Fires on Pollutant Concentrations in the United States. *Science*, 288:324–328.

Yu, H., Kaufman, Y. J., Chin, M., Feingold, G., Remer, L. A., Anderson, T. L., Balkanski, Y., Bellouin, N., Boucher, O., Christopher, S., DeCola, P., Kahn, R., Koch, D., Loeb, N., Reddy, M. S., Schulz, M., Takemura, T., and Zhou, M. (2006). A review of measurement-based assessments of the aerosol direct radiative effect and forcing. *Atmospheric Chemistry and Physics*, 6(3):613–666.

Yue, C., Ciais, P., Cadule, P., Thonicke, K., Archibald, S., Poulter, B., Hao, W. M., Hantson, S., Mouillot, F., Friedlingstein, P., Maignan, F., and Viovy, N. (2014). Modelling the role of fires in the terrestrial carbon balance by incorporating SPITFIRE into the global vegetation model ORCHIDEE - Part 1: simulating historical global burned area and fire regimes. *Geoscientific Model Development*, 7(6):2747–2767.

Yue, C., Ciais, P., Cadule, P., Thonicke, K., and van Leeuwen, T. T. (2015). Modelling the role of fires in the terrestrial carbon balance by incorporating SPITFIRE into the global vegetation model ORCHIDEE - Part 2: Carbon emissions and the role of fires in the global carbon balance. *Geoscientific Model Development*, 8(5):1321–1338.

Zhang, F., Wang, J., Ichoku, C., Hyer, E. J., Yang, Z., Ge, C., Su, S., Zhang, X., Kondragunta, S., Kaiser, J. W., Wiedinmyer, C., and da Silva, A. (2014). Sensitivity of mesoscale modeling of smoke direct radiative effect to the emission inventory: a case study in northern sub-Saharan African region. *Environmental Research Letters*, 9(7):075002.

Zhang, K., O'Donnell, D., Kazil, J., Stier, P., Kinne, S., Lohmann, U., Ferrachat, S., Croft, B., Quaas, J., Wan, H., Rast, S., and Feichter, J. (2012a). The global aerosol-climate model ECHAM-HAM, version 2: sensitivity to improvements in process representations. *Atmospheric Chemistry and Physics*, 12(19):8911–8949.

Zhang, X., Kondragunta, S., Ram, J., Schmidt, C., and Huang, H.-C. (2012b). Near-real-time global biomass burning emissions product from geostationary satellite constellation. *Journal of Geophysical Research*, 117(D14):D14201.

Acronyms

AEROCOM Aerosol Comparisons between Observations and Models

AERONET Aerosol Robotic Network

AMIP Atmosphere Model Intercomparison Project

AMS Autonomous Modular Sensor

AOT aerosol optical thickness

AOD aerosol optical depth

BC black carbon

CALIOP Cloud-Aerosol Lidar with Orthogonal Polarization

CESM Community Earth System Model

DGVM dynamic global vegetation model

DMS dimethyl sulfide

ESM Earth system model

FDI fire danger index

FINN Fire INventory from NCAR

FRP fire radiative power

FWI fire weather index

FT free troposphere

GCM general circulation model

GFAS Global Fire Assimilation System

GFED Global Fire Emission Data Base

GISS Goddard Institute for Space Studies

HYSPLIT Hybrid Single Particle Lagrangian Integrated Trajectory

IBBI Interdisciplinary Biomass Burning Initiative

ICON icosahedral non-hydrostatic

iLEAPS Integrated Land Ecosystem Atmosphere Processes Study

KS Kolmogorov-Smirnov

LCT land cover type

LSCE Laboratoire des Sciences du Climat et de l'Environnement

MACC Monitoring Atmospheric Composition and Climate

MAN Marine Aerosol Network

MINX MISR Interactive Explorer

MISR Multi-angle Imaging Spectroradiometer

MODIS Moderate Resolution Imaging Spectroradiometer

MOPITT Measurement of Pollution in the Troposphere

MPI-ESM Max Planck Institute Earth System Model

MPHP MISR Plume Height Project

NH Northern Hemisphere

NPP net primary productivity

NRL Naval Research Laboratory

OC organic carbon

Oslo-CTM2 University of Oslo chemistry-transport model

PBL planetary boundary layer

PD present day

PDF probability density function

PFT plant functional type

PRM-MODEL plume rise model

RCP Representative Concentration Pathway

RF radiative forcing

RH relative humidity

SD standard deviation

SH Southern Hemisphere

SO_2 sulfur dioxide

SP Sofiev Parametrization

SSP Shared Socio–economic Pathway

SST sea surface temperature

HadGEM3-UKCA Hadley Centre Global Environment Model version 3 – UK Chemistry and Aerosols

TOA top of atmosphere

WMO World Meteorological Organization

List of Figures

List of Tables

Acknowledgements

First, I thank my supervisor Silvia Kloster who offered me the opportunity to do research at the MPI-M. I am grateful for the very good support during my entire PhD studies. The excellent supervision helped me to make continuous progress and to improve my scientific skills.

Furthermore, I would like to thank Martin Claussen and Cathy Hohenegger who co-supervised my research. The critical and inspiring discussions at our regular IMPRS panel meetings contributed helpful ideas for the success of this PhD thesis.

I also thank the IMPRS-ESM team including Antje Weitz, Wiebke Boehm and Cornelia Kampmann. The interdisciplinarity of the school and the great administrative support offered me a vibrant working environment which always gave me encouragement to successfully complete this PhD in time.

Moreover, I thank Gitta Lasslop, Stiig Wilkenskjeld, Samuel Remy, Johannes Kaiser and Nick Schutgens for their technical, scientific and personal support. As co-authors of the papers published in the context of this thesis, they contributed substantially to the results of this study. I also thank Sebastian Rast, Felicia Brisc and Angelika Heil for their technical support. Furthermore, I appreciate Stephan Bakan's critical and inspiring internal review of all three journal contributions.

I would like to thank my colleagues Jan Ackmann, Jessica Engels, Victoria Naipal and all others for the pleasant working atmosphere and the enjoyable lunch breaks.

I also thank my parents who helped to develop my talents and who provided me with the stamina which is necessary to successfully complete a PhD.

Last but not least, I would like to thank Julia for continuously supporting me. I am deeply gratefully for your patience and your encouragement throughout the last three years.

Aus dieser Dissertation hervorgegangene Veröffentlichungen

List of Publications

Veira, A., Kloster, K., Wilkenskjeld, S., Remy, S. (2015). Fire emission heights in the climate system Part 1: Global plume height patterns simulated by ECHAM6-HAM2. Atmospheric Chemistry and Physics, 15, 7155–7171.

Veira A., Kloster K., Schutgens, N. A. J. , Kaiser, J. W. (2015). Fire emission heights in the climate system - Part 2: Impact on transport, black carbon concentrations and radiation. Atmospheric Chemistry and Physics, 15, 7173–7193.

Veira, A., Lasslop, L., Kloster K. (2015). Wildfires in a warmer climate: Emission fluxes, emission heights and black carbon concentrations in 2090-2099. Journal of Geophysical Research - Atmospheres. Submitted on 27 August 2015, Manuscript ID 2015JD024142.